SUPPRESSION OF CLASSICAL FLUTTER USING A 'SMART' ROTOR

<u>Master Thesis</u>

Sustainable Energy Technology (SET)

TUDelft & TU/e

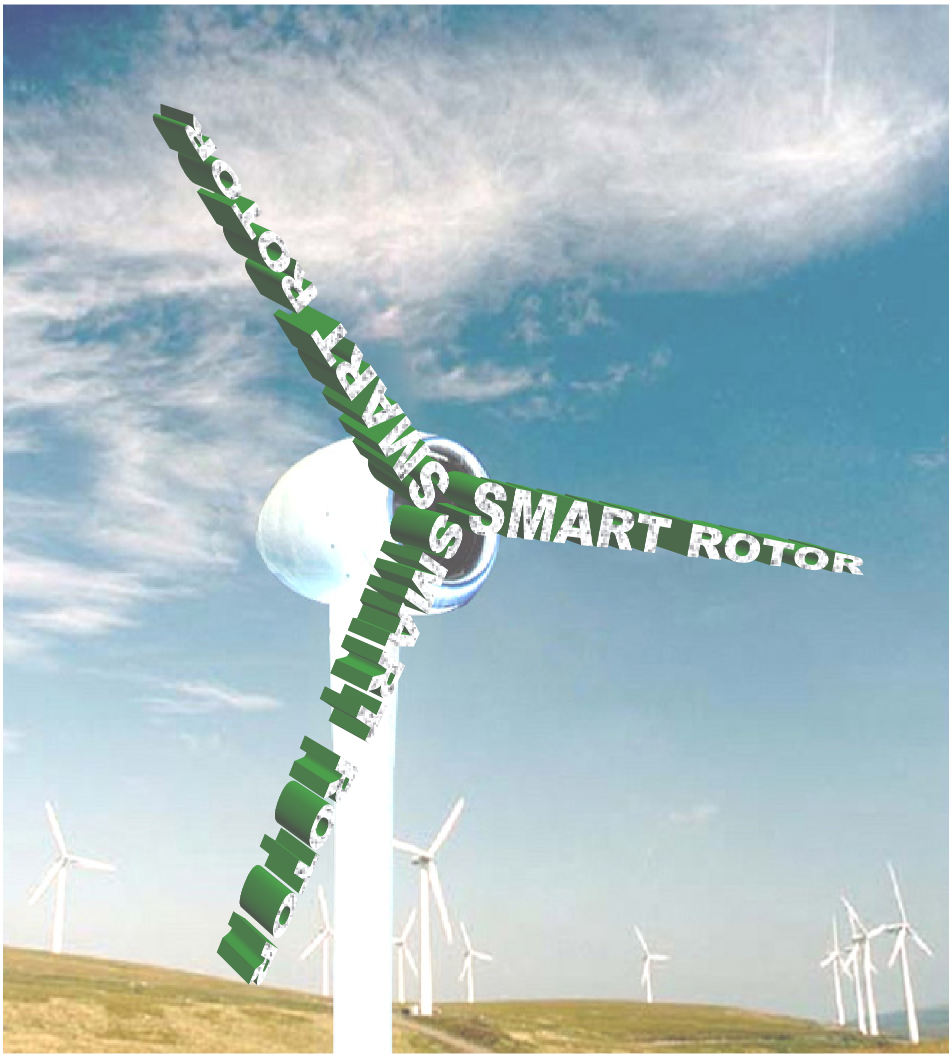

Author: Greg Politakis

August 2007

TABLE OF CONTENTS

Preface

The intention of the material presented in this Masters Thesis topic is to build upon and support scientific knowledge in aeroelastic phenomena in the design of wind turbines. It is hoped to show there are still promising technological advancements in wind turbine technology to maintain its status as a significant renewable energy supplier for the developing and developed world.

The author draws inspiration for such an undertaking in the belief that accumulation of such knowledge can be instilled in the wind turbine industry so manufacturers can produce more efficient, sustainable and cheaper electricity generation systems. These inspirations are placed in the context of driving towards new solutions for the carbon dioxide paradigm and to counter the human impact on the Earth's climate. One can only trust that every little bit helps.

The author would like thank Wouter Haans for his insights and continual guidance for the duration of the project; and Jan-Willem van Wingerden for his valuable contribution and guidance in control system theory.

Greg Politakis

Summary

The mechanics of aeroelastic instabilities is particularly important in relation to the next generation of wind turbine designs. Sizes approaching the 10MW capacity will have a rotor diameter somewhere in the order of 170m. This could mean much higher loads and more flexible blade designs than current MW wind turbines, most probably resulting in aeroelastic instabilities not commonly seen in the machines of today. Load control on an aerofoil using actuated trailing edge flaps could be a means to mitigate this issue.

Load control on future wind turbines should serve three main goals:

- Improve the fatigue life
- Reduce extreme loads
- Improve aeroelastic stability

The two most important are fatigue life and aeroelastic stability; as these are the likely design drivers for future giant wind turbines (10MW and beyond).

The content of this report is focused on the effects of trailing edge flaps on the aeroelastic stability of a rotor ('Smart' Rotor), in particular, the two degree of freedom Flap-Torsion Flutter instability - Classical Flutter.

Current research has shown promising results for load reduction on an aerofoil using trailing edge flaps. The aeroelastic model employed in this study uses Theodorsen's theory for a flat-plate aerofoil with a trailing edge flap for determination of the lift coefficient. A basic BEM aerodynamic model determines the induced forces on the blades with a blade structural response exhibited according to a modal representation of a blade (eigenmodes and eigenfrequencies).

The aeroelastic model of the wind turbine (rigid hub – no tower interaction) is designed with the intention to capture the Classical Flutter instability so that a simple controller for an actuated trailing edge flap can be investigated to show if controllability on the Flutter limits is achievable.

The final goal is to show that it could be feasible for giant wind turbines to avoid Flutter regions in their normal operational envelope with implementation of the 'Smart' rotor concept.

Nomenclature

Φ	Total twist (torsion) about the elastic axis
x’	The axial elastic axis of the blade principle axes
y’	In-plane (in direction of chord)principle axis (edgewise)
z’	Out of plane principle axis (flapwise)
X	Rotating blade axial axis
Y	In-plane rotating blade axis
Z	Out of plane rotating blade axis
M_{shc}	Total moment about the shear centre
X_{NR}	Non rotating blade axial axis
Y_{NR}	Non rotating blade in-plane axis
Z_{NR}	Non rotating blade out of plane axis
Sh_c	Shear centre
ψ	Rotor azimuth (zero in 6 o’clock position – downward)
y_{ac}	Aerodynamic centre offset from shear centre
y_{cg}	Centre of gravity offset from the shear centre
k_z	Flapwise spring stiffness
k_y	Edgewise spring stiffness
k_φ	Torsional spring stiffness
φ_p	Blade pitch angle
φ_t	Blade built-in twist
φ_e	Torsion elastic deformation
C_{Dax}	Axial aerodynamic force coefficient
a	Axial induction factor at the disc
V	Undisturbed mean wind speed
$\dot{Z}$	Out of plane blade velocity
$\dot{Y}$	In-plane velocity of the blade
Ω	Angular velocity of the rotor
R	*R*adius of the blade section element
c_l	Lift coefficient
c_d	Drag coefficient
c_m	Moment coefficient
ρ	Air density
c	Chord length

dr	Length of a blade section (span) element
α_{qs}	*Q*uasi-steady angle of attack due to a pitch and plunge motion
δ	Trailing-edge flap deflection
E	Non-dimensional trailing-edge flap hinge location in semi-chords
W	Relative wind speed as seen by the rotor
S	Non-dimensional aerodynamic time
w_g	Downwash velocity
δ_{qs}	Quasi-steady angle of attack due to a trailing-edge flap deflection
H	Wagner function
Ψ	Küssner function
φ	Inflow angle
m^i	Concentrated mass at the i^{th} node
$P^i_{z',y'}$	Inertial loading in the respective coordinate planes
$u^{1f}_{z'}$	1^{st} flapwise eigenmode in the principle axes
$u^{1e}_{y'}$	1^{st} edgewise eigenmode in the principle axes
k	The orthogonality constant
$u_{z',y'}$	Deflection of blade in principle axes
φ^i_t	Torsion eigenmode at respective iteration step
$M_l(x')$	Local moment about the pitching axis
k_t	Curvature associated with torsion eigenmode
GJ	Blade torsional rigidity
q_g	Generalised coordinate vector
ζ	Corresponding normalised mode shape vectors
$[M']$	Generalised Mass matrix
$[K']$	Generalised stiffness matrix
$[F_{ext}(t)']$	Generalised force as a function of time
$q_{1f,1e,2f,1T}$	Solutions for generalised coordinates for the 1^{st} flap, 1^{st} edge, 2^{nd} flap and 1^{st} torsion mode
W_i	Represents the virtual work for a unit displacement in a DOF
P_i	Local force in the X-Z or X-Y plane at respective blade station along the radius
s_i	Slope (tangent to displacement) at the respective blade node
$\Delta x'$	Distance between discretised nodal segments of the blade

M_i^{φ}	Aerodynamic moment at the respective blade node
M_i^{L}	Moment caused by lift force at aerodynamic centre about shear centre
F_{c_i}	Component of centrifugal force normal to the elastic axis at a given node
$\vec{\Omega}$	Rotational vector of the rotor
$\vec{r}$	Local radial vector in time of a point on the blade from the origin of the rotating coordinate system
β	Local blade flapping angle
$P_{eq,z}$	Equivalent force in the X-Z plane
$F_{x'}$	Total axial force in the blade
$F_{gX,Y,Z}$	Force of gravity in the rotating blade system
$L_{Z,Y,i}$	Aerodynamic forces as determined from BEM theory
I_{φ}	Blade pitching inertia
K_{φ}	Radius of gyration of a mass about the shear centre
ω_{z}^{1f}	1st Flapwise Eigenfrequency
$\omega_{z'}^{2f}$	2nd Flapwise Eigenfrequency
$\omega_{y'}^{1e}$	1st Edgewise Eigenfrequency
ω_{φ}^{1T}	1st Torsion Eigenfrequency
V_t	Rotor tangential velocity component
V_p	Rotor perpendicular velocity component
V_f	Flutter tip speed velocity
$c_{l,nc}$	Non-circulatory component of lift coefficient
$c_{l,c}$	Circulatory component of lift coefficient
F_{10}, F_{11}, F_1, F_4	Theodorsen's Coefficeints
ξ	Damping in the actuator

1 Introduction

The content of this report is focused on investigating the performance of trailing edge flaps on maintaining the aeroelastic stability of a rotor; in particular, their ability to control the Flap-Torsion Flutter instability (Classical Flutter). A simple aeroelastic model of a wind turbine (rigid hub – no tower interaction) is developed to capture the Flutter instability and a simple controller for a trailing edge flap is investigated to show if controllability is achievable on the Flutter limits. A schematic of a blade with a trailing edge flap (sometimes referred to as a 'smart' rotor) is shown in Figure 1.1.

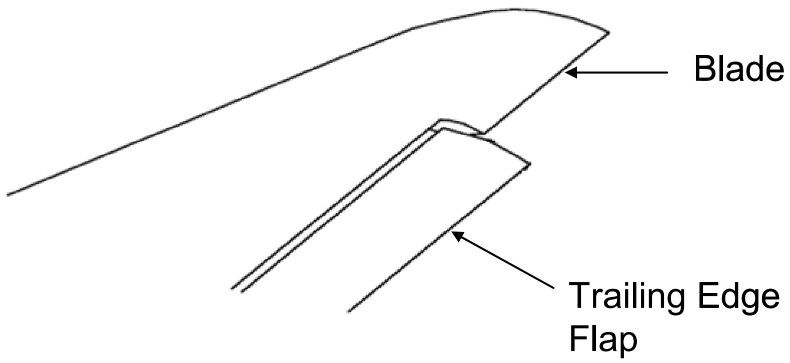

Figure 1.1 Smart Rotor Concept – Aerofoil Showing Added Trailing Edge Flap

1.1 Motivation

The mechanics and understanding of aeroelastic instabilities is particularly important in relation to the next generation of wind turbine designs. With wind turbines entering a mature phase in terms of technological advancement, the logical direction for further success in the industry lies in bigger machines capable of massive electricitiy generation. Sizes approaching the 10MW capacity will have a rotor diameter somewhere in the order of 170m. Even 20MW machines have been conceptualised, with a diameter well over 200m. This means much higher loads and more flexible blades than current MW wind turbines, most probably resulting in aeroelastic instabilities not commonly seen in the current machines of today. Load control on an aerofoil using trailing edge flaps is a concept that proposes to control the lift force experienced by the blade.

Load control on future wind turbines should serve three main goals:

- Improve the fatigue life
- Reduce extreme loads
- Improve aeroelastic stability

The two most important of these are fatigue life and aeroelastic stability, as these will be the design drivers for wind turbines of the future.

Aeroelastic stability of a wind turbine refers to the dynamic response of the various components of a wind turbine (blades, tower, etc) given an external loading condition provided by-in this case-the wind. In short, aerodynamics is dependent on structural response of the wind turbine, while the structural response is dependent on the aerodynamics; thus, such a coupling has the potential to lead to undesirable system dynamics under certain conditions. Because wind turbines operate on the principle of aerodynamics, the tower motion, blade accelerations, etc, relative to the varying vectorial nature of wind, can be in a mode where the phase of the response is conducive to drawing energy from the wind into the system and causing undesirable violent vibrations.

Two common such instabilities exhibited by aerofoil based machines are the Flap-Lag and Classical Flutter instability. For reasons stated in section 2, Classical Flutter is deemed to be more vital in the context of future large wind turbines and is the focus of the current work. Classical Flutter has not been the cause of any failures to date in wind turbines; rather it being more prevalent in rotorcraft applications. However, with a reducing blade torsional stiffness with increasing blade radius, it is possible the stability limit (condition at which Flutter occurs, i.e. for a given blade tip speed) between the turbines of now, and those of the future, is becoming narrower.

To this end, the motivator for undertaking the present analysis of Flutter suppression using actuated trailing edge geometry is to assess a possible solution for manufacturers wishing to tackle the stability problem that will inevitably ensue. It is certainly desirable to know if Classical Flutter needs to be taken into account and what can be done to mitigate its effects.

1.2 Aims & Objectives

Current research has shown promising results for load reduction potential using actuated trailing edge flaps. The present analysis therefore attempts to support this claim through showing its worth as an aeroelastic stability shaping device enhancing the design and development of giant wind turbine machines.

The primary aim of this study is to investigate the Classical Flutter instability limit margins of today's largest wind turbines; 5MW machines with rotor diameters approximately of 120m, compared to machines that will be in the order of 7 – 10MW with diameters exceeding 170m. This should provide an indication of whether Flutter analyses need to become common place in new designs of large wind turbines. It is then hoped to show in theory, that actuated trailing edge flaps can provide a solution to combat this problem. This is achieved through the following set of sub-objectives to:

- Set-up a simplified Aeroelastic Model of a Wind Turbine with a rigid hub, including the effects of trailing edge geometry
    - ➢ Aerodynamic Model (lift coefficient) based on Theodorsen's theory for a flat plate aerofoil
    - ➢ Structural model based on a modal (eigenmode and eigenfrequency) representation of the total length of blade
    - ➢ Blade Element Momentum (BEM) theory for determining blade forces
- Propose a design of a 10MW blade using scaling laws and investigate its Flutter stability limit margin and compare to a representative 5MW wind turbine design of today
- Implement a basic controller (e.g. Proportional, Integral or Differential - PID) for a given trailing edge flap actuator and control surface geometry assembly specifically for the intention of suppressing Flutter

The report layout consists of six sections in total, more or less following the format of the aforementioned objectives. In section 2, some background information and analysis of aeroelastic phenomena is given to put this study into context and to show its significance in wind turbine design. In section 3, the approach adopted and theory used to build the aerolelastic model and represent the wind turbine structural characteristics is detailed. The cases explored and method for determining the Flutter limits is also provided.

Section 4 attempts to validate the aeroelastic model using a comparison of dynamic response across the steady-state wind operating range of the wind turbine. Following this, the analysis of Flutter margins for the 5MW and proposed 10MW wind turbine is examined.

In section 5, the method employed in designing a controller for the trailing edge flap is outlined as well as the parameters defining the experimental set-up for testing the performance of the actuated flap for suppressing Flutter. Finally, some key conclusions and recommendations are made for possible improvements to the work should future related investigations take place.

2 Background

2.1 Wind Turbines and Aeroelastic Stability

Aeroelastic Stability of a wind turbine refers to the dynamic interactions of the various components and loading of a wind turbine in its operational state. It is known wind turbines operate in a range of conditions (wind speed fluctuations, turbulence, rotational speeds, etc), and as such, the dynamic interaction occurring between the external loading and structural components are complicated.

Like most dynamic systems, reduction of fatigue loads in the structure is given much attention in the design process. Unwanted vibrations are well known to be the causes of fatigue leading to shorter component lifetime or even premature failure if they are such that they grow in amplitude without recovery. Such vibrations which do not reduce in time are termed unstable. It would now be timely to define the different vibration modes and the classification of their effect as an instability. This is neatly summarised in Figure 2.1 [23].

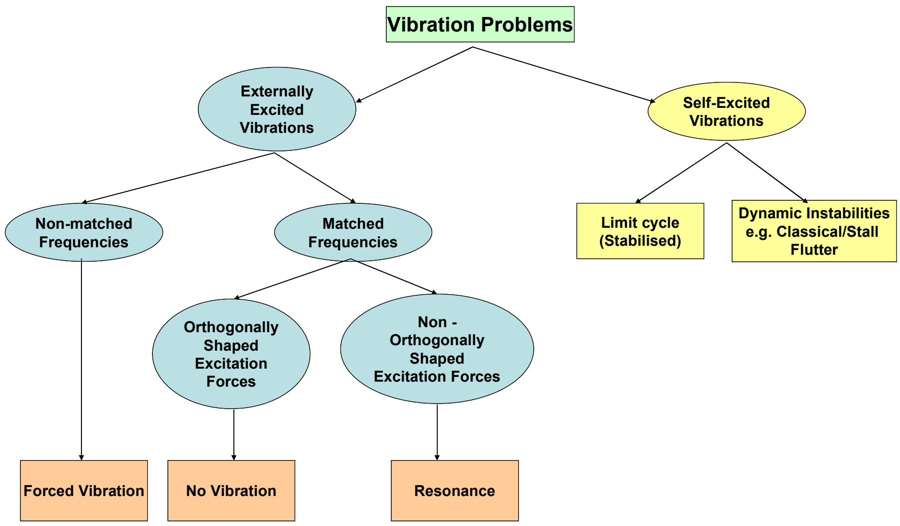

Figure 2.1 Vibration Modes and Stability / Instability Classification

Two categories of vibrations are shown to be: those induced under external excitation forces, such as aerodynamic forces and gravity, and those from self-excited vibrations [23]. The latter means vibrations can occur without external forces acting, but rather the vibrations occur due to an energy feeding mechanism (transfer of energy from one mode to another) possibly resulting in an instability [23]. If this type of vibration does not stabilise, then the result is a dynamic instability which grows exponentially in time. While resonance can also lead to catastrophic failures, dynamic instabilities can reach the ultimate stress limits faster. The relevance of determining the aeroelastic stability of a wind turbine for example, is plainly evident. It is even more so critical for the wind turbine designs considered for the future, which are fast approaching sizes which could be causing the instability limits to reduce (in terms of operational parameters of wind turbines, (e.g. tip speeds) as exists in the medium to large wind turbine designs of the present.

This section focuses on the phenomena of dynamic instabilities, namely those concerned with the rotor instabilities only. Three of the prominent aeroelastic instabilities experienced by wind turbines are the one degree of freedom ‘Stall Flutter’ and the two degree of freedom stabilities; ‘Classical Flutter’ (Flap-Torsion dynamics) and the ‘Flap-Lag’ instability (stall induced vibrations).

In the next sections, some of these instabilities are examined to find the most important and the one that could be alleviated with a trailing edge flap.

2.1.1 One-Degree of Freedom Stall Flutter

Stall Flutter is a one dimensional instability in blade torsion that can occur due to dynamic stall conditions. Dynamic stall means that the effective onset of stall on an aerofoil is delayed in comparison to the static case which stalls at a prescribed stall-angle α. This means that instead of lift decreasing at the static stall angle, lift continues to increase with increasing α to a maximum value before stall occurs and then finally decreases. The position of the lift force also changes relative to the aerodynamic centre further contributing to a moment. This effects is shown in Figure 2.2.

To accompany this, the pitching moment about the aerodynamic centre turns negative above the static stall angle due to a shifting pressure force along the aerofoil from a surface traversing vortex formed at high angles of attack – refer to Figure 2.2 [26]. This moment is significantly higher than in the static conditions and can cause large vibrations, especially when lift is still occurring on the blade (see stage d) in Figure 2.2). As α is decreased, the aerofoil also un-stalls at a later stage than given for the static stall case. This is usually described in diagrams as hysteresis loops showing the non-linear behaviour of the lift coefficient.

This phenomenon has been prevalent in stall regulated wind turbines with increasing diameters. Since this investigation is primarily concerned with variable speed, pitch controlled wind turbines, the time of operation spent in stall should be decreased and therefore the effects less. This instability is also usually short-lived within a rotational cycle as the amplitudes of the vibrations are stabilised by non-linear aerodynamic effects, i.e. periodic attaching and detaching flow regimes from retreating / advancing rotor relative to the wind field as it rotates.

2.1.2 Flap - Lag Instability (Stall Induced Vibrations)

The Flap-Lag instability is the result of a weakly damped lag (edgewise-in plane) mode coupling to the flapping (out of plane) mode. This instability has been observed in many stall regulated wind turbines of sizes ranging from 500 – 750kW [24].

The risk of Flap-Lag instability increases as the flapwise and edgewise blade natural frequencies approach each other. The amount of blade twist also plays a role; since this rotates the blade principle axes (uncoupled bending axes of origin through the blade elastic axis) out of the rotor plane such that blade in-plane and out-of-plane bending will have components in both Lag and Flap directions [1].

The wind turbine is at greatest risk when entering the region of stall where aerodynamic damping of the blade behaves non-linearly and effective negative aerodynamic damping can occur. The characteristics of dynamic stall are given in Figure 2.2.

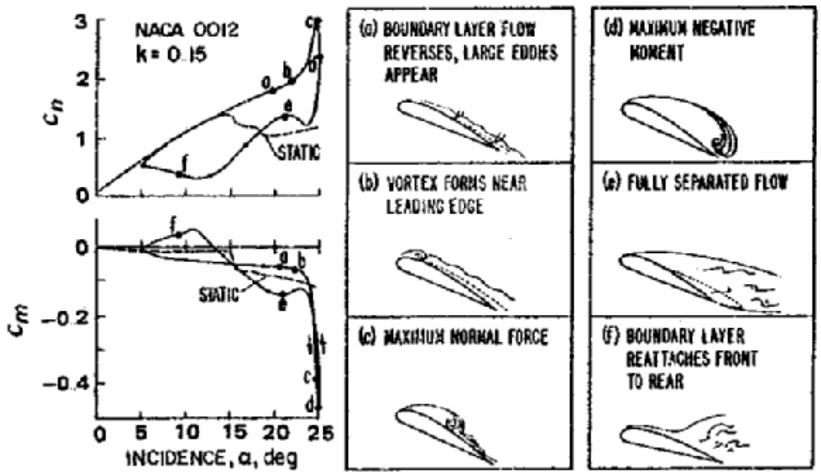

Figure 2.2 Lift and Moment Characteristics of an Aerofoil Undergoing Dynamic Stall

The underlying dynamics is a vortex forming and traversing the chord length until the maximum normal force is reached (stage c), after which stall occurs and the lift force almost instantaneously vanishes (stage e). This is when there is danger of negative aerodynamic damping and opens the door for the Flap-Lag instability to develop.

It is shown in the paper of van Holten [21], using the energy flow method, that energy transfer between the blade flapping oscillations and blade lag motion is possible for certain flap vibrational frequencies. These energy transfers can lead to an instability, especially in stalled flow conditions as is pointed out now.

Looking at the effect of blade flapping only, if sufficient damping exists, the flap oscillation amplitude is minimised and there is less force produced in the edgewise direction due to less Coriolis force variation. The coriolis force acts due to an effective shortened radius to the rotational axis of the rotor plane as a result of flapping angle (centre of mass moves towards the rotating axis), which accelerates and decelerates the blade in the edgewise direction – rotational plane. The Coriolis effect on the blade is shown in Figure 2.3.

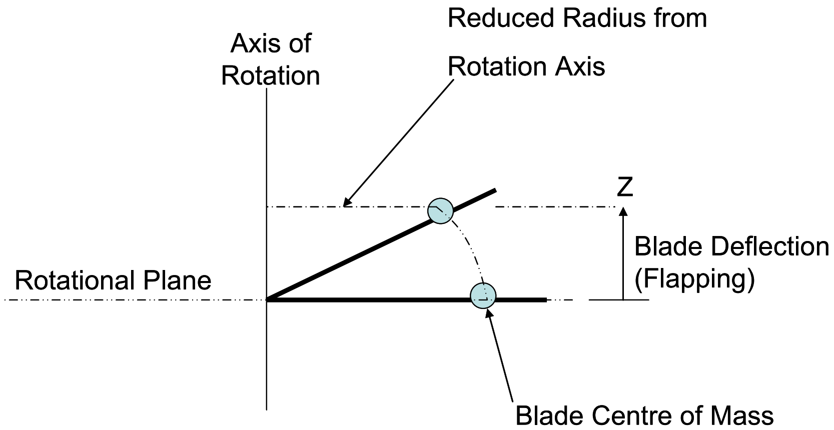

Figure 2.3 Edgewise Accelerations as a Result of Coriolis Effect for Flapping Motion (View: Top View of a Wind Turbine with Blade in Horizontal Position)

There is a built-in stabilising affect in that the flapping motion has the effect of tilting the lift force on the aerofoil such that a stabilising effect occurs on the edgewise accelerations due to the lift vector generating torque closer to the edgewise vibration plane [21]. A problem occurs however near the blade stall region where aerodynamic damping decreases or vanishes (refer to Figure 2.2) and if the phase of Flap-Lag motion is favourable (i.e. there is aerodynamic coupling occurring), the damping is lost and vibrations can grow quickly. In this case the stabilising coriolis effect is lost and increased edgewise vibrations can result.

It is also pointed out by van Holten [21], that a second mechanism near stall can exacerbate the problem. In this case, the drag coefficient is severely increased in stall and can diminish the tilting lift stabilisation effect from the blade flapping. This also means there is less damping on the flapping mode; further adding to the unstable dynamics, with possibly large edgewise vibrations occurring.

2.1.3 Classical Flutter (Flap - Torsion motion)

Classical Flutter is the term used to describe the dynamics of a blade undergoing coupled vibrations in the flapwise and torsional mode. Unlike the Flap-Lag instability, Flutter occurs in the region where flow is attached to the blade and aerodynamic forces vary linearly with angles of attack [8]. Again, it was shown qualitatively using the energy flow principle that energy transfer from the blade torsion motion to the flapping motion is possible due to components of the flapping velocity being in phase with the torsional excitation force. In turn, the same can be said for energy flow from the flapping motion to the torsional motion, providing the centre of gravity of the aerofoil is behind the quarter-chord (aerodynamic centre) line. Figure 2.4 illustrates a blade in a flutter mode, where the blade bending mode and torsion mode over a cycle of vibration is clearly evident. In the right phase aerodynamic coupling can occur and these bending modes can feed each other and grow in amplitude very quickly as is the case in the figure.

Figure 2.4 Graphic of Blade Flutter Mode Over One Period of Oscillation [9]

Looking at the coupling in another manner, pitch or torsional changes in the aerofoil section cause fluctuations in lift, causing the blade to flap, which in turn acts as an exciter for torsion through a changing angle of attack. When the lift and vertical motion of the blade are both working in the same direction, work is being added to the system. When the lift opposes the motion (damped) energy is being extracted. Therefore the Flutter can occur when the timing of torsion and flap motion is such that the lift over one cycle of motion is aligned with the flap motion [14]. This is illustrated in Figure 2.5.

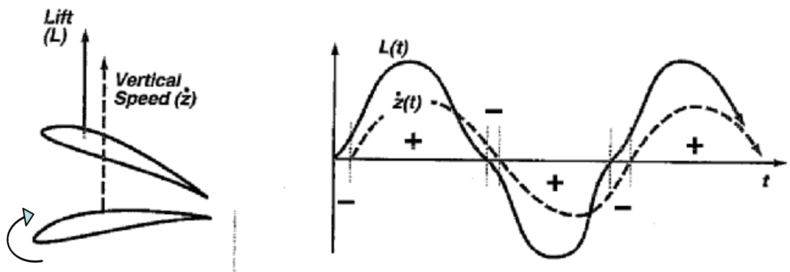

Figure 2.5 Work Added (+) to System due to Timing of Torsion & Flap Motion Aligning the Lift Vector [14]

Another important coupling arises due to the position of the centre of mass - gravity- of the blade as a result of flap and torsion, which gives contributions of the centrifugal force about the torsion axis for flap motion and in the radial direction of the blade, which acts through a moment arm provided by the centre of mass rotating out of the rotor plane due to torsion. This coupling and diagrammatical representation is given in section 3.1.4.5.

The conclusion is that with these two degrees of freedom pumping energy into each other, a condition could arise leading to an instability. While no known cases of failures due to Flutter have been recorded for wind turbines, the stability limit may be decreasing with increasing turbine rotor diameters, and hence, torsional natural frequencies.

For these reasons above, Stall Flutter would seem of less importance given that Classical Flutter and Flap-Lag instabilities could give rise to catastrophic failure more quickly. Therefore, these are considered in greater detail in the following section.

2.2 Historical Accounts of the Phenomena & Relevance to Wind Turbines

Stall Induced Vibrations (Flap-Lag Instability)

These were the first aeroelastic stability problems identified for horizontal axis wind turbines of rotor diameters around 40m and above. They were of the stall regulated variety and the instability was seen to emerge during the 1990s where an increase in rotor diameter for wind turbines was observed. This suggests that the extra flexibility of the rotor due to increasing blade radius plays an important role in this instability. The vibration in the edgewise directions can be considerable enough to cause high fatigue and lead to failure of the rotor blade. About a decade ago, there were instances of blade failures on the machines which saw the blade being hurled from the wind turbine quite some distance. While the cause was not stated, it is quite possible these were a result of fatigue initiated by stall induced vibrations on the stall regulated machines of this era.

On discovery of the problem, many experiments were conducted to understand the dynamics occurring causing the instability. This led to theoretical studies which confirmed the instability arising from energy supplied by aerodynamic forces during stalled operation

Fortunately, there are some post design solutions for wind turbines experiencing the problem; one is the fitting of stall-strips to the blade to change the stall characteristics and maintain aerodynamic damping. This is however at a certain cost of energy production [8].

In the design process, it is also possible to quell the problem through tailoring the structural dynamics of the wind turbine to maximise the overall blade motion to be vibrating out of plane (as opposed to the less damped in-plane motions) in its mode shapes to increase the overall aerodynamic damping. Subsequently, in the event of an effective negative aerodynamic damping due to stall, sufficient structural damping of the blades can be applied.

Classical Flutter (Flap -Torsion)

Classical Flutter has not been the cause of any failures in wind turbines and has been more prevalent in the operation of helicopters. Although current operational states of wind turbines is outside the Flutter stability limits, it is expected this gap is becoming narrower with the very large diameter wind turbines being produced with lighter more flexible materials, i.e. lower torsional stiffness.

There are no post design solutions for Flutter, but aerofoils can be structurally designed to be more resistant to Flutter. The most important parameters for counteracting Flutter in design are the frequency ratio between flapwise and torsional motion, chordwise position of aerofoil pitching axis and centre of gravity, and mass ratio between air and structure [8].

2.3 Analysis of Most Critical Instability

In the context of ever increasing rotor diameters over time, and the assumption of variable speed pitch regulated turbines being the prevalent design choice of the modern wind turbine, the question might be asked as to which aeroelastic instabilities become more critical. Typical questions to consider might be:

1. Are operating conditions and/or wind turbine designs more prone to a particular instability? Can they be taken into account or mitigated against, e.g. using trailing edge flaps? Which instability mechanism is more likely to occur?
2. How do the instabilities relate to scaling effects of wind turbines?
3. What are the future materials or design methods likely to be used in the future?

The following sections try to answer these questions to discover which instability may be more essential in future wind turbine applications. This would therefore prioritise the action to investigate the mitigation of the instability using an aerofoil with trailing edge flap geometry.

2.3.1 Occurrence / Operating Conditions for Instability

Stall Induced Vibrations (Flap – Lag Instability)

It has already been pointed out the greatest risk here is on the onset of stalled operation where a negative aerodynamic damping can exist to destabilise the dynamics. The first point to note is that on a variable speed, pitch regulated turbine, operation in stall conditions should be less than the previously stall regulated turbines. Therefore the stalled operation will occur predominantly from usual unsteady conditions such as in wind gusts or produced in yawed flow. If the stalled operation is less, then so should the occurrence of this instability.

The second point is that due to the varying inflow over a rotational cycle in these conditions, limit cycle behaviour is observed and so the instability is limited to within a cycle. This is because eventually the flow reattaches to the blade and damping is restored, which occurs cyclically and does not let the dynamics become fully unstable. Nevertheless, these vibrations could result in a higher fatigue rate [24]. It is considered for the vibrations to be of a destructive mode in this case, the edgewise vibrations would need to couple with the tower motion. This is another class of instability called the edgewise / sideways tower instability.

This instability can be mitigated against using full aeroelastic design of the wind turbine or changing the behaviour of stall using strips attached to the blade, meaning post design solutions are possible, which is an advantage over Classical Flutter.

It is thought that trailing edge flaps would not be as effective in treating this instability because the flaps would have less impact on edgewise motion, since it mainly serves to affect out of plane dynamics by directly interfering with the lift force.

The third and final point should be the consideration of increased flexibility of the rotor blades (more slender blades) due to scale effects and how the eigenfrequencies are affected. This may bring the edgewise and flapwise eigenfrequencies closer together to form a resonance instability. As stated earlier, dynamic instabilities are considered to cause responses more quickly in time than resonance. Section 2.3.2 investigates the scaling effects of wind turbines.

Classical Flutter (Flap – Torsion)

Classical Flutter can occur more readily in steady conditions (attached flow – not in stall) and compared to the previous case, the danger here is that flapping inertias have a direct effect on torsion, and therefore increases the excitation forces for this mode. Therefore, the aerodynamic damping could have less influence over this instability if torsional stiffness is low enough such that deflections are relatively significant and in low enough frequency where both mechanisms continue to feed each other energy (i.e. the inherent damping in flap motion is negated by an associated torsion angle, which if in the right phase to flap motion, will reduce the overall damping). While both instabilities rely on aerodynamic damping, it may be less effective at suppressing classical Flutter due to the blade flapping inertial influences directly on torsional motion.

Therefore, the operating conditions for this instability depend on the flapping and torsional response from aerodynamic and inertial loads. If Flutter was to occur, this could very well lead to catastrophic failure of the rotor blade in a short time. Since this can happen with attached flow over the blade, it makes occurrence over the Flap – Lag problem higher, particularly in the context of future large wind turbines.

Unlike the Flap-Lag case, there are no limit cycle occurrences which periodically stabilise the situation for Flutter. There are also no post design solutions to Flutter; it will occur if the right conditions prevail for a blade of given structural properties. It is considered for future wind turbines, the structural properties of the blade will be suitably flexible for experiencing Flutter given current operating conditions for wind turbine (i.e. tip speeds). It is thought that trailing edge flaps could play a role in stabilising the onset of Flutter. Since flap motion is important for the coupling to cause Flutter, a trailing edge flap could possibly change the dynamics suitably to keep the turbine stable.

2.3.2 Scaling Effects - Reducing Natural Frequencies

Scaling Effects

It has been emphasised so far that the above instabilities may feature more heavily with larger rotor blades. Flap-Lag dynamics were observed in turbines of rotor diameters around 40m, so it could be expected Flutter could also emerge in the future as a potential problem.

To assess these scale effects, since rotor blade eigenfrequencies play a vital role in the dynamics, it is logical to determine how they might vary. Van Holten, Pavel & Smits [22] showed through the square cube law, the blade eigenfrequencies scaled according to those in Table 2.1.

Table 2.1 Scaling of Blade Eigenfrequencies

	Flap	Lag	Torsion
Square Cube Law	$1/R$	$1/R$	$1/R$
Experimental	$1/R^{0.8}$	$1/R$	-

The flap and lag eigenfrequencies were also measured experimentally and showed the flap frequency reduces more slowly than the lag frequency with increasing radius. The significance of this is the frequencies will converge on each other for larger turbines. Therefore, smaller vibrations (flap and lag) in normal turbine operation will be closer to their natural frequencies, thus making the coupling result in possibly worse vibrations in the event of stall.

If it is assumed the blade torsional frequency also behaves according to the square cube law, the natural frequencies in the bending-torsion mode will also coincide with increasing radius. To reinforce this idea, a Flutter experiment conducted on a rotor blade by Hansen [8] showed that aeroelastic damping of the torsional mode decreases as the torsion natural frequency decreases; to become negative at a critical velocity at which Flutter begins.

This would indeed suggest that larger wind turbines will inevitably experience Flutter problems due to increased flexibility of rotors in the torsional mode. This would become a critical design issue in larger turbines since it is certainly likely that the critical torsion frequencies for Flutter will interfere in normal wind turbine operation.

2.3.3 Blade Design

Larger blades will require design changes to account for increased loading while maintaining tight constraints in manufacturing cost and blade mass. For larger wind turbines, this means smaller operating speeds, less centrifugal stiffening and higher in-plane (edgewise) forces from gravity effects. A common structure for large blades is the use of a composite box beam or "D spar" to carry the bulk load; the rest being taken from the blade skin. It is considered if this method is continued for even larger say 7-10MW turbines of the future, in-plane natural frequencies will become closer to excitation levels [27].

The blade material is usually made from a composite material for large turbines. Common resins used in composites are polyester, vinyl ester and epoxy, with the first two being mostly used, but the trend seems to be moving toward epoxy because of better material properties.

Current research on rotor blades is aimed at using composite materials, laminate stacking sequences and ply angles to increase the damping of blades in flapwise and lagwise directions. A study has been recently conducted assessing different matrix materials (polyesters, epoxy, adhesive putty) and glass-aramid based fibre systems [5] for increasing effective damping. In a full model test of a blade with a different layer structure (different ply angles) and materials, a total modal damping ratio of 94% and 104% was exhibited in the flapwise and edgewise directions respectively, compared to a baseline blade of today. This optimised composite stacking also had an effect on the eigenvalues of the blade, which showed a small reduction in frequency due to reorientation of the fibres.

Therefore, it would seem that new blade material and designs used in the future could offset some of the flexibility problems associated with larger blades. However, the natural frequencies of the blades will still decrease with size. The increased damping would be welcomed for in-plane motion, since this is a concern in stalled conditions.

In summary:

Both Flutter and Stall Induced vibrations are major concerns for future, larger wind turbines. However, in consideration of the statements above, it is the author's opinion that Classical Flutter will become a critical design issue for larger wind turbine blades for the following reasons:

- Torsional flexibility will increase with larger radius, making the blade more prone to Flutter
- No limit cycle occurs over a revolution (i.e. not periodically stabilised due to unsteady aerodynamics as the rotor rotates)
- Flutter dependent on ratio of flap motion to torsion, and therefore can occur even if blade flapping is being damped (if damping maintained for Flap-Lag, should help to keep stable)
- Pitch control of the blade could act as an exciter for this instability, whereas for Flap-Lag, the pitching helps to keep the blade out of the stalled region (advantage)
- No aerodynamic post design solution exists for Flutter (i.e. stall strips can be fitted to aerofoil to smoothen stall for Flap-Lag case).
- Careful design considerations of the blade aerofoil will have to be made if able to resist Flutter, e.g. special blade design possibly deviating from best current manufacturing practices will have to be developed

It is considered the Flutter margin will be within normal operating limits of turbines with larger blades, while Flap-Lag could be contained with increased structural damping of the blade and tuning of the turbine modal dynamics such that the tower can be used to dampen edgewise vibrations. However, if the Flap-Lag motion were to couple with that of the tower, there is the possibility of another instability arising, which again must be considered in the modal damping of the turbine at design phase.

3 Dynamic Model for Investigating Classical Flutter

This chapter identifies the methodology and theory utilised in the thesis for investigation of the 'Classical Flutter' instability of a given wind turbine. It includes the development of the aeroelastic model (section 3.1.2 to 3.1.5) for a wind turbine rotor configuration and an explanation of the simulation environment with brief descriptions of relevant sub-functions and relationships so that an overview of the simulation model is obtained. Following this, a method to investigate the Flutter limits of the turbine configuration is outlined in section 3.2 in preparation of the final objective; to investigate the controllability of 'Flutter' using trailing edge geometry.

The core topics include:

- Wind turbine configuration and blade section structural properties
- Overview of the aerodynamic model (BEM & Theodorsen theory)
- Detailed analysis of the structural dynamic model – Modal Analysis
- Overview of the aeroelastic coupling between torsion and flapwise bending
- Classical Flutter Stability limit determination procedure

The realisation of these steps into an effective simulation model allows a platform to be built for including actuated trailing edge geometry and assessing the impacts on controlling the Flutter phenomenon, which is the topic of section 5.

3.1 The Aeroelastic Wind Turbine Model

3.1.1 General

Aeroelasticity refers to the interdependence (coupled effect) of the structural dynamics and aerodynamics of the rotor. The coupling effect is due to the aerodynamic forces (via the external wind field) being dependent on the aerofoil position and accelerations (response) relative to the wind field in time, thus making it necessary to model the turbine as a linked system for an accurate dynamic analysis. This linking of the aerodynamic and structural dynamic – aeroelastic system is summarised in Figure 3.1 [11].

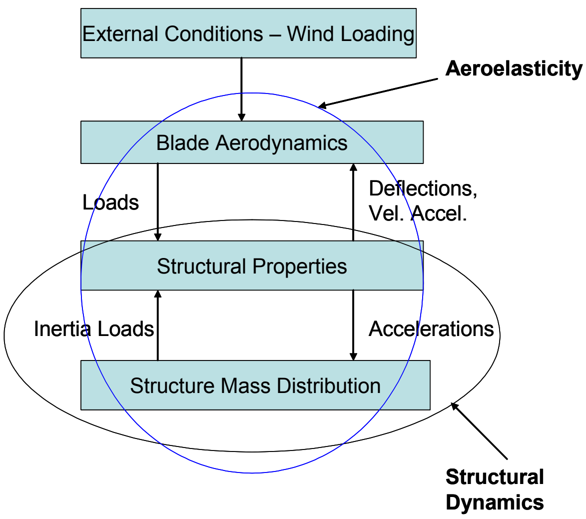

Figure 3.1 The Coupling of the Aerodynamic and Structural Dynamic Models

The figure shows that structural dynamics consists of two parts, the response of the structure based from its elastic properties (causing deflections, accelerations, etc), and the inertial loads according to the structures mass distribution. Consideration of inertial loads is vital since it relates to the natural frequencies of the system and indicates the oscillatory manner of the response. For example, according to Figure 3.1, without accounting for the inertia would mean the blade position and accelerations are not accounted for to update the aerodynamic information, thereby giving a false representation of the dynamics.

The importance of aeroelastic models for design are increasingly important nowadays since the drive towards larger turbines is demanding more flexible components (e.g. rotor blades) for reducing both mass and cost of manufacture, which means more attention needs to be given to the structure eigenfrequencies to ensure stability. Currently, there are three types of models used for structural dynamics in aeroelastic computations [25]:

- Models based on finite element methods;
- Models based on modal representation of the turbine with modal stiffness and masses; and
- Models based on multi-body formulation

The assumptions in applying these models are that the deflections are small and aerodynamic loads can be applied to the undeformed structure; both of these reaching their outer limits with the larger and more flexible turbines of today [25].

The finite element method models the rotor structure as simple beams under load. A disadvantage of this method is the amount of computational time required for a multi-degree of freedom system. The same can be said for multi-body formulation. The most commonly used model in design codes is the modal representation, which is considered to have advantages of providing reliable dynamics of the wind turbine with few degrees of freedom- meaning less computation time [32]. As such, a modal approach has been adopted for this study and is introduced in Section 3.1.4.

3.1.2 Wind Turbine Configuration

3.1.2.1 Modelling Assumptions

A thorough investigation into the behaviour of wind turbines operating in an unsteady environment demands a full aeroelastic analysis comprising of interactions starting at the rotor and cascading on down through the nacelle and tower foundation. While this would be desirable in the current investigation into classical Flutter occurrence, here a simplified approach has been adopted. The wind turbine represented here assumes an infinitely stiff tower with the rotor blades fixed to a rigid hub (no hinge offset). While this impinges on the real aeroelastic interactions experienced by a wind turbine, it is sufficient to capture the stability margins and analyse the effect of trailing edge flaps. Inclusion of tower interaction would invariably alter the aeroelastic interactions, but this should not detract from the ability of testing if trailing edge geometry can control the Flutter stability limits.

A further simplification is that one blade is modelled only so that multiple blade interaction effects can be neglected, which should make the dynamics and effects of an actuated control flap more transparent later in the analysis. A schematic of the model is given in Figure 3.2.

The blade used for the initial development of the model is that from the UpWind project. This wind turbine is based on a 5MW, 3 bladed design with a rotor diameter if 126m. The UpWind project is a joint European investigation into the design of the next generation of wind turbines up to and beyond 10MW. The UpWind turbine is a fabricated design, using design characteristics taken from existing commercial designs. The relevant blade structural data used in this study is given in Appendix A.II.

The more pertinent properties are listed in Table 3.1.

Table 3.1 UPWIND Wind Turbine Design Characteristics

Rated power	5MW
Number of blades	3
Rotor Diameter	126.0m
Hub Diameter	3.0m
Hub Height	90.0m
Maximum Rotor Speed	12.5 RPM
Hub Overhang	5.0m
Shaft Tilt Angle	5.0^{o}
Rotor Pre-cone Angle	-2.5^{o}

Further to the above assumptions, the UpWind rotor blade rotating axes are assumed to coincide with the rotational plane, i.e. pre-cone angle equal to zero, and the rotor plane orientated perpendicular to the wind field, i.e. tilt angle equal to zero (avoidance of yawed flow conditions in normal turbine operation).

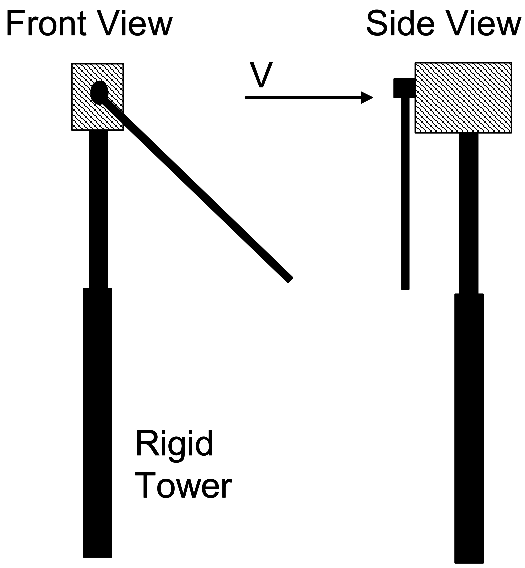

Figure 3.2 Schematic of Wind Turbine Configuration

3.1.2.2 Model Coordinate System

The coordinate systems for the dynamic model are illustrated in Figure 3.3 and Figure 3.4; being that of a rotational blade coordinate system located at the hub centre. Within the rotating system, another coordinate system in the principle axes of the blade exists (the x' axis represents the elastic axis of the blade – EA as specified below). In the principle axes, the curvature of the elastic axis due to flapping and edgewise deflections can be translated to the rotational coordinate system whilst accounting for the twist of the blade (pitching, design twist and elastic deflection under the aerodynamic moment and moment from the lift acting over an offset arm to the shear centre), as indicated in Figure 3.4.

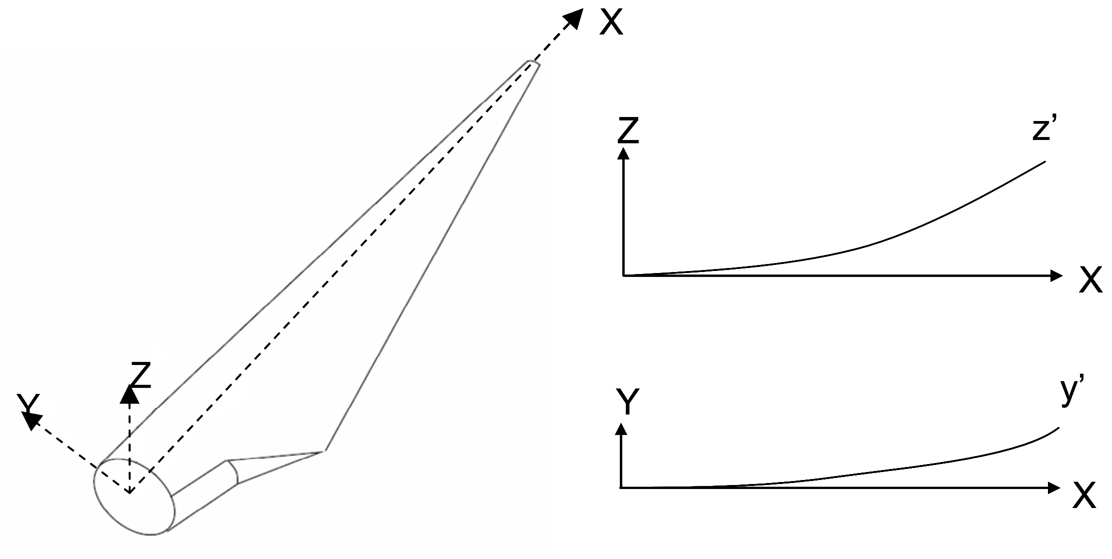

Figure 3.3 Rotating Blade Coordinate System - X aligned with undeformed Elastic Axis (EA)

Upper right - out of plane flapping

Lower right – in-plane deflection

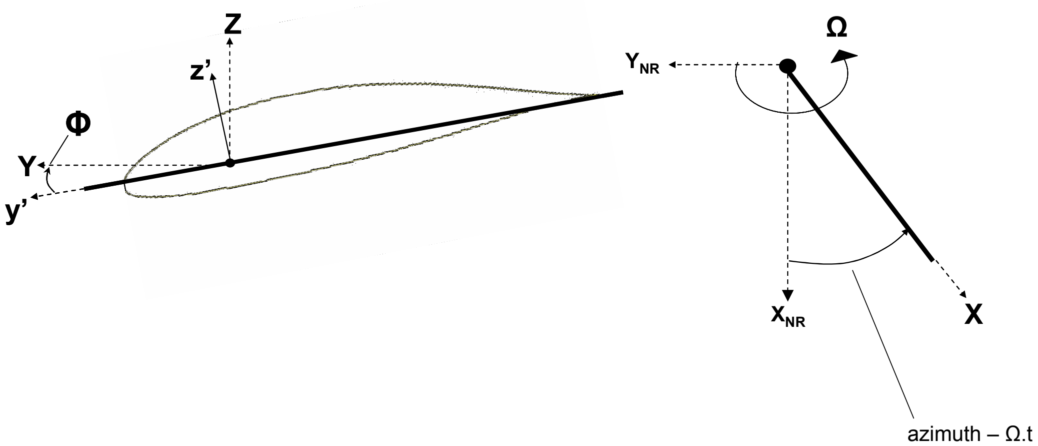

Figure 3.4 Left – Blade Section Indicating Principle Axes and Blade Torsion about Elastic Axis (EA) (perspective from undeformed state – z' = y' = 0)

Right – Front View of One-Bladed Rotor with Not Rotating Coordinate System at Hub

It should be noted that the angle between the Y- axis and the y' – principle axis (along the chordline) is just the built-in twist angle of the blade, being defined zero at the blade tip chord line. The total local twist angle Φ of the blade represents the built in twist, pitching and torsional elastic deformation of the blade.

The transformation from the deflections in the rotating blade system to the non-rotating system involves a rotation about the Z-axis only and is made as follows:

$$\begin{bmatrix} X_{NR} \\ Y_{NR} \\ Z_{NR} \end{bmatrix} = \begin{bmatrix} \cos(\psi) & \sin(\psi) & 0 \\ -\sin(\psi) & \cos(\psi) & 0 \\ 0 & 0 & 1 \end{bmatrix} \begin{bmatrix} X \\ Y \\ Z \end{bmatrix}$$

Where ψ is the blade azimuth from the 6 o'clock (downward) position.

The transformation from the principle axis (x', y', z') to the rotating blade axis (X, Y, Z) is made on the curvature of the elastic axis, details of which is given in section 3.1.2.4.

3.1.2.3 Aerofoil Section Structural Characteristics

The inclusion of the torsion DOF into the dynamic model requires rotational inertias to be specified for the blade as well as structural properties defining the extra inertias due to misalignment of the blade section centre of gravity (y_{cg}) and aerodynamic centre (y_{ac}) to the shear centre. It is assumed for the current model that the flapwise and torsion spring coincide at elastic axis (EA) to simplify the structural coupling, which is at the origin of the principle axis as depicted in Figure 3.5. The torsion deflection will be measured about the EA and include moment contributions due to centre of gravity (y_{cg}) and aerodynamic centre (y_{ac}) offset from shear axis.

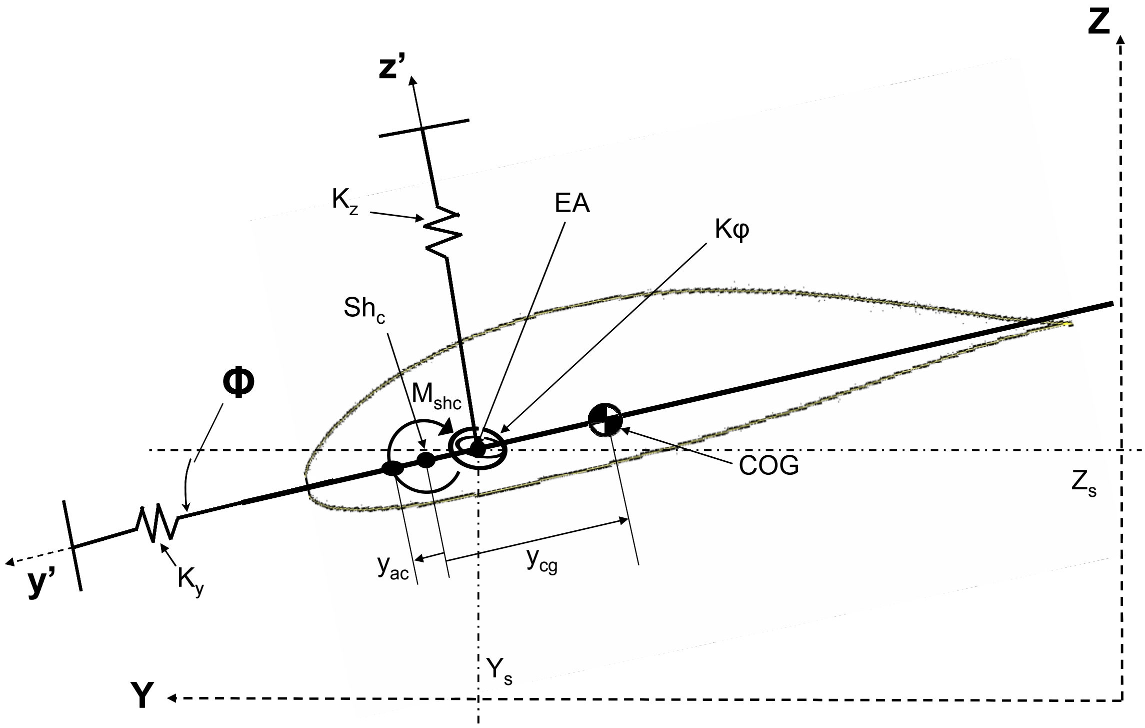

Figure 3.5 Blade Section Structural Characteristics Used in Dynamic Model (perspective given for arbitrary blade bending in Y and Z)

The properties in the figure are defined as:

- EA is the elastic axis (origin of principle axes – x')
- y', z' are the principle axes
- Z_s and Y_s are the blade section deflections of the EA in the blade coordinate axes
- M_{shc} is the total moment about the shear centre including that from the aerodynamic moment, the lift acting over the moment arm from the aerodynamic centre offset; and that contributing from the centre of gravity offset.
- COG is the centre of gravity for the blade section
- Sh_c is the shear centre - defined as where an in-plane force does not rotate the aerofoil [15].
- y_{ac} and y_{cg} (y positive towards leading edge) are the distances of the aerodynamic moment and centre of gravity from the shear centre respectively
- k_z, k_y and k_φ represent the flap, edgewise and torsion spring stiffness respectively

It should be noted that properties such as the aerodynamic centre and centre of gravity offsets change along the span of the blade, as do the respective spring stiffness values. The spanwise structural properties can be viewed in Appendix A.II.

In the configuration shown in Figure 3.5, the COG contributes positively (nose up) to the aerodynamic moment (M_{shc} clockwise is positive) as it is located behind the EA. It is possible at another point along the blade; it is in front of the EA, which constitutes a negative contribution to the total moment. This needs to be considered later in the analysis when formulating the generalised mass and stiffness for blade torsion.

The parameters y_{ac} and y_{cg} are important for defining the rotational inertia from displacements and accelerations in the Z-axis.

3.1.2.4 Coordinate Transformations for Torsion - Flap – Edgewise Coupling

The transformation of the deflections from the principle axes to the rotating blade axes as depicted in Figure 3.5 is complicated due to the built in twist, pitching and elastic deformation of the blade, represented by:

3.1

$$\Phi = \varphi_p + \varphi_t + \varphi_e$$

where,

φ_p is the blade pitch angle [deg]

φ_t is the blade twist [deg]

φ_e is the elastic deformation [deg]

The uncoupled blade deflections in the principle axes have components in both the in-and-out of plane directions *(Y, Z)* and due to changing twisting angles, Φ, along the span (also changing in time), a coupling effect arises [1]. The radial twisting of the blade means that when for example, out of plane deflections are given in the rotating blade frame; there is also a small deflection in-plane. The same can be said for in-plane deflections, which causes out of plane motion.

For an accurate account of the Flutter problem, it is desirable to include this coupling and can be done so using a trigonometric transformation on the curvatures of the elastic and blade axes, as shown by Eq. 3.2. [1].

3.2

$$\frac{d^2Z}{dX^2} = \frac{d^2z'}{dx'^2} Cos\Phi - \frac{d^2y'}{dx'^2} Sin\Phi$$

$$\frac{d^2Y}{dX^2} = \frac{d^2z'}{dx'^2} Sin\Phi - \frac{d^2y'}{dx'^2} Cos\Phi$$

Eq. 3.2 can be solved in terms of the modal approach discussed in the following sections, where the uncoupled deflection modes (e.g. z') are numerically integrated (using deflection correction functions) to approximate the transformation given deflections in-plane and in the presence of span varying torsion. The deflection correction functions as given by [1] are given in Appendix A.I.V.

3.1.3 Aerodynamic Model

The aerodynamic model makes use of the Blade Element Momentum method (BEM) and is designed for both quasi-steady and unsteady aerofoil aerodynamics using modified

'Theodorsen' theory. Theodorsen and other aerodynamic relations are given in full in Appendix A.I.

BEM theory forms the backbone of current wind turbine design codes which utilises fundamental physics concepts, such as conservation of mass, momentum and energy of inviscid flow to describe the behaviour of the global and local flow fields about the rotor and aerodynamic forces on a blade element. The model represents the rotor as an actuator disc within a stream tube (control volume) where axial and angular momentum and energy balances of the flow over the actuator disc are taken [7]. The thrust over the disc can be determined using the flow conditions upstream, downstream and the induced velocity (induction factor) at the actuator disc itself (or rotor). These forces caused at the rotor given by momentum theory can be assumed equal to the forces described by 2D Blade Element Theory, which is the breakdown of aerodynamic forces on elements of a blade taken from aerofoils with known lift and drag coefficients at given angles of attack [3]. This provides a fast way to examine the aeroelastic behaviour, or structural response of the blade for given wind conditions entering the rotor plane. In the case of Theodorsen's model, lookup tables are not required, as the lift coefficient is determined from the flow properties.

BEM theory is a well known method, thus given here is only a brief summary of the relevant theory used in the current aeroelastic model. For the purposes of this study, the BEM model with modified Theodorsen theory for lift was acquired from an internally designed Simulink code developed within TUDelft Wind Energy Department (WIMSIM – Wind Turbine Integrated Module Simulation) [19]. Slight adaptations have been made here to interface it with the new structural model to be described in section 3.1.4.

Aerodynamic Model Assumptions

The effects of wake rotation has been neglected (no tangential induction factor) and the axial induction factor is assumed to be constant over the rotor disc. There is also no empirical tip loss or dynamic stall model installed. Not having dynamic stall is not an issue for this study, since the Classical Flutter phenomenon occurs in attached flow conditions. The drag and moment coefficients are determined via lookup tables, since the capability was not already existing in the current model.

The model however does account for the turbulent wake state (higher thrusts) as well as a first order differential equation for the dynamic inflow. This allows for the time it takes the wake to equilibrate after a disturbance at the rotor. The Aerodynamic relations underlying the WIMSIM module is given in Appendix A.I. The following is a summary of the key relations.

Momentum Equations

The axial induction factor is found from 1D (steady, inviscid) momentum theory as:

3.3

$$C_{Dax} = 4a\left|1-a\right|$$

while an empirical relation is used for the turbulent wake state:

3.4

$$C_{Dax} = \frac{2.708}{1.991-a} \quad 0.5 \le a \le 1.62$$

where:

C_{Dax} is the axial aerodynamic force coefficient [-],

a is the axial induction factor at the disc [-].

Blade Element Equations

A blade element with the definitions of velocities, angles, forces and moments can be seen in Figure 3.6. From this the blade element theory can be described.

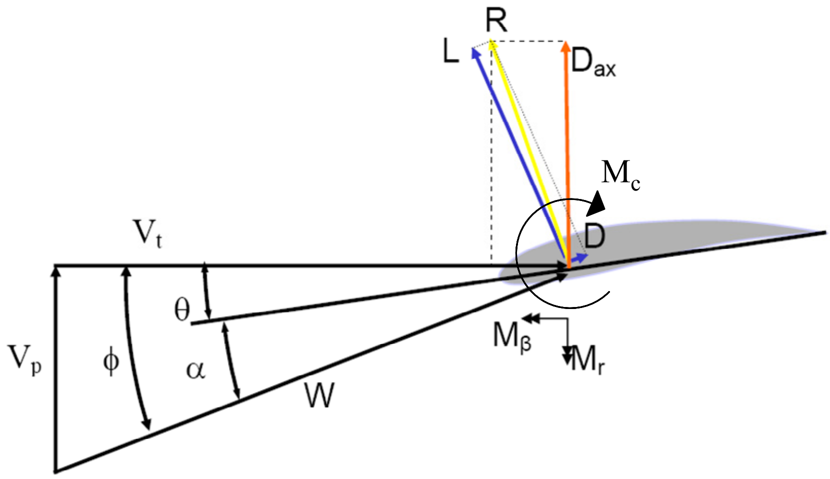

Figure 3.6 Blade section with definitions of velocities, angles, forces and moments

In case of the quasi-steady aerodynamics the perpendicular velocity component becomes (for rigid tower):

3.5

$$V_p = V\left(1-a\right)-\dot{Z}$$

where:

V is the local wind speed (i.e. mean wind speed plus wind disturbances) [m/s],

$\dot{Z}$ is the out of plane blade velocity [m/s]

Similarly, the tangential velocity component V_t becomes:

3.6

$$V_t = \Omega r - \dot{Y}$$

where:

$\dot{Y}$ is the in-plane velocity of the blade [m/s]

Ω: is the angular velocity of the rotor [rad/s]

r is the radius of the blade element [m]

From these quantities, the relative wind speed (W) and inflow angle for each blade element can be determined in the usual manner according to the definitions and geometry of Figure 3.6.

For determination of total lift, drag and moment on each blade section, the respective coefficients can be obtained from specific aerofoil data at given angles of attack in the case of quasi-steady aerodynamics, or through using the modified Theodorsens approach to determine lift only, as is the case with simulation of a trailing edge flap. With lift, drag and moment coefficients per section known, the following important loadings on the rotor are found [18]:

3.7

$$L = \int_0^R c_l \frac{1}{2}\rho W^2 c\, dr$$
$$D = \int_0^R c_d \frac{1}{2}\rho W^2 c\, dr$$
$$M_c = \int_0^R c_m \frac{1}{2}\rho W^2 c^2\, dr$$

where:

c_l is the Lift coefficient [-],

c_d is the Drag coefficient [-],

c_m is the Moment coefficient [-]

ρ is the air density [kg/m^3],

c is the chord length [m],

dr is the length of a blade element [m].

Again, as per in the usual manner, the thrust coefficient, flapping moment and aerodynamic rotor torque can be obtained using the geometric properties of Figure 3.6 and summing the components of each blade section (Refer Appendix A.I.).

3.1.3.1 Unsteady Aerofoil Aerodynamics

The unsteady model has been developed for calculating the lift coefficients of an aerofoil in arbitrary motion and wind gust field using Theodorsens theory, modified by the Wagner and Küssner functions. The necessity for such a model will become apparent in later sections when trailing edge flaps are added to the aerofoil, which will have a significant impact on the local and global flow fields, and hence aerodynamics. The model is capable of determining the unsteady lift coefficient due to an arbitrary trailing edge flap deflection using a summation of the non-circulatory and circulatory regions of the flow. The non circulatory lift coefficient is given by [17]:

3.8

$$c_{l,nc} = -\frac{\pi c}{2W^2}\left(\ddot{Z} + W\dot{\Phi} + \frac{\Omega}{W}\dot{\Omega} r^2 \alpha_{qs} + \frac{c\ddot{\Phi}}{4}\right) - \frac{c}{2W^2}\left(F_4 W\dot{\delta} + \frac{cF_1\ddot{\delta}}{2}\right)$$

where:

α_{qs}: is the quasi-steady angle of attack due to a pitch and plunge motion [rad]

δ is the trailing-edge flap deflection [rad]

E is the non-dimensional trailing-edge flap hinge location in semi-chords [-]

W is the relative wind speed [m/s]

dot=d/dt: first time derivative [1/s]

Φ is as defined in Eq. 3.1

The circulatory component is given via Duhamel's superposition integral with the Wagner indicial step response H and the Küssner gust entry function Ψ as given in [17]:

3.9

$$c_{l,c} = \left(c_{l,c}\right)_{\alpha} + \left(c_{l,c}\right)_{\delta} + \left(c_{l,c}\right)_{w_g}$$
$$= 2\pi \left(\alpha_{qs}(0)\mathrm{H}(s) + \frac{1}{V}\int_0^s \frac{d\left(V\alpha_{qs}\right)}{d\sigma}\mathrm{H}(s-\sigma)d\sigma + \delta_{qs}(0)\mathrm{H}(s) + \int_0^s \frac{d\delta_{qs}}{d\sigma}\mathrm{H}(s-\sigma)d\sigma + \frac{w_g(0)}{W}\Psi(s) \right.$$
$$\left. + \int_0^s \frac{dw_g}{d\sigma}\Psi(s-\sigma)d\sigma \right)$$

and

3.10

$$c_l = c_{l,nc} + c_{l,c}$$

where:

s is the non-dimensional aerodynamic time [-]

w_g is the downwash velocity [m/s]

δ_{qs} is the quasi-steady angle of attack due to a trailing-edge flap deflection [rad]

H is the Wagner function

Ψ is the Küssner function

In these, the quasi-steady angle of attack α_{qs} and the quasi-steady angle of attack due to trailing-edge flap deflection δ_{qs} are given with respect to the initial steady state values. The non-dimensional parameter s is the aerodynamic time based on semi-chord lengths of the airfoil travelled:

Further aerodynamics and geometric considerations concerning the trailing edge flap is identified in Section 5.

Finally, the quasi steady aerofoil angle of attack is given by:

3.11

$$\alpha_{qs} = \varphi + \Delta\varphi - \left(\Phi + \frac{\dot{\Phi}c}{2W} + \frac{\dot{Z}}{W} \right)$$

Where,

φ is the inflow angle [rad]; and other variables as defined previously.

The above relationships are coded in state-space format and solved to an indicial method. A thorough description of the unsteady model equations can be found in the WIMSIM module [19]. An excerpt is given in Appendix A.I, with also some validation of the installed code.

3.1.4 Structural Model

The structural model makes use of a modal approach wherein the rotor blade is represented as a cantilever beam, which has both a distributed mass and stiffness, and inbuilt twist about the radial axis (X). A modal analysis makes use of such a beam that is loaded to determine the deflections, velocities and inertias using generalised coordinates, which define the amount of structural displacement according to specified modeshapes of the beam.

Mode shapes represent the degrees of freedom (DOF) of the system under investigation and are related to the 'eigenfrequencies' (natural frequency) of the beam, at which the blade exhibits a pre-defined response according to its mass and stiffness distribution called an 'eigenmode'. It should be stressed; the reason for defining modeshapes is to eliminate the number of (infinite) DOF of a system with continuous, distributed mass so that the dynamic equations are simplified and computational time is minimised. This is possible due to the 'orthogonality' property of eigenmode shapes, which states that each mode vibrating with different natural frequencies can be uncoupled from each other, since all other combinations of the modes must result to zero amplitude according to Eq. 3.12 [1].

3.12

$$\left(\omega^r - \omega^p\right)\sum_{i=1}^{n} m_i u_i^p u_i^r = 0$$

Where,

$\omega^{r,p}$ is natural frequency of two modes, e.g. 1st and 2nd natural frequencies

$u_i^{p,r}$ is the amplitudes of vibration for pth and rth modes

m^i is a concentrated mass

Thus, for two modes with $\omega^r \neq \omega^p$ ($r \neq p$ and frequency non-zero), then $_{i}u_i^p u_i^r$ must be zero for $r \neq p$. This provides a convenient simplification to the dynamics because the equations of motion can be represented as multiple-uncoupled single degree of freedom systems using mode shapes constrained by the orthogonality principle [1].

A convenient method to find the mode shapes of a beam is to discretise the blade into finite lengths and use a lumped-mass procedure and define the displacements and accelerations at these points only [4]. This avoids the need for complicated partial differential equations to model the dynamics since variables of position along span and time would have to be included if all inertia forces were defined for all points[1]. A discretised blade relevant for the task at hand is shown in Figure 3.7.

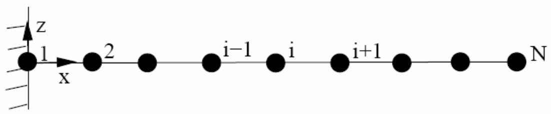

Figure 3.7 Cantilevered Discretised Blade Showing N Concentrated Point Masses

In this model, it is assumed the structure supporting the point concentraion is included in this lumped mass and the structure itself considered as being weightless [4]. An iterative method can be applied to determine the eigenmodes of the beam to represent the DOFs of interest for this study; namely the blade flapwise, edgewise and torsion direction. This procedure is given shortly. The number of eigenmodes for each direction included depends on the accuracy required, but usually most of work done in bending is captured in the first two to three eigenmodes (lowest natural frequencies), and decreases for higher ones.

An example of the shape of typical first (DOF one) and second (DOF 2) flapwise eigenmodes (deflection out of rotor plane) is given in Figure 3.8. The mode shapes are usually normalised so that the tip deflection is equal to 1, which is useful for later on when generalised forces are applied on the blade.

[1] Note: in a modal representation, this time dependence is replaced by the generalised coordinate, which advances the concentration points of the modeshape in time to arrive at the dynamic response. This requires the use of the virtual work principle, which is explained in 3.1.4.2.

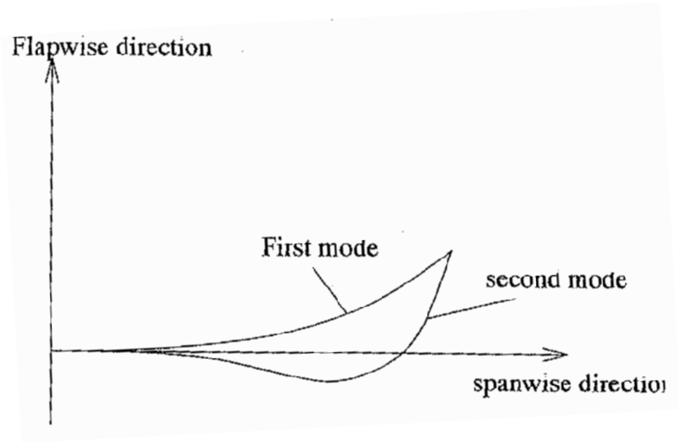

Figure 3.8 First and Second Eigenmode of Blade Flapwise Deflection

3.1.4.1 Determination of Blade Eigenmodes (Mode Shapes)

The examination of the classical Flutter instability phenomenon requires at least the flapwise and torsion DOF, since these are the primary coupling components. For completeness, the first blade edgewise DOF is also included, which will give a more realistic aeroelastic model in terms of the influence on the blade inflow conditions. The following outlines the procedure used to determine the UpWind blade eigenmodes. Appendix A.III details the applied algorithm.

1st, 2nd Flapwise Eigenmodes

These eigenmodes may be calculated in various ways, but due to the limited number of eigenmodes required, the simple Stodola iteration process is adopted here. This procedure is given by Hansen [11] and Clough [4], and with reference to the lumped-mass discretised blade of Figure 3.7 and considering deflection in the x'-z' and x'-y' plane (Figure 3.3), is based on the relationship of Eq. 3.13.

3.13

$$P^i_{z'} = \omega^2 m^i u^i_{z'}$$
$$P^i_{y'} = \omega^2 m^i u^i_{y'}$$

where,

$P^i_{z',y'}$ is the inertial loading in the respective coordinate planes [kg.m.s^{-2}]

ω is the frequency of vibration [rad/s]

m^i is the concentrated mass at point i I along the blade [kg]

$u^i_{z'}$ is the static deflection (z') at point i along the blade [m]

$u^i_{y'}$ is the static deflection (y') at point i along the blade [m]

The multiplying term $\omega^2 m^i$ is simply the stiffness of the blade at each section, as will be shown in a later section.

Eq. 3.13 can be used in an iterative procedure which will converge to the lowest eigenfrequencies, and therefore eigenmodes of the blade. The process converges to the first flap mode shape by first assuming a constant loading along the blade, which estimates deflection at all respective points on the blade according to Eq. 3.13.

This in turn produces new inertias and deflections until it reaches a static equilibrium state for a certain frequency (the lowest natural frequency), hence defining the mode shape, i.e. the first flap mode (defined here as $u_{z'}^{1f}$).

Since the inertial loading is given at discrete points on the blade, the deflections may be computed numerically by assuming a linearly varying force between the points and integrating to determine the bending moments in the blade. Curvatures $\left(\partial \big/ \partial X^2 \right) u_{z'}^{1f}$ are then determined using blade stiffness and are integrated to identify the rotation (deflection gradient or slope) and deflection at each point.

The Stodola procedure can be easily implemented into a Matlab routine for determination of the 1st flapwise mode. The entire iteration sequence is given as according to Hansen [11] in Appendix A.III.

The eigenmodes determined are the uncoupled modes in the principle blade axes (x', y', z'), which undergo a transformation to the in-plane and out-of plane axes as described in section 3.1.2.4.

1st Edgewise Eigenmodes

Until now, only the first flapwise mode is known. To determine the first edgewise ($u_{y'}^{1e}$), a similar procedure is followed but to prevent the Stodola iteration converging to the first flapwise mode again, a portion has to be subtracted (that proportional to the first flapwise mode multiplied by constant k) at each iteration according to .

3.14

$$u_{z'}^{1e} = u_{z'} - k.u_{z'}^{1f}$$
$$u_{y'}^{1e} = u_{y'} - k.u_{y'}^{1f}$$

where,

$u_{z',y'}$ is the deflection calculated each iteration according to 3.13 for a given constant loading.

The constant k is determined from the orthogonality principle as stated in Eq. 3.12, where here we make use of the fact that the natural frequencies of the flapwise and edgewise vibrations are not equal (they have their own distinct frequency and mode shape), thereby according to Eq.3.12, resulting in:

3.15

$$\int_0^R u_{z'}^{1f} m u_{z'}^{1e} dX + \int_0^R u_{y'}^{1f} m u_{y'}^{1e} dX = 0$$

Eq. 3.15 requires the integral over the entire blade, denoted by the integral over *R*.

Combining Eq. 3.14 and 3.15, the constant becomes defined as:

3.16

$$k = \frac{\int_0^R u_{z'}^{1f} m_i u_{z'} dX + \int_0^R u_{y'}^{1f} m_i u_{y'} dX}{\int_0^R u_{z'}^{1f} m_i u_{z'}^{1f} dX + \int_0^R u_{y'}^{1f} m_i u_{y'}^{1f} dX}$$

The inclusion of this into the Stodola procedure can now converge on the edgewise eigenmode. Similar statements are also made to find the 2nd flapwise mode of which is given completely in Appendix A.III.

1st Torsion Eigenmode

An approximate method to find the first pure torsion mode makes use of a similar iteration procedure based on convergence to the required mode. The procedure followed was obtained from [30]. This coupling of torsion to in-plane and out of plane motion is considered in the transformation equations in Appendix A.IV.

An initial mode is guessed and the local moments due to rotational inertias (including the effect of mass offset from shear centre) are integrated to give the total moment as a function of spanwise length (X). The local moments are given by:

3.17

$$M_t(x') = \varphi_t^i \left[J(x') + m(x') \left\{ r_{cog} - r_{shc} \right\}^2 \right]$$

where,

φ_t^i is defined as the torsion eigenmode at respective iteration step [rad]

J is the pitching moment of inertia of the blade [kgm^2]

$\left\{ r_{cog} - r_{shc} \right\}$ is the distance of the section centre of gravity from the shear centre [m]

The curvature (k_t) can then be defined by, and using the torsional rigidity of the blade (GJ [Nm^2] for thin walled aerofoil geometry) as:

3.18

$$k_t(X) = \frac{M(X)}{GJ(X)}$$

Like previously, the curvature is numerically integrated to arrive at a new deflection, which is used in the next iteration to determine local moments, and so on, until the torsion mode has converged. A complete account of the procedure is detailed in Appendix A.III.

Figure 3.9 to Figure 3.12 show the computed eigenmodes used in simulations for each DOF and their corresponding eigenfrequency is listed in Table 3.2.

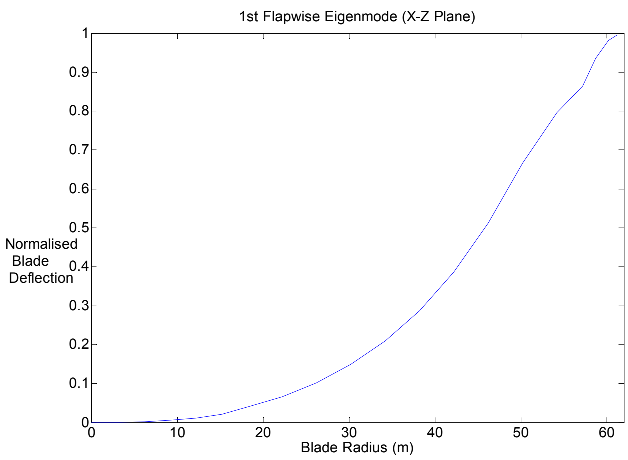

Figure 3.9 Blade Eigenmode for the 1st Flapwise DOF

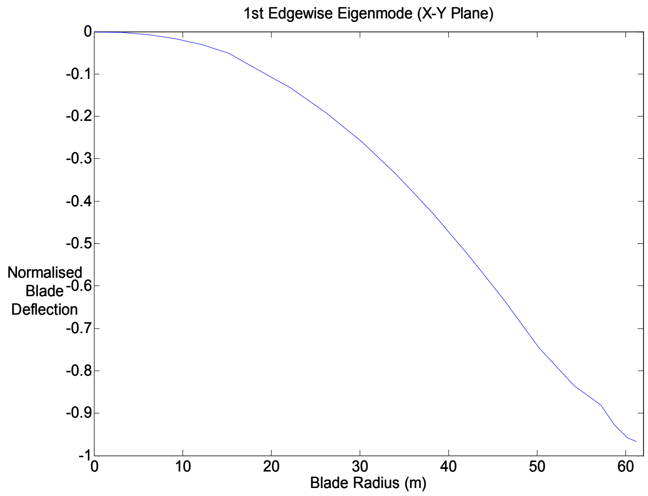

Figure 3.10 Blade Eigenmodes for the 1st Edgewise DOF

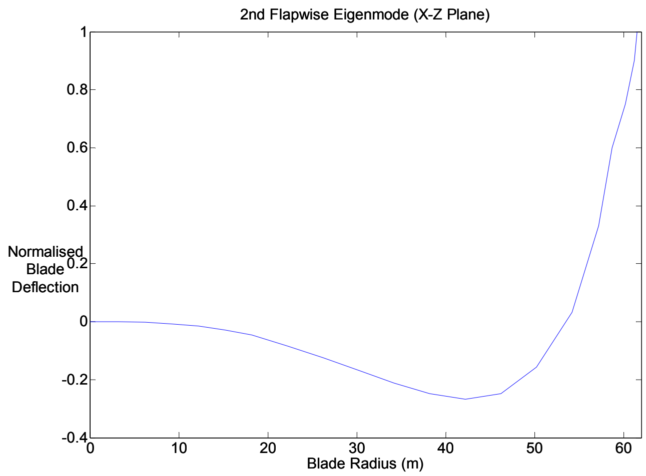

Figure 3.11 Blade Eigenmodes for the 2nd Flapwise DOF

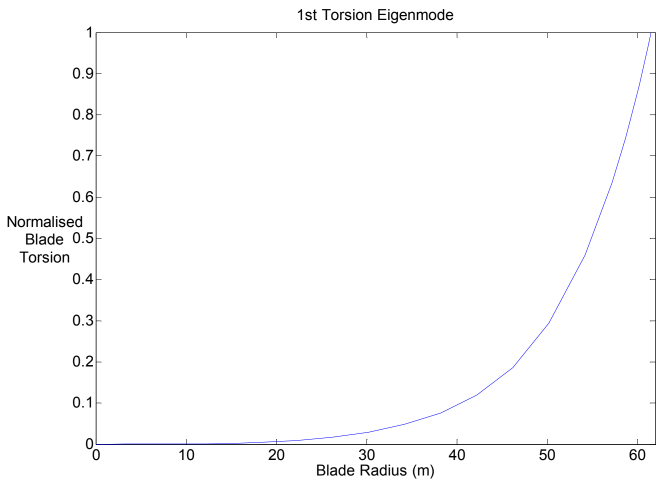

Figure 3.12 Blade Eigenmodes of 1st Torsion

Table 3.2 Blade Eigenfrequencies of the UPWIND Turbine

Blade Eigenmode	Eigenfrequency (Hz)
1st Flapwise	0.85
2nd Flapwise	2.20
1st Edgewise	1.20
1st Torsion	5.60

For each eigenmode, the slopes and curvatures are recorded and used in the calculation of generalised mass and force expressions given in the following section. The details of each eigenmode is given in Appendix A.III.

According to the generalised coordinate approach used in this study, the above eigenmodes (represented by Eq. 3.20) are used to estimate the blade deflections by solving the dynamic equations for the generalised coordinate q_g according to Eq. 3.19 [15].

3.19

$$v(x') = q_g(t).\varsigma(x')$$

where,

q_g is the generalised coordinate vector determining the contribution to the deflection from each eigenmode in time [m]

ζ is the corresponding normalised mode shape vectors for the DOF defined in Table 3.2 [-]

c as specified in Table 3.2 [m]

3.20

$$v(x') = \begin{bmatrix} u'^{1f}_i(x') \\ u'^{2f}_i(x') \\ u'^{1e}_i(x') \\ u^{1T}_i(x') \end{bmatrix}$$

where,

u'^{1f}_i, u'^{2f}_i, u'^{1e}_i and u^{1T}_i correspond to the blade nodal displacements from the contributions of the 1st & 2nd flapwise, 1st edgewise and 1st torsion modes respectively in the rotating blade axes.

The following section is dedicated to detailing the modal theory concept with generalised coordinates and required derived quantities for an effective dynamic model to determine the deflections as given by Eq. 3.20. A convenient starting point is the derivation of dynamic equations for the one bladed model used in the present study.

3.1.4.2 Rotor Blade Dynamic Equations

As in all dynamic systems, the equations of motion take the form (neglecting structural damping in this case) of:

3.21

$$\left[M\right]\ddot{v}+\left[K\right]v=\left[F_{ext}(t)\right]$$

where,

$\left[M\right]$ is the mass matrix

$\left[K\right]$ is the stiffness matrix

$\left[F_{ext}(t)\right]$ are the external forces as a function of time

It has already been stated the modal approach is used and by the orthogonality principle, we can arrive at a reduced DOF problem represented by Eq. 3.21. The introduction of the generalised coordinate allows the following generalised displacements to be defined in the blade principle axes;

3.22

$$z'=\sum_i u_{z'}^i(x').q_{z'}^i(t)$$

$$y'=\sum_i u_{y'}^i(x').q_{y'}^i(t)$$

$$\varphi=\sum_i u_{\varphi}^i(x').q_{\varphi}(t)$$

where,

$q_{z'}(t)$ is the generalised coordinate for flapping motion; for i =*1, 2*

$q_{y'}(t)$ is the generalised coordinate for in-plane motion; for i =*1*

$q_{\varphi}(t)$ is the generalised coordinate for elastic torsion motion; for i =*1*

i denotes the mode shape number, e.g. $u_{z'}^2$ would be the 2nd flap mode shape

With this coordinate transformation, Eq. 3.21 can equivalently be expressed as

3.23

$$\left[M'\right]\ddot{q}_g+\left[K'\right]q_g=\left[F'_{ext}(t)\right]$$

$$q_g=\begin{bmatrix} q_{z'}^i \\ q_{y'}^i \\ q_{\varphi}^i \end{bmatrix}$$

where v has now been replaced by the generalised coordinate, and the mass, stiffness and force matrices are now denoted as the generalised mass, stiffness and force corresponding to the generalised coordinate [4].

The generalised mass and stiffness matrix are a result of reducing the DOF by using mode shapes, which idealise the blade deflection with discrete points of mass joined together with an associated stiffness. Therefore, these matrices must describe the force equilibrium existing between the discrete points (equilibrium of internal elastic forces of the structure [4]) which define the mode shape as dictated by the external forces and inertial accelerations.

Trying to equilibrate the dynamic and internal elastic forces of the discretised blade system can be complicated, but a usual method is to use the principle of virtual work for determining the generalised forces and principle of virtual displacements (for a unit deflection of generalised coordinate) for determining the properties of the generalised mass (GM) and stiffness (GK) matrix [4]. In this way, the dynamic equation of 3.23 expressed in generalised coordinates and mode shapes of the blade can be evaluated using a suitable numerical time-stepping scheme. It should be noted that for this simplified study with one rotor blade attached to a rigid hub, structural damping has not been included.

The time-integration scheme used in this analysis is the Runge-Kutta-Nystrom method, of which is described in Appendix V. The essential characteristics of this scheme are that knowing the accelerations, velocities and positions at one time-step, the velocities and positions at the next time-step can be estimated. Accelerations and forces in this time-step can then be updated and a new time-step performed. For example, the acceleration at time *t=n,* for known positions and velocities at *t=n,* is given by Eq. 3.19 rewritten as,

3.24

$$\ddot{q}_g^n = \frac{1}{\left[M'\right]}\left\{\left[F''_{ext}(t)\right] - \left[K'\right]q^n{}_g\right\}$$

The solutions for each time-step yield scalar values of the generalised coordinates (q_g^n) for the corresponding DOF, which gives the amplitude of each vibration mode at that time-step. For the blade considered here, it is assumed the deflection can be considered as a linear combination of these modes [10], or rather, as given by an extension of Eq. 3.22:

3.25

$$z'(x') = u_{z'}^{1f}(x').q_{1f'}^n(t) + u_{z'}^{2f}(x').q_{2f}^n(t)$$

3.26

$$y'(x') = u_{y'}^{1e}(x').q_{1e}^n(t)$$

3.27

$$\varphi(x') = u_{\varphi}^{1T}.q_{1T}^n(t)$$

where,

$q_{1f,1e,2f,1T}$ are the solutions for generalised coordinates for the 1st flap, 1st edge, 2nd flap and 1st torsion mode respectively at a given time-step n ; and

u_j^i denotes the corresponding mode shape number and vector.

These uncoupled deflections are given in the principle axes coordinate system as per Figure 3.3. They are coupled and transformed to the rotating blade system according to the procedure of Appendix I.V.

In the coming sections, an account of formulating the Generalised Mass, Stiffness and Force (GM), (GK) and (GF) matrices is now given.

3.1.4.3 Generalised Force Matrix Formulation

The generalised matrices of the dynamic equation of Eq. 3.23 are defined such that the principle of virtual work can be used to describe the equilibrium state of the discretised structure under inertial and point loads. Once these matrices are defined according to the DOF of the system, the blade deflections may be simulated using point loading along the blade as determined by the aerodynamic model.

The generalised forces of the system are computed using the principle of virtual work performed by the external force distribution and deflection in the structure. For a modal analysis, the virtual work is considered to be that from which a given force distribution produces a unit deflection as described by each eigenmode of the system DOF, or, (in other words),

3.28

$$GF_i = W_i = \int_0^R P(x')u_i(x')dx'$$

where,

W_i represents the virtual work for a unit displacement in a corresponding DOF at each node [Nm]

P is the force distribution over the blade radius (edgewise & flapwise plane) [N/m]

u_i are the blade eigenmodes deflection at each node, corresponding to the DOF specified in Eq. 3.20 [-]

The integral is required over the blade length to represent the total virtual work. The load distribution and eigenmodes are defined at discrete points according to Figure 3.7, therefore to evaluate the integrand (area under force-displacement graph), while considering the blade deflection to have varying rotation (slope) and curvature, the following relation is implemented [11],

3.29

$$dW_i = P_i(\frac{7}{20}u_i + \frac{1}{20}s_i\Delta x' + \frac{3}{20}u_{i+1} - \frac{1}{30}s_{i+1}\Delta x')\Delta x' \ldots$$

$$\ldots\ldots\ldots\ldots\ldots + P_{i+1}(\frac{3}{20}u_i + \frac{1}{30}s_i\Delta x' + \frac{7}{20}u_{i+1} - \frac{1}{20}s_{i+1}\Delta x')\Delta x'$$

where,

P_i is the local force in the X-Z or X-Y plane at respective blade station along the radius [N/m]

u_i is the unit displacement of given DOF eigenmode at respective blade station [m]

s_i is the slope (tangent of displacement) at the respective blade station [-]

$\Delta x'$ is the distance between discretised segments as determined by choice of number of segments for the blade [m]

It can be seen this formulation uses the deformation around a local point to take into account the elastic bending of the beam (as opposed to rigid bending). Eq. 3.29 describes the situation for when curvature of the blade is considered to vary linearly between the points ($\Delta x'$). The slope and curvatures of the blade deflections are found from the blade eigenmodes as discussed in diction 3.1.4.1.

The generalised force for each DOF is thus obtained through summation of all the blade sections (dW_i). The generalised force matrix used in the current model is given in Eq. 3.35.

For the torsion DOF, Eq. 3.29 may be replaced by the following formulation that is more suitable for the exhibited shape of the eigenmode, by replacing the dynamic forces with the moments. The second moment term visible in Eq. 3.30 is the contribution of work given by the lift force acting over a moment arm due to the offset of the aerodynamic centre to the shear centre.

3.30

$$dW_i = (M_i^{\varphi} + M_i^{L})(\frac{1}{2}u_i^{1\varphi}.\Delta x' + \frac{1}{8}s_i(\Delta x')^2 + \frac{1}{24}s_{i+1}(\Delta x')^2)....$$
$$...........+(M_{i+1} + M_{i+1}^{L})(\frac{1}{2}u_{i+1}^{1\varphi}.\Delta x' + \frac{5}{24}s_i(\Delta x')^2 + \frac{1}{8}s_{i+1}(\Delta x')^2)$$

where,

M_i^{φ} is the aerodynamic moment at the respective blade station [Nm];

M_i^{L} is the moment caused by lift force at aerodynamic centre about the shear centre; and

All other variables as previously defined,

Again, Eq. 3.30 assumes a linearly varying curvature between the blade segments.

Centrifugal Stiffening & Rotational Inertia Loads

The generalised forces considered thus far govern the majority of the structural inertia effects as observed and reacted upon by the rotor blade. There are however other inertias involved due to the rotation of the rotor (and therefore mass) which has its own effect on the blade dynamics and which is not included in the generalised mass or force matrix using the above relations. This is termed a rotational inertia load. This can be accounted for in the equations of motion by considering it as a force on the right hand side of Eq. 3.23. The force is a centrifugal force which acts in the radial direction of the blade due to its angular velocity, and for a blade in elastic bending (deformed elastic axis), a component of this centrifugal force lies normal to the elastic axis (see F_C in Figure 3.13), providing a counterforce to that of the aerodynamic thrust force (and therefore reducing the amount of flapwise deflection).

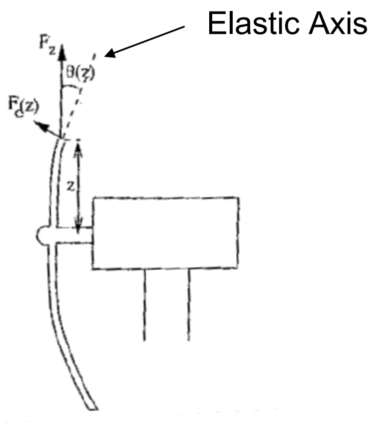

Figure 3.13 Component of Centrifugal Force Normal (F_C) to the Elastic Axis for Blade Bending

This component of centrifugal force can then be subtracted from the lift force (P_i) at each section of blade. The component of centrifugal force normal to the elastic axis experienced by each blade section is given in Eq. 3.31 [15].

3.31

$$F_{c_i} = -m_i\vec{\Omega}\times(\vec{\Omega}\times\vec{r})\sin\beta$$

where,

F_{c_i} is the component of centrifugal force normal to the elastic axis at a given node [N/m]

$\vec{\Omega}$ is the rotational vector of the rotor [rad/s]

$\vec{r}$ is the local radial vector in time of a point on the blade from the origin of the rotating coordinate system [m]

β is the local flapping angle (angle between un-deflected blade axis and elastic axis) [Deg]

The minus sign signifies the operation of moving the inertia force from the left hand side of the dynamic equations to the right side, i.e. the inertia acts as resistance as is subtracted from the external forces.

The position vectors for the blade sections are calculated from the solution to the equations of motion at the given time-step, and then used to determine the centrifugal effects for the following time-step.

Once this force is equated with the aerodynamic force of Eq. 3.29 (i.e. subtracted from), it now represents the generalised force including the effects of rotational inertia.

One other important effect included in the dynamic model is that of centrifugal stiffening of the rotor blade, which has the property of making the blade more resistant to bending. This effect is caused from the axial force in the blade due mainly to centrifugal and gravity effects [11]. It represents the work done by the axial forces to keep the blade at a constant length when it is undergoing a deflection. Therefore, this work should be included in the generalised force matrix. It was included in the dynamic model according to a procedure given by Hansen [11], whereby equivalent loads in the flap and edgewise deflections can be specified in terms of the axial force and blade slopes and curvatures, which gives the same bending moment and shear force distribution in the blade as the axial force would. These equivalent loads can be added to the generalised forces in the same manner as for the component of centrifugal force and are of the form:

3.32

$$P_{eq,z'} = F_{x'}u_{z'} - P_{x'}s_{z'}$$
$$P_{eq,y}' = F_{x'}u_{y'} - P_{x'}s_{y'}$$

where,

$P_{eq,z}$ is the equivalent force in the X-Z plane [N/m]

$F_{x'}$ is the total axial force in the blade [N]

$u_{z',y'}$ is the blade curvature in the X-Z plane [m^{-1}]

$P_{x'}$ is the axial force at each blade section [N/m]

$s_{z',y'}$ is the slope of the deflected blade [-]

The axial force includes the effects from centrifugal forces as well as the axial component of the cyclic gravity force.

Gravity

The loading in the edgewise direction due to gravity can be accounted for in a similar manner to the above, i.e. by adding the contribution of the gravity force at each node to the generalised force matrix. The force of gravity will take the form of a positive contribution to work done (added to the rotor torque) when the rotor blade is moving in the direction of gravity (right half of the rotor plane for clockwise rotating wind turbine), and negative when moving against it. The component of gravity for each blade section in the blade edgewise direction is given according to the following transformation (zero azimuth (ψ) defined when blade in the six o'clock position (blade down) meaning total gravity force starts in blade radial direction)

3.33

$$\begin{bmatrix} F_{gX} \\ F_{gY} \\ F_{gZ} \end{bmatrix} = \begin{bmatrix} \cos(\psi) & \sin(\psi) & 0 \\ -\sin(\psi) & \cos(\psi) & 0 \\ 1 & 0 & 1 \end{bmatrix} \begin{bmatrix} F_{gX,NR} \\ F_{gY,NR} \\ F_{gZ,NR} \end{bmatrix}$$

$$\begin{bmatrix} F_{gX,NR} \\ F_{gY,NR} \\ F_{gZ,NR} \end{bmatrix} = \begin{bmatrix} 9.8.m_{i.} \\ 0 \\ 0 \end{bmatrix}$$

where,

$F_{gX,Y,Z}$ is the force of gravity in the rotating blade system for axial and edgewise directions [N/m]

$F_{gX,NR}$ is the non rotating coordinate system specifying the initialised gravity force (blade down) [N/m]

$m_{i.}$ is the mass at the given blade section [kg/m]

In summary, the contributions of these other inertial and external influences are added to the respective out-of and in-plane aerodynamic forces, and with reference to Eq. 3.29:

3.34

$$P_{z'i} = L_{z'i} - F_{cz'i} - P_{eq,z',i}$$
$$P_{y'i} = L_{y'i} - F_{cy'i} - P_{eq,y',i} - F_{g,i}$$

where,

$L_{Z,Y,i}$ are the aerodynamic forces as determined from BEM theory [N/m]

The virtual work with all these effects is now accounted for, and ready to be solved with the corresponding generalised mass and stiffness matrices. The generalised force vector used for calculating the total work (including all the above effects) as defined in Eq. 3.23 in its entirety is given in Eq. 3.35.

3.35

$$GF_{q_{z'}^{1f}} = \int_0^R P_{z'}(x')u_{z'}^{1f}(x')dx'$$

$$GF_{q_{z'}^{2f}} = \int_0^R P_{z'}(x')u_{z'}^{2f}(x')dx'$$

$$GF_{q_{y'}^{1e}} = \int_0^R P_{y'}(x')u_{y'}^{1e}(x')dx'$$

$$GF_{q_{\varphi}^{1T}} = \int_0^R (M_{ac}(x') + M^L(x'))u_{\varphi}^{1T}(x')dx'$$

3.1.4.4 Generalised Mass Matrix

The mass matrix can be can be determined (column by column) by assuming a unit of acceleration of generalised coordinate ($\ddot{q}_g = 1$) of each DOF in turn, whilst keeping the acceleration of other DOF at zero. This gives inertial loads on the other DOF in the system (if there are components of inertia force in the respective directions), which can be represented by the generalised force as in Eq.3.28. Looking at it another way, the generalised mass can be found by replacing P in Eq. 3.28 with the inertial load given by a unit acceleration of the DOF of concern; for example, calculating the 1st column assumes a unit acceleration of generalised coordinate $\ddot{q}_{1f} = 1$ of the 1st flapwise DOF $u_{z'}^{1f}$ so that the inertial load, $P_{z'}$, is defined in terms of generalised coordinate:

$$P_{z'}(x') = m(x')\ddot{z}'(x')$$

$$\ddot{z}'(x') = \ddot{q}_{1f} u_{z'}^{1f}(x')$$

and for $\ddot{q}_{1f} = 1$

$$P_Z = m(x')u_{z'}^{1f}(x')$$

Therefore, representing the jth column as the generalised force vector of Eq. 3.28 and using the above inertia load, the 1st column and row ($GM_{1,1}$) of the generalised mass matrix takes the form of:

3.36

$$GM_{1,1} = \int_0^R m(x')u_{z'}^{1f}(x')u_{z'}^{1f}(x')dx'$$

This procedure for the generalised mass merely relates the inertial loads at discrete points of the system in terms of the generalised coordinate and represents the inertial characteristics of the structure for a given excitation. It could also been seen as the structures resistance to accelerations.

Row 2 of the 1st column is again found using the generalised force of Eq 3.28, but this time with a unit deflection in DOF number 2, say the edgewise eigenmode, $u_{y'}^{1e}$, while still using the inertial load due to acceleration in flapwise DOF $u_{z'}^{1f}$ (since we are still in column one of the GM matrix). This gives:

3.37

$$GM_{1,2} = \int_0^R m(x')u_{z'}^{1f}(x')u_{z'}^{1e}(x')dx'$$

This brings us back to the convenience of using a modal approach, whereby Eq. 3.37 must satisfy the orthogonality principle given by Eq. 3.12. It is shown in Table 3.2 that the flapwise and edgewise eigenfrequencies are not the same, therefore the product of Eq. 3.37 must be zero; hence $GM_{1,2} = 0$. This shows how the modal method produces uncoupled equations of motion of the left side of the dynamic equation.

This procedure is done for unit accelerations in each DOF (each column) until the mass matrix is filled. The resulting generalised mass matrix for the one bladed system considered here is given in Eq. 3.38.

Definition and Inclusion of Torsion Parameters

The following is just an example to highlight the important parameters involved with a body in torsion and the equations given are not the equations used in the generalised equations of motion. The equations represent a 2-D system of flap and torsion just to illustrate the forces and couplings we are considering in this study.

The entries for the torsion mass matrix coefficients make use of the location of the centre of gravity offset (y_{cg}) to the elastic axis as detailed in section 3.1.2.3 with regards to Figure 3.5. This serves as a mass coupling system (static mass moments) between the flap and torsion displacements. The pitching inertia about the shear centre (I_{φ}) is defined in the generalised mass matrix and is taken from the blade section structural data in Appendix A.II. The generalised mass matrix coefficient including this inertia term is contained equivalently as described in equations of motion for a 2-D case described below (the bracketed term), i.e. of the form of:

$$my_{cg}\ddot{z} + (I_{\varphi} + my_{cg}^2)\ddot{\varphi} + k_{\varphi}\varphi = P_z y_{ac} + M_{ac}$$

$$or,$$

$$my_{cg}\ddot{z} + m(\frac{I_{\varphi}}{m} + y_{cg}^2)\ddot{\varphi} + k\varphi = P_z y_{ac} + M_{ac}$$

$$where,$$

$$\frac{I_{\varphi}}{m} = K_{\varphi}^2$$

where K_{φ} is defined as the radius of gyration of a mass about the elastic axis (units of m) and the right hand side being the aerodynamic moment and contribution to the moment by the lift force, $P_{z'}$, acting at an offset to the elastic axis.

For the generalised equations of motion, coefficients of $\ddot{z}$, $\ddot{\varphi}$ (mass matrix) and φ (stiffness matrix) are generated for the full blade span with coupling for torsion and flapwise motion only. The coefficients for the stiffness matrix are given in section 3.1.4.5. It is considered the moment arm causing torsion that is generated from the centre of gravity offset in the direction normal to the flapping plane (i.e. in direction of blade thickness) is small, and thus edgewise-torsion coupling is neglected.

In the determination of the generalised mass matrix torsion coefficient, the sign of y_{cg} in the bracketed term above depends on where the centre of gravity lies for each section, thus being defined as positive if situated between the elastic axis (EA) and leading edge.

The overall generalised Mass Matrix Entries for the current case are given in Eq. 3.38 for a 4 by 4 matrix.

3.38

$$GM_{1,1} = \int_0^R m(x')u_{z'}^{1f}(x')u_{z'}^{1f}(x')dx'$$

$$GM_{1,4} = GM_{4,1} = \int_0^R m(x')y_{cg}u_{\varphi}^{1T}(x')u_{z'}^{1f}(x')dx'$$

$$GM_{2,2} = \int_0^R m(x')u_{z'}^{2f}(x')u_{z'}^{2f}(x')dx'$$

$$GM_{2,4} = GM_{2,4} = \int_0^R m(x')y_{cg}u_{\varphi}^{1T}(x')u_{z'}^{2f}(x')dx'$$

$$GM_{3,3} = \int_0^R m(x')u_{y'}^{1e}(x')u_{y'}^{1e}(x')dx'$$

$$GM_{4,4} = \int_0^R m(x')\left[\frac{I_{\varphi}}{m(x')} + y^2_{cg}\right]u_{\varphi}^{1T}(x')u_{\varphi}^{1T}(x')dx'$$

All other generalised mass matrix entries are equal to zero.

3.1.4.5 Generalised Stiffness Matrix

The generalised stiffness matrix is generated in a similar fashion to the mass matrix, but rather than assuming accelerations in each DOG freedom to determine inertias, here we determine the external forces which are required to produce a unit deflection in each DOF freedom and zero for all others and again specifying these loads as a generalised force. The idea of this procedure is to find the static equilibrium of the discrete structure from an instantaneous deflection caused by the generalised coordinates [11]. These forces can be specified in terms of Hooke's law (Eq. 3.39), relating the forces in the structure being proportional to the spring stiffness (*K*) and amount of deflection in generalised coordinate.

3.39

$$F = Ku$$

An example here illustrates how each column of the stiffness matrix is constructed by examining the 1st two rows of the 1st column.

The set of loads required to produce a unit deflection in DOF $u_{z'}^{1f}$ are;

$F_z = K_z u_z^{1f} = K_z.1$

Therefore, the force required to maintain static equilibrium for the corresponding DOF is the summation of the external force at each node, leaving $F_{z'} = K_{z'}$. This can be expressed as the generalised force (virtual work) using Eq. 3.28 and making the substitution of $F_{z'}$ for $P_{z'}$ and generalised coordinate for displacement to arrive at a similar expression to that as above for the mass matrix:

3.40

$$GK_{1,1} = \left(\omega_{z'}^{1f}\right)^2 \left[\int_0^R m(x')u_{z'}^{1f}(x')u_{z'}^{1f}(x')dx'\right]$$

where $\omega_{z'}^{1f}$ is the eigenfrequency of the 1st flapwise eigenmode and has been defined from the flap stiffness according to:

3.41

$$\omega_{z'}^{1f} = \sqrt{\frac{K_{z'}(x')}{m(x')}}$$

$$and,$$

$$K_{z'} = \left(\omega_{z'}^{1f}\right)^2 m(x')$$

It can be seen Eq. 3.40 is just the mass matrix multiplied by the natural frequency of the corresponding mode. This makes sense in that the stiffness is trying to equilibrate the system from the inertial forces imposed by the external force.

The 2nd row of the stiffness matrix is determined as the forces induced in DOF 2, for example the edgewise mode ($u_{y'}^{1e}$), due to a unit deflection in $u_{z'}^{1f}$. However, due to orthogonality between the 1st flapwise and 1st edgewise mode, there are no induced deflections in the edgewise direction and therefore no work done. Therefore the generalised force is zero for this entry. A similar argument exists for the unit displacement of the 2nd flapwise mode.

The entire stiffness matrix coefficients for the current blade system are given in 3.45 and 3.46.

Representing Flap-Torsion Stiffness Coupling in Dynamic Equations

In addition to the formulation specified above for matrix stiffness coeficients, an additional external loading causing a torsion deflection, is a moment about the elastic axis (taken from the centre of gravity offset) caused by the curvature of the elastic axis introduced due to flapwise bending. This occurs due to the centrifugal force having a component perpendicular to the elastic axis with magnitude dependent on the rotation angle in flapwise bending (the slope of deflection, $(u_z^{1f})'$ and assuming small angle approximation - $\sin\theta \approx \theta = (u_z^{1f})' q_z^{1f}$) [1]. Because the centre of gravity is offset to the elastic shear centre, a moment is produced about this axis. This is illustrated in Figure 3.14.

[Source:Bielawa]

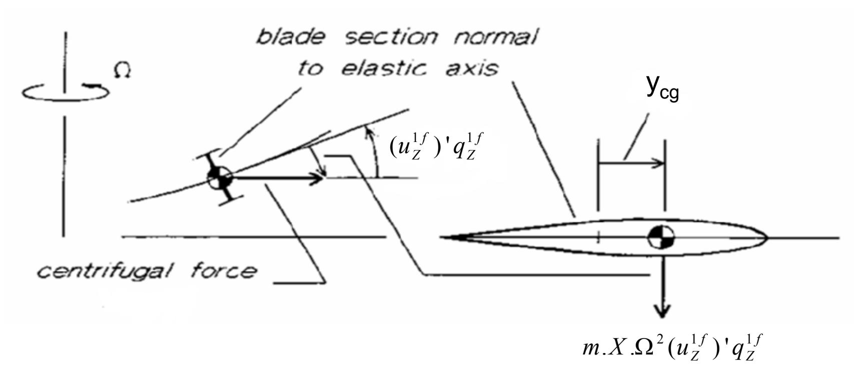

Figure 3.14 Torsion Moment Due to Flapwise Bending and Centrifugal Forces

In a similar manner, a moment is introduced over the spanwise direction due to a moment arm created by a torsional deflection which rotates the centre of mass out of the rotor plane (hence, providing a moment arm for centrifugal force to act over). From these descriptions, the stiffness coupling becomes evident; a blade in bending induces torsion about the elastic axis, which in turn causes a spanwise moment influencing flapwise bending.

This coupling is included in the equations of motion in the usual manner by specifying it as a generalised force. Referring to the first column of the stiffness matrix, wherein a unit deflection in the flapwise bending section is examined, the corresponding external force (moment) induced about the elastic axis is:

3.42

$$M_{EA} = m(x')\Omega^2 r(x')[u_z^{1f}(x')]' y_{cg}(x')$$

where,

$[u_z^{1f}]'$ is the slope at the blade section in bending and via small angle approximation, gives the component of centrifugal force normal to the elastic axis

To include this external loading in the dynamic model here, it must be represented as the generalised force (moment) according to Eq. 3.28 and use the principle of virtual work; i.e.

3.43

$$GK_{1,4} = \int_0^R M_{EA} u_\varphi^{1T} dx'$$

For the other stiffness matrix constituent, $GK_{5,1}$, a similar expression to 3.42 is obtained for a moment in flapwise direction determined by the moment arm created by the centre of gravity offset and a given unit of rotation and using small angle approximation ($y_{cg} u_\varphi^{1T}$). The moment is thus defined as:

3.44

$$M_{flap} = m(x')\Omega^2 r(x') u_\varphi^{1T} y_{cg}(x')$$

The loading produced along the span is given by the spanwise derivative of this moment, which is given by multiplying 3.44 by the slope in flapwise bending $[u_z^{1f}]'$. Converting this to the generalised force through the virtual work principle, it can be shown the matrix entries for coupled flap torsion become:

3.45

$$GK_{1,4} = \int_0^R \left\{ m(x).\Omega^2.r.y_{cg}.\left[u_z^{1f}(x)'\right]\right\}.u_\varphi^{1T} dx'$$

$$GK_{4,1} = \int_0^R \left\{ m(x).\Omega^2.r.y_{cg} u_\varphi^{1T}(x).\left[u_z^{1f}(x)'\right]\right\}.u_z^{1f} dx'$$

It is worth noting these differ from other stiffness matrix entries which are formulated using the relative spring stiffness (leading to expressions for natural frequencies) to determine the generalised forces when a DOF is excited. The stiffness matrix just needs to include all external forces (stated as generalised vector) so that the static equilibrium can be determined.

The remaining stiffness matrix coefficients are given in Eq. 3.46.

3.46

$$GK_{1,1} = (\omega_{z'}^{1f})^2 \left[\int_0^R m(x') u_{z'}^{1f}(x') u_{z'}^{1f}(x') dx' \right]$$

$$GK_{2,2} = (\omega_{z'}^{2f})^2 \left[\int_0^R m(x') u_{z'}^{2f}(x') u_{z'}^{2f}(x') dx' \right]$$

$$GK_{3,3} = (\omega_{y'}^{1e})^2 \left[\int_0^R m(x') u_{y'}^{1e}(x') u_{y'}^{1e}(x') dx' \right]$$

$$GK_{4,4} = (\omega_{\varphi}^{1T})^2 \left[\int_0^R m(x') \left[\frac{I_{\varphi}}{m(x')} + y^2{}_{10_{cg}} \right] u_{\varphi}^{1T}(x') u_{\varphi}^{1T}(x') dx' \right]$$

Up to now, the formulation of the dynamic equations of a single blade with four degrees of freedom, neglecting damping, has been given.

Now, an overview of the WIMSIM simulation modelling environment is given to clarify the Aeroelastic model set-up.

3.1.5 Simulation Environment

The WIMSIM model uses the Matlab Simulink graphical interface for the representation of the aeroelastic model in this study. The model contains 3 modules:

1. Wind Generating Module
    a. Wind Shear
    b. Tower Shadow
    c. Turbulence
2. Aerodynamics Module
    a. BEM Theory
    b. Lift coefficient determined via Theodorsen's theory and for trailing edge geometry
    c. Trailing Edge Flap controller inputs (positions, velocities & accelerations)
3. Structural (Rotor Dynamics) Module
    a. Modal analysis

A fourth module will be added later, namely the trailing edge flap controller with added feedback. The details of this are given in section 5.

A diagram of the basic aeroelastic model is given in Figure 3.15. Behind each module lies the theory and parameters as discussed in the previous sections. It should be noted the simulations carried out in this investigation used a steady mean wind speed only with some simulations including tower shadow and wind shear. No effect using turbulence was carried out, but this would be useful for future investigations.

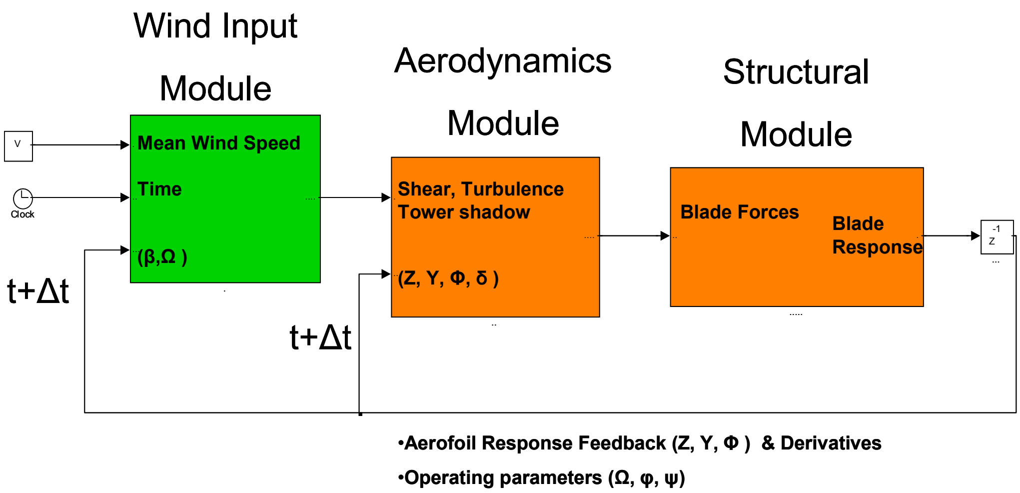

Figure 3.15 Basic Representation of the WIMSIM Aeroelastic Model

The model is intialised with operating parameters according to the given mean wind speed. There is no control system installed for pitching or generator speed, as simulations are run at constant settings specified by the wind turbine operating characteristics, of which are given in Appendix A.II.

The blade response determined at time (t) is fed back into the aerodynamic module in the next time-step to assess the new blade inflow conditions. The wind input module also requires some feedback data for generating wind shear and tower shadow effects at the rotor. For the intention of investigating trailing edge flap control, a controller module would be inserted in the above figure, taking an input from most probably a measured blade response variable (e.g. blade acceleration), and giving an output of trailing edge flap deflection, velocity and acceleration for input into the aerodynamic model. This is given further attention in section 5.

3.2 Classical Flutter - Stability Limit Determination

The instability of Classical Flutter was introduced in a qualitative sense in section 2, and a dynamic model was described with various included couplings in section 3.1.4. The aeroelastic model should now be set up to capture the "Classical Flutter" phenomenon for given characteristics and operating conditions of a wind turbine. As a reminder to the reader, the primary goal of this study is to investigate the effects on the Flutter stability limit using a trailing edge control surface. This therefore requires the stability limits to first be identified so that it is known in which operating conditions (e.g. wind speed, rotor angular velocity) the turbine is running at such that there is instability to control. Determination of the Flutter stability limit also offers insights into the stability margin of some of the bigger wind turbines already in commercial development today, while providing a basis to perhaps estimate if Flutter is a 'near future' problem for designers. The stability limit at given operational parameters is most often measured as a function of dynamic pressure, from which can be related to tip speeds of the blade and hence, the rotor angular velocity at the Flutter limit. This is examined further in the following section.

The UpWind blades used here are obviously not expected to be within the Flutter boundaries for its normal operational conditions (tip speeds), but the idea here is to induce the blade to a Flutter condition by altering the operating conditions or by modifying the blade to a lower torsional stiffness (lower natural frequency). The location of the centre of mass behind the elastic axis is also a parameter that can be used to drive the blade to a lower Flutter stability margin for reasons stated in previous sections.

There are a range of methods available to determine the stability limit based on the dynamic equations, some more elegant than others. The most common approach appears to be through a linearisation of the equations of motion about an equilibrium point and then using the eigenvalue problem to solve for the amplitudes and phases of the system, which give information as to the stability of the system at the specified operating conditions [5].

Another, somewhat less elegant approach, is to identify the Flutter boundary by forcing Flutter to occur by adding a harmonic excitation force over a specified frequency range to the generalised forces and view the response of the system to discover where the two modes (flap and torsion) converge and hit an infinite solution (the Flutter point) [14]. This is shown in Figure 3.16. This is called the "Brute Force Method", which effectively performs a frequency sweep in the time-domain to determine the frequency at which instability occurs.

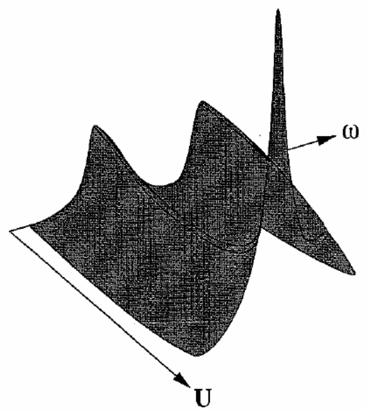

Figure 3.16 Working Principle of the Brute Force Method – Two Modes Converging to Point of Instability

This however requires multiple simulations over varying wind speeds and therefore is more time consuming to obtain the full Flutter boundaries. A full account of the Classical Flutter phenomenon is not in the scope of this study, but rather its control using trailing edges flaps. Therefore, the latter of the methods just mentioned is sufficient to determine some Flutter regions for some selected turbine configurations for the purposes of adding a control flap. The following outlines the frequency sweep implementation.

3.2.1 Brute Force Flutter Limit Determination Method

The method is rather simple to employ in the aeroelastic model because due to the nature of rotor dynamics having gravity effects as a function of its rotational frequency, a sinusoidal varying forcing function already exists in the dynamic equations to perform the frequency sweep of the system. The gravity force therefore acts an exciter for the Flutter mode, which at some frequency (for a given tip speed) will merge flap and torsion modes to cause the Flutter mode. The gravitational force can be swept over a frequency range by allowing the rotor angular velocity to gradually speed up, which has the following two effects in reference to Figure 3.17.

1. Rising angular velocity causes rising tangential velocity ($V_t=\Omega r$) and therefore increases the relative wind velocity (W) for a given wind velocity (V_p) into the rotor plane and hence, dynamic force
2. An excitation force due to gravity at a frequency proportional to the rotor angular velocity

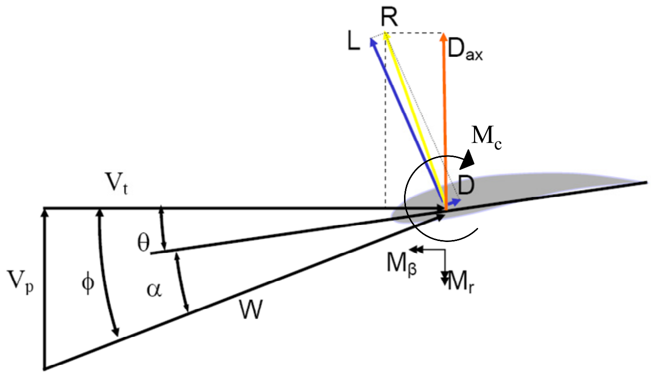

Figure 3.17 Section of an Aerofoil Highlighting Velocity Vectors Affected for Increasing Rotor Speed

At the rotor angular velocity where the Flutter limit is reached, the Flutter speed can be determined for that corresponding at the blade tip, i.e.

$$V_f = \Omega r_{tip} - \dot{Y} \qquad \textbf{3.47}$$

where,

V_f is the Flutter velocity

$\dot{Y}$ is the blade in-plane velocity

The ramp up rate of the rotor angular velocity is also specified such that quasi-steady state conditions of the aerodynamics at the rotor can be assumed. This merely suggests that enough time is given between increments to ensure continuity exist in the solution at each time step by allowing enough time for the flow conditions in the wake to reassert its effects back upstream.

The Flutter stability limits can now be assessed for some selected conditions of interest for this study.

3.2.2 Stability Limit Investigation Cases

The stability limits are investigated for three different cases, the first case being the Flutter limit for the current 5MW UpWind turbine using the actual blade properties. The second case uses a modified centre of gravity (COG) offset from the elastic axis (EA) (placed forward of towards the leading edge) to observe the effect on Flutter limit speeds and if this is in agreement with other studies. The third case involves scaling up the 5MW turbine to a 10MW design and comparing the difference in Flutter response. The cases are summarised in Table 3.3.

Each case is simulated with the specified parameters each indicated wind speed to find the Flutter limit at that wind speed for the given torsional stiffness.

It is also required to define a Flutter condition occurring in the operational range of the UpWind turbine so that Flutter suppression can be investigated using trailing edge flaps. This is the topic of section 5.

Table 3.3 Wind Turbine Flutter Stability Test Cases and Corresponding Blade Parameters

Case	Description	Torsion Eigenfrequency (Hz)	COG Offset Relative to EA (% of chord)	Undisturbed Wind Velocity (V) (ms^{-1})				
1	Original UpWind Turbine Specifications	5.6	~ -10	7	10	15	20	25
2	Case 2 but COG Forward of EA	5.6	~ +5	-	-	15	-	-
3	Modified Stiffness & COG Offset for 10MW Turbine	4.0	~ -12	7	10	15	20	25

The findings from these cases are given in sections 4.2 and 4.3.

In Section 4.1, the aeroelastic models performance is tested and validated against a study performed on the same wind turbine, after which a Flutter analysis is given.

4 Dynamic Model Validation & UpWind Turbine Flutter Limits

Most aerolelastic codes available today for wind turbine design technology do not consider the torsional degree of freedom in the computations, as the scale of today's modern turbine allow it to be sufficiently stiff in torsion so that it can be neglected in aeroelastic effects. Therefore, it is not easy to verify the elastic torsion response of the designed aeroelastic model in this study. There is some confidence in its certainty in that the approach to model torsion uses the same modelling principles as the flap and lead-lag blade motion, which can be verified using commercial aeroelastic codes by comparing turbine response for given wind conditions.

Section 4.1 is dedicated to demonstrate that the aeroelastic model used in this study is sufficient to simulate the response of a real wind turbine and in enough detail to capture the Classical Flutter phenomenon. The out-and-in-plane blade deflections including elastic torsion are validated against those computed by an ECN code called Blademode [29], of which an analysis was conducted on the same UpWind turbine, which has some slightly altered operating characteristics (e.g. pitch angle settings, rotor speeds and damping around rated speed).

Thereafter, in section 4.2 the main instability of Classical Flutter is investigated with determination of the Flutter limits for the UpWind turbine according to the cases given in Table 3.3.

The chapter concludes with examination of the Flutter stability limits for a 10MW wind turbine designed from scaling principles of the 5MW UpWind turbine, assuming design principles commonly used today. A comparison of the Flutter limits for current and future wind turbines is made.

4.1 WIMSIM Blade Deflection Predictions

The flap, edgewise and torsion blade deflections of the WIMSIM aeroelastic model were compared against those determined using the ECN Blademode aeroelastic program for steady wind conditions. The tip deflections were calculated over a selection of the wind velocity operating range of the wind turbine to indicate the accuracy of the model. The deflections are given in the rotating blade axes coordinate system in reference to Figure 3.3. The deflection comparison can be viewed in Figure 4.1, with the turbine operating characteristics given in Table 4.1.

Figure 4.1 indicates that the blade flapwise and edgewise deflections predicted in WIMSIM, which uses a simplified structural representation of the wind turbine (no tilt or rotor coning), predicts tip deflections to within good accuracy to the Blademode model, which has slightly differing wind turbine operating characteristics. The pre-coning and tilt angle not included in WIMSIM will reduce the effective area of the rotor, and hence thrust, which may explain the smaller deflections identified in the Blademode model around the rated speed region and for zero pitching. The biggest discrepancy occurs around the rated wind speed ($11ms^{-1}$), where a difference in thrust coefficient between the models was found (C_T WIMSIM: ~ 0.78, C_T Blademode: ~ 0.7). A slightly varying thrust coefficient is not surprising given the increased rotor area in the WIMSIM model.

Large loads are present on approaching the rated wind speed and the Blademode model makes some adjustments to reduce the loading, such as added modal damping to the dynamics at this wind speed. The WIMSIM model neglects added modal damping in the dynamics but adds small blade pitch on the onset of rated wind speed to reduce peak loads. This contributes to some of the uncertainty between the two models in such a scenario.

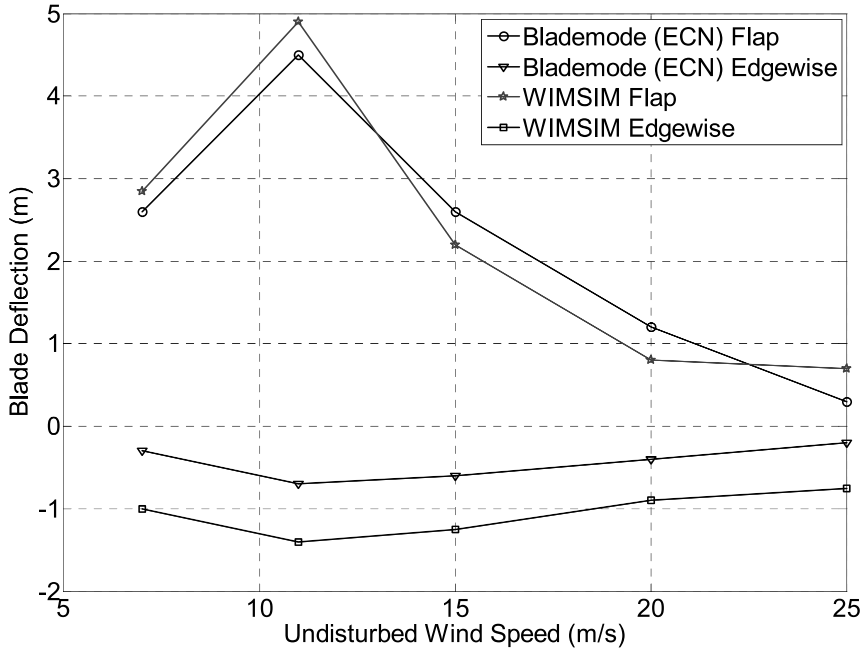

Figure 4.1 WIMSIM and BLADEMODE (ECN) Predicted Flapwise & Edgewise Tip Response for a Range of Wind Speeds

The in-plane deflections are over predicted by WIMSIM across the wind speed range but still to within a reasonable tolerance. A reason for this predicted error could be due to WIMSIM simulating a wind turbine with a rigid hub, thereby excluding any damping provided through the drive train (e.g. from the generator). The Blademode model simulates with drive train dynamics, which may explain the discrepancy between the exhibited responses.

The coupling between torsion and in-plane deflection also showed impacts in the shown edgewise vibrations, where for cases of centre of mass being forward of the elastic axis, torsion, flapwise and in-plane deflections showed reduced deflection. An example of the difference in edgewise deflection is shown in Figure 4.2.

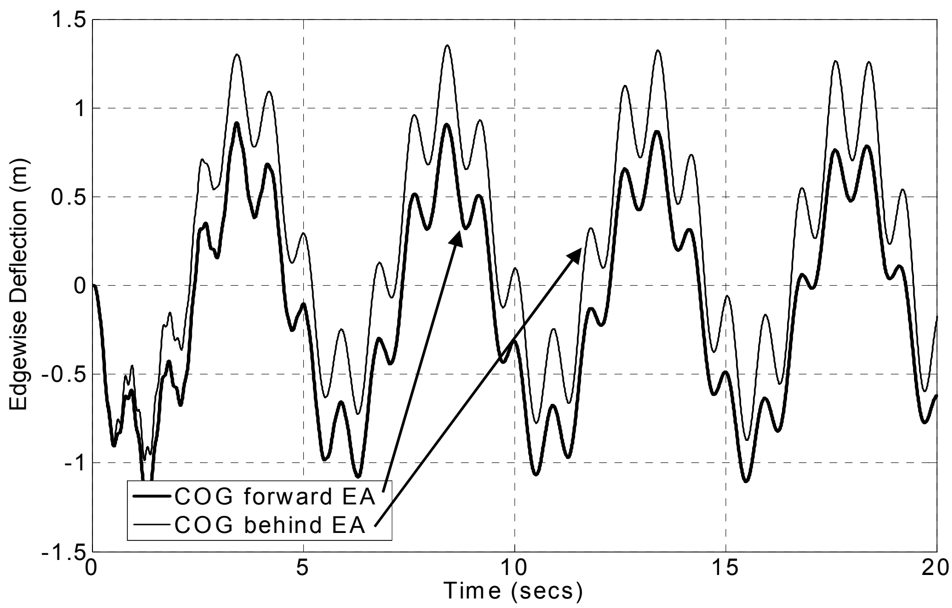

Figure 4.2 The Impact of Centre of Gravity Location of Edgewise Vibrations

With reference to Figure 4.2, the COG located in front of the elastic axis changes the mean position about which the oscillations occur and the maximum amplitude reduces from ~ 1.4m to ~ 1m in the edgewise direction.

Figure 4.3 shows the blade torsional response as predicted in the WIMSIM and Blademode simulations. The figure indicates increased positive torsion near the rated speed region and at lower wind speeds when the blade pitch is zero for the WIMSIM model compared to Blademode. The Blademode torsion response does not show positive deflection around the rated wind speed region, but rather shows the aerodynamic moment dominating across the wind speed range causing negative torsion. This may be because of a different structural model setup. For example, the WIMSIM model includes the moment obtained about the shear centre due to the lift force acting at an offset (moment arm) from the shear centre. For rated speeds and zero pitch angles, a greater moment about the shear centre results, pulling the blade nose up and indicated in Figure 4.3. When pitching of the blade occurs and higher wind speeds, the moment pulling the nose up due to lift acting at the aerodynamic centre is dramatically reduced and the negative aerodynamic moment about the shear centre dominates, pulling the nose down.

The location of the centre of gravity (COG) is also observed to impact the torsional response as it did with flap and edgewise motion. WIMSIM considers the offset of the COG location from the shear centre (see Figure 3.5), which gives different torsion dynamics whether it is placed forward or backward of this point. For the UpWind blade, the centre of gravity at its furthest point behind the shear centre along the span of the blade (COG position changes along the elastic axis with blade span) approaches approximately 0.7m, with the average over the blade being about 0.36m.

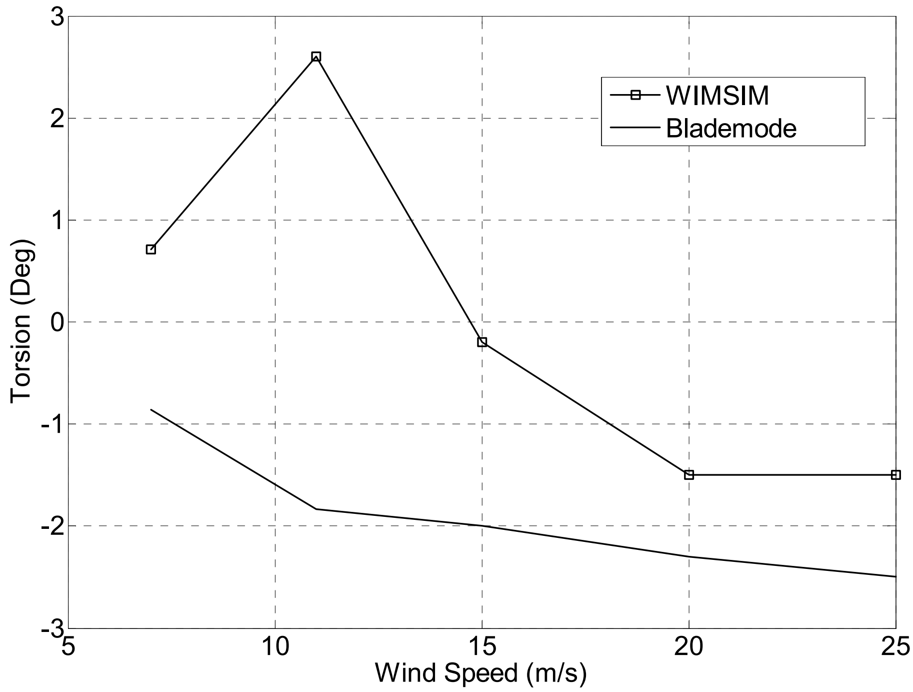

Figure 4.3 Comparison of WIMSIM and Blademode Torsion Tip Response

Table 4.1 Blade Tip Deflection Comparison with Blademode UpWind Turbine [29]

Wind Speed (ms^{-1})	RPM	Blade Pitch (Deg)	WIMSIM			Blademode (ECN)		
			Z (m)	Y (m)	Φ (deg)	Z (m)	Y (m)	Φ (deg)
7	8.0	0.0	2.85	1.00	0.71	2.60	0.30	-0.86
11 *(rated)*	11.5	3.0	4.90	1.40	2.60	4.50	0.70	-1.83
15	12.7	10.5	2.20	1.10	-0.20	2.60	0.60	-2.00
20	12.7	17.0	0.80	0.90	-1.50	1.20	0.40	-2.30
25	12.7	23.3	0.70	0.80	-1.50	0.30	0.20	-2.50

A typical simulation showing the governing response of the UpWind turbine in WIMSIM is illustrated in Figure 4.4. After the initial transients are overcome, the steady state values can be identified. The dominant effect of gravity in the edgewise plane is exhibited in the response of torsion and flap, which show a small oscillating component tuned to that of the edgewise deflections.

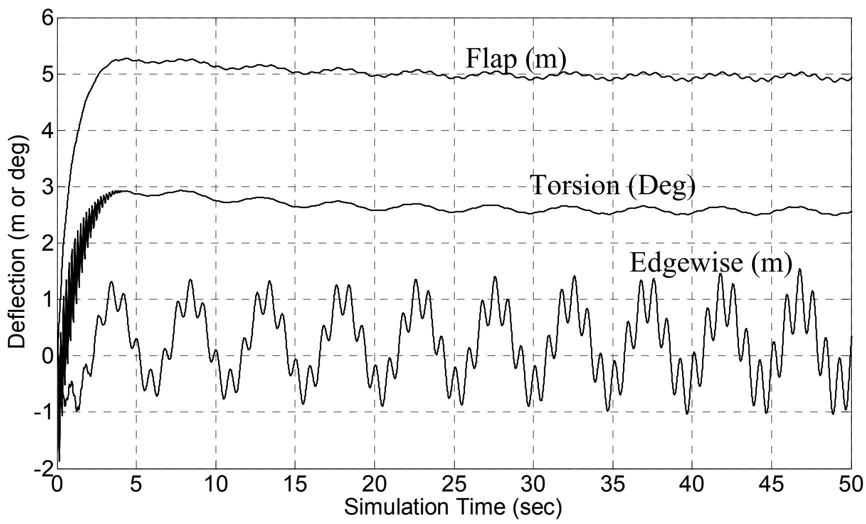

Figure 4.4 UpWind Blade Deflection at Rated Windspeed 11ms^{-1} and 12.7 RPM – Flap, Edgewise & Torsion

The preceding comparison seems to suggest the simplified model of WIMSIM configured to capture Classical Flutter effects produces a reasonable estimate of the response of the UpWind turbine. The flapwise and edgewise deflections show good agreement, with absence of structural damping possibly being a cause of larger edgewise deflections.

It is concluded here also that modelled torsion of a blade can take different forms depending on the configuration of blade parameter offsets generating moments, and also depending on the coupling between blade bending. It should be noted that the Blademode simulation represents a full wind turbine aeroelastic analysis, while WIMSIM uses a one bladed model attached to rigid hub. This means structural coupling effects will be quite different and some deviation in their response is expected.

4.2 Analysis of the Flutter Margins

The method of determining the Flutter boundaries of the UpWind turbine blade is given in section 3.2, along with the selected cases to be examined which define the Flutter behaviour according to certain operating and blade structural parameters. Figure 4.5 depicts the point at which the blade experiences "Classical Flutter" for the wind conditions specified and with the original UpWind turbine blade centre of gravity location and other relevant parameters as given in Appendix A.II. The figure represents the deflections in the flapwise and torsion directions as measured with an increasing blade tip speed as the rotor is allowed to gradually speed up in time. The point at which Flutter appears is where the torsion and flap modes (frequencies) have converged on each other as result of an increasing frequency (from increasing rotor speed) of the gravity forcing function at the corresponding dynamic force. Figure 4.6 illustrates the converging mode frequencies of the system for the specified case.

Torsion & Flap Deflection for V = 10ms^{-1}

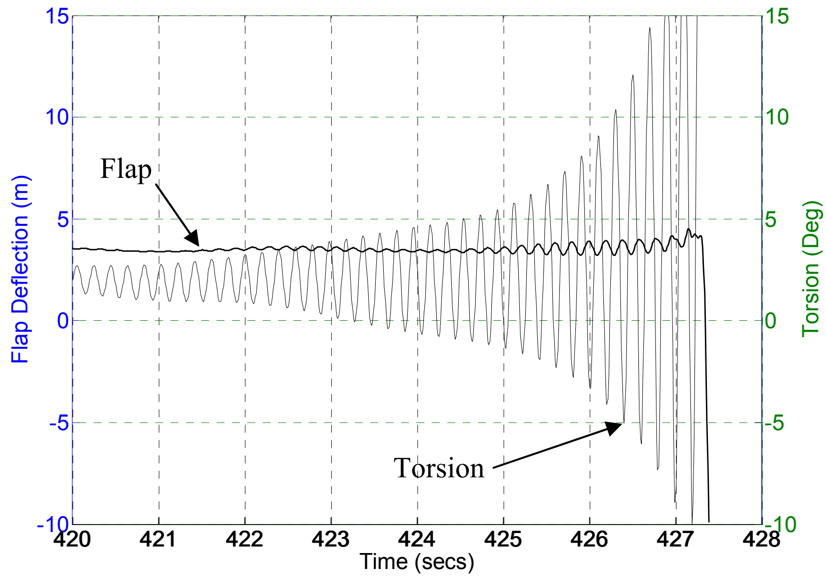

Flutter Rotor Speed (~ 19.5 RPM) for V = 10ms^{-1} (In-plane Tip Speed ~ 118ms^{-1})

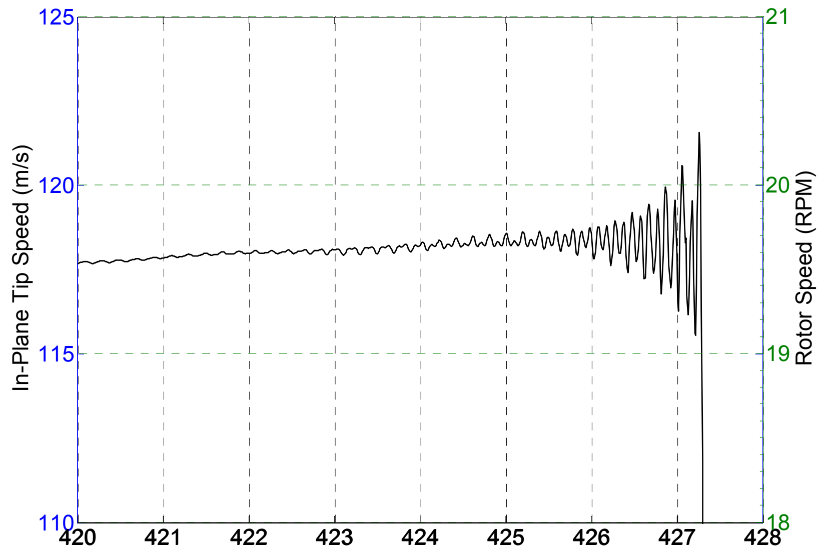

Figure 4.5 Exhibited Classical Flutter at Representative Wind Speeds of V = 10ms^{-1} for Increasing Rotor Speed (Flutter Tip Speed ~ 118ms^{-1})

Figure 4.5 (top figure) shows the point at which the instability starts to appear and at which tip speed (bottom figure). The tip speed has an oscillating value since in is measured in the edgewise plane. For convenience, the time history prior to that shown has been omitted, and only that given is where Flutter is evident. The distinguishing feature of Flutter, as can be viewed, is the increasing amplitudes of both torsion and flap to a point where in practical terms, failure of the blade would occur. It is shown the deflections go well beyond normal limits, and can occur within a range of seconds to tens-of-seconds. The Flutter speed for the case shown is defined at the point where the increasing amplitudes first become evident, which is seen to be approximately 118ms^{-1}.

The time simulations of Flutter are useful for viewing the blade response but no information about the blade modal interactions or system frequencies is available in this format. Therefore, the dynamics occurring near the Flutter point were examined in the frequency domain in an attempt to verify at which frequency the flap and torsion mode are merging to cause Flutter, and whether the 1st or 2nd flap mode is the cause. In other studies on Flutter [2], it is stated the second flapwise mode is usually interacting with the torsion mode because of the high relative torsional stiffness compared to the "soft" first flapwise mode. The system spectral response is analysed using a case for a mean wind speed of 15ms^{-1}. In the simulation, the operating conditions were brought as close to the Flutter limit as one could get without causing it to become unstable, which was to a rotor speed around 16 RPM and a corresponding tip speed around 107ms^{-1}. The identified spectrum is given in Figure 4.6.

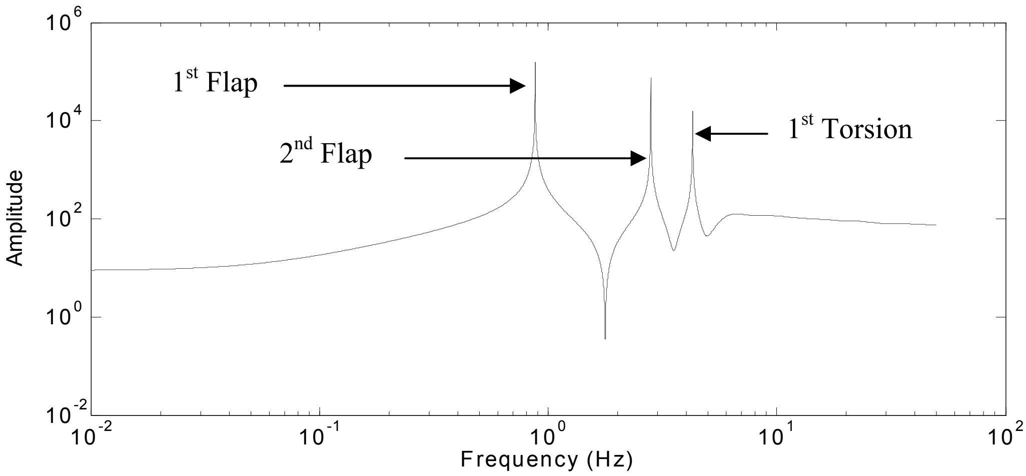

Figure 4.6 Spectrum of Blade Natural Frequencies at Operational Rotor Speed 16 RPM (Flutter Speed ~ 17.5 RPM)

The blade natural frequencies are identified in the figure and show the 1st blade flap mode is slightly higher at this rotational speed at about 0.9Hz (from 0.85 non-rotating). The second blade flap mode has increased from 2.3Hz to around 2.8Hz and the torsion mode has reduced to 4.2Hz (from 5.6Hz non-rotating). It appears the 2nd blade flap mode and 1st torsion mode are converging (as is the suggested case in other studies), which would see them merge somewhere between 3Hz and 4Hz to cause Flutter. This value is in the vicinity of values found from other studies with similar sized blades and properties [2] and [9]. This result gives some confidence in the methodology used to determine the Flutter limits.

The general trend for the Flutter velocity over the wind speed range is a decreasing Flutter speed for increasing wind speed. The Flutter velocity over the operating wind speed range of the UpWind turbine is given in Figure 4.7.

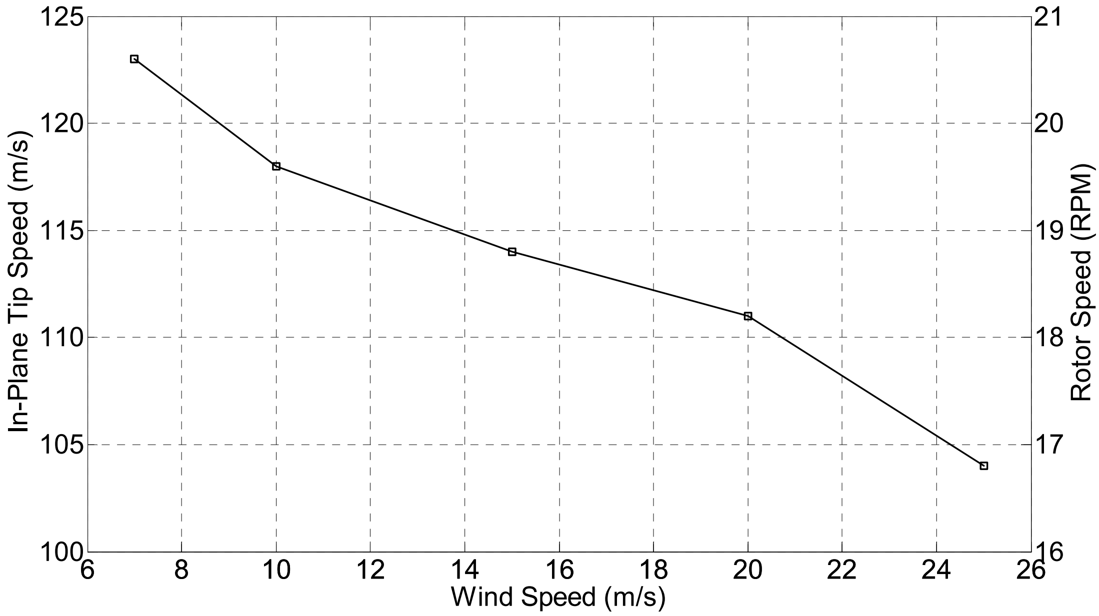

Figure 4.7 Flutter Velocity Over Given Range of Operating Wind Speeds

As suggested in the figure, the rotor speeds would have to be substancial for the UpWind turbine to enter a Flutter region (maximum design rotor speed is 12.7RPM). Obviously, this wind turbine design would most likely not experience Classical Flutter with its present blade structural properties and intended operating conditions. A study given in [9] also found for a 5MW blade of 60m, Flutter occurred at rotor speeds around 24RPM, which is comparable to that found here. The torsion natural frequency used in this study however was substantially higher at 8Hz, which might explain the higher Flutter speeds.

4.2.1 Centre of Gravity Offset Effects on Flutter Limits

Other studies have shown Classical Flutter to be heavily influenced by the centre of gravity offset from the blade shear. This is tested here as to the extent of its effect and also as an indication if the dynamic model is behaving according to what experiments suggest. A case is examined for a wind speed of $15ms^{-1}$ with the centre of gravity location exaggerated to be forward of the elastic shear axis by 1.5 times the equivalent amount as it is behind (refer to Table 3.3 for details); ensuring this does not place the COG in front of the aerodynamic centre so that Flutter is still possible. The resulting effect is presented in Figure 4.8. It is shown with the centre of gravity placed forward of the elastic shear axis, the Flutter limit has been increased from approximately $113ms^{-1}$ to $125ms^{-1}$, an increase of 10%. This therefore is in alignment with other Flutter analyses which show an increasing Flutter speed limit with such a position of the COG. The figure is also good for showing how the Flutter limit is being determined using a frequency sweep, since both plots are closely aligned while in the stable condition, and then deviation is shown for when the Flutter mode is excited.

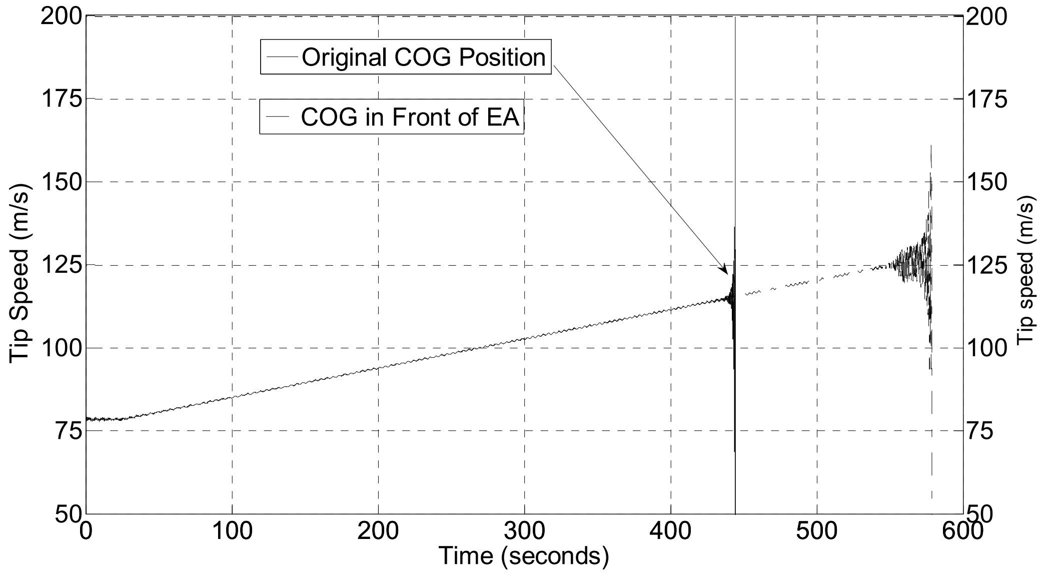

Figure 4.8 Extension of the Flutter Limit due to Placement of Centre of Gravity in front of Elastic Axis

4.2.2 Wind Shear & Tower Shadow Effects

So far only a steady wind field has been used to investigate Flutter. Real wind turbines operate in wind shear, which means as the blade rotates one full revolution, it experiences a higher wind velocity in the top half plane compared to the bottom, and therefore sees a periodic change in the angle of attack. Wind turbine blades also experience a perturbation on the angle of attack due to the presence of the tower, which interacts with the global flow field as the rotor passes by it causing the blade to respond. This too is periodic.

To test the effects this might have on the Flutter limits, simulations were run for the cases above with wind shear and tower shadow effects included. The results showed for all cases there was a noticeable decrease in the Flutter tip speed. The tip-speeds decreased by around $5ms^{-1}$. This is considered to occur possibly because as the turbine gets closer to its Flutter instability limit, the tower shadow effect is able to excite the blade dynamics sufficiently to induce the Flutter mode. This is one example of the many variable operating conditions wind turbines can operate in and highlights that Flutter needs to be thoroughly examined for all conditions. Time did not permit turbulence effects to be investigated, but it could be interesting to see the effects. The stochastic nature of turbulence may provide extra damping which could help stabilise Flutter, but it is left for another study to verify this.

4.3 Giant Wind Turbines – Bridging the Classical Flutter Stability Limits

It has been demonstrated the UpWind turbine could experience Flutter in operating conditions sufficiently above that it is operated in. It should also be noted that this turbine design parallels the largest commercial machines currently in operation. This begs the question of then; at what size will wind turbines be approaching the area of critical Classical Flutter stability limits?

Already presented in section 2.3.2 is an introduction to the topic of large wind turbines and possible trends in blade eigenfrequencies (from scaling laws) if blade manufacturing materials and methods follow the current projected path. Here an attempt is made to estimate at what size commercial wind turbines will have to be considered and tailored for avoidance of Classical Flutter. This is by no means a rigorous analysis, but should be enough to develop an appreciation for which generation of wind turbines are encroaching upon the Flutter limit.

To answer this question, the following cases are constructed to identify the projected design characteristics of giant wind turbines, and where possible, the simulation model is used to support the conclusions.

4.3.1 Case Analysis

Case 1

A very simplified case is to assume that the blade properties of the UpWind turbine for example, can maintain their structural integrity (eigenfrequencies) despite a significant increase in the blade radius. While this is certainly impossible (unless materials are revolutionised), this will provide an upper size limit of when a turbine may experience Flutter. It is further considered that in order to keep the turbine design practical, the tip speed ratio will have to be higher than those typical for MW machines today. This is because the torque generated in the rotor would become so large, massive generators would be required at low tip speed ratios. Two instances of tip speed ratios are used here to observe how critical it is, with details given in Table 4.2.

The next generation of wind turbines are envisioned to be in the 10-20MW range, therefore a good starting point is to take the simplified design of a 10MW turbine. The following parameters are an estimation of such a design.

Table 4.2 Possible Design Parameters for a 10MW Wind Turbine

<table>
<tr><th colspan="2">Power</th><th>10MW</th><th>5MW Reference</th></tr>
<tr><td colspan="2">Rotor Diameter</td><td>172m</td><td>122m</td></tr>
<tr><td rowspan="2">Angular Velocity (rated)</td><td>i)</td><td>9 RPM (tip speed ratio ~ 7)
V_{rated} ~ 11 m/s</td><td>12.5 RPM
V_{rated} = 11m/s</td></tr>
<tr><td>ii)</td><td>10.5 RPM – 13RPM (tip speed ratio ~ 9)
& V_{rated} b/w 11 ms^{-1} – 13ms^{-1}</td><td>-</td></tr>
<tr><td rowspan="2">Tip Speed</td><td>i)</td><td>82 m/s</td><td>82 m/s</td></tr>
<tr><td>ii)</td><td>95 – 117 m/s</td><td>-</td></tr>
<tr><td rowspan="2">Rotor Torque</td><td>i)</td><td>10 MNm</td><td>4 MNm</td></tr>
<tr><td>ii)</td><td>7 – 9 MNm</td><td>-</td></tr>
</table>

These rough estimates of a 10MW wind turbines operating parameters show that if a higher tip speed ratio is chosen as in ii, (i.e. tip speed ~ 9), which is favourable to reduce torque, it is possible for the tip speeds to reach close to the Flutter limit (remember, this is assuming unchanged blade characteristics from the 5MW design). This would depend on the choice of rated wind speed, as here it is assumed to range from 10-13ms^{-1} at higher tip speed ratios. The torque at higher tip speeds is much less than if the turbine was designed for tip speeds comparable to the common designs today. If it is desired to reduce the torque further, then most likely, the Flutter boundary would be breached. However, based on the above numbers and the main assumption, Flutter probably could be avoided with carefully chosen design and operating characteristics for a 10MW machine.

It is now assumed that with a large increase in blade length, more flexible blades will result. This assumption is made due to the design problem of keeping the blades to a low mass to keep in-plane bending stresses acceptable, for example by increasing chord length to blade thickness ratio to create more slender blades. This most likely will lead to a lowering of the Flutter velocity to that identified for the UpWind turbine. Previous studies have shown [8] the Flutter limit reduces as the gap between the flap and torsion eigenfrequencies decreases. This takes us to the next case, where the stiffness of a 10MW blade is estimated for the case of a more slender blade and the effect on Flutter limits investigated.

Case 2

The UpWind turbine blade was up-scaled to that equivalent of a blade radius of 86m for a 10MW turbine. The method used was to scale the chord length of the new blade according to the increase in blade radius and using this chord length as the base to make new estimates for:

- Mass
- Stiffness (flap, edgewise, torsion)
- Polar Moment of Inertia
- Centre of gravity offset from shear axis; and
- Aerodynamic centre offset from shear axis

The new eigenfrequencies of the blades were determined using the methods mentioned in section 3.1.4.1. The angular velocity of the turbine was adjusted to keep it operating at present day trends of a tip speed ratio of about 7. This will indicate whether Flutter could occur within a typical operational envelope of a future wind turbine.

The basic relations used for the up-scaling can be viewed in Appendix A.VI. The new fabricated 10MW design has the properties given in Table 4.3.

Table 4.3 Scaled Parameters for a 10MW Wind Turbine

Rated power	10MW	5MW Reference
Number of blades	1	1
Rotor Diameter	172m	122m
Maximum Rotor Speed	~9 RPM	12.5 RPM
1st Flap Eigenfrequency	0.55Hz	0.85Hz
2nd Flap Eigenfrequency	1.25Hz	2.3Hz
1st Edgewise Eigenfrequency	0.80Hz	1.2Hz
1st Torsion Eigenfrequency	4.00Hz	5.6Hz

A main assumption for the new eigenfrequencies is that the blade thickness of the up-scaled blade remains constant (i.e. so a more slender blade results increasing the flexibility, as would result if blade mass is minimised and new high strength materials are not used); therefore the moments of inertia for determining new stiffness are related to the newly distributed chord length only. It would be expected for the thickness to chord length ratio to be designed in an optimal manner in reality, such that bending and torsion stiffness is not compromised in a trade-off with the additional blade mass causing higher in plane stresses due to gravity.

4.3.2 10MW Wind Turbine Flutter Analysis

With the turbine properties inputted into the WIMSIM model with the adjusted wind speed – rotor speed control for a tip speed ratio of 7, the results of the simulations show at lower wind speed (under $9ms^{-1}$) the turbine comes to a stable response. At higher wind speeds, the turbine is unable to meet equilibrium and it is possible the turbine is in the Flutter operational envelope. It was seen in the previous section, the Flutter speed decreases with increasing mean wind speed, which might explain why the turbine runs in the low wind speed range in the simulation.

To test this, the Flutter speed is tested at the stable operating wind speed of $8ms^{-1}$ to gauge how far away the Flutter point is. If Flutter is close to this operational state, it may be reasonable to assume that other states above this wind speed are close or in the Flutter zone, therefore indicating that large wind turbines running with similar operational characteristics (tip speed ratios) of today may be prone to Flutter. The Flutter point for the case of $8ms^{-1}$ wind speed is presented in Figure 4.9.

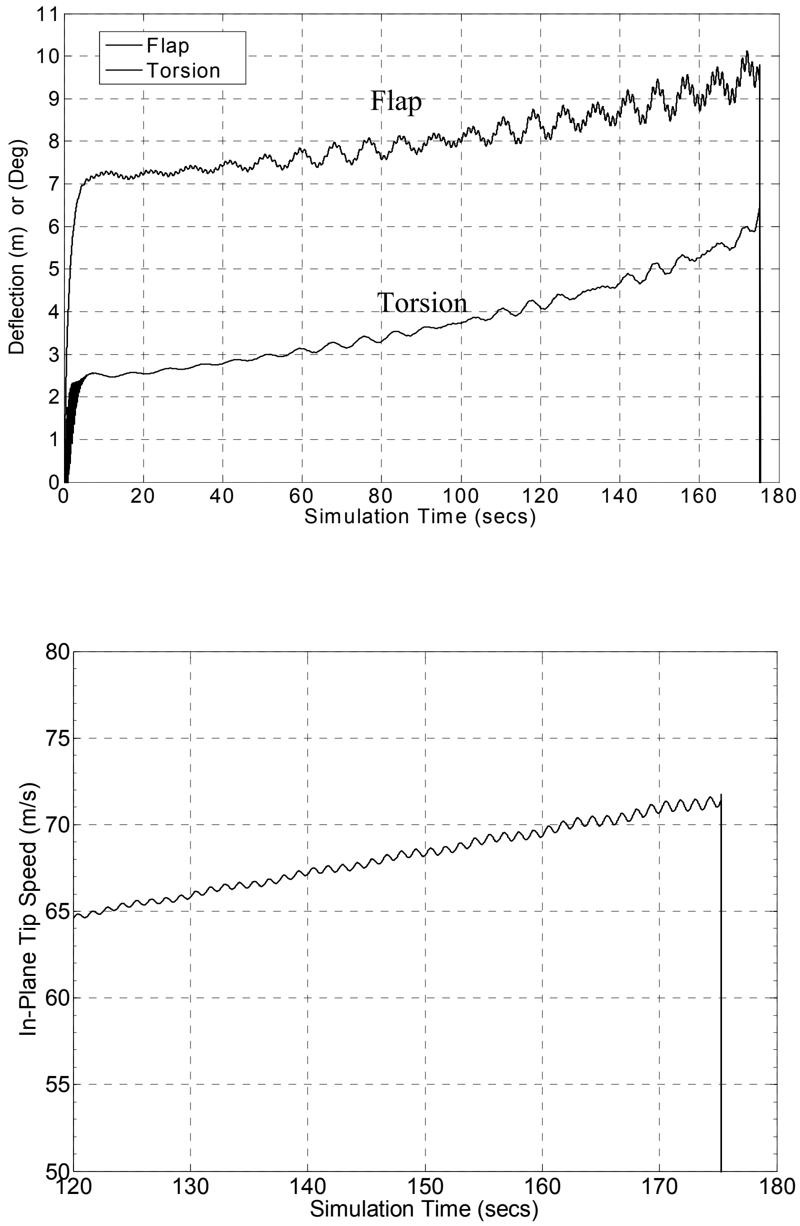

Figure 4.9 Top: Flapwise & Torsion Deflection with Increasing Rotor Speed to the Flutter Point Bottom: Tip Speed up to Flutter Point

The tip speed at nominal operation for a wind speed of $8ms^{-1}$ is around $52ms^{-1}$. The Flutter point was reached at around $72ms^{-1}$ for the up-scaled blade. This shows a dramatic decrease in the Flutter limit compared to the original blade of 61.5m radius, which showed a Flutter limit at a tip speed of approximately $120ms^{-1}$. This would indeed indicate Flutter may pose problems for larger wind turbines.

Looking at turbine operation at higher wind speeds, the rated speed of the 10MW turbine is around 9RPM. This puts the tip speed at around $80ms^{-1}$, already above the Flutter limit just shown in Figure 4.9. Given the trend shown for the 61.5m blade Flutter limits in Figure 4.7, it could be argued that at higher wind operational states for the 10MW turbine, it will be prone to Flutter, which is supported by the simulated unstable model at wind speeds above $8ms^{-1}$. It should be kept in mind; this is providing it is designed to run at a tip speed ratio of 7.

It was found for even a tip speed ratio of 4, at the end of the wind operating range ($\sim 25ms^{-1}$), which should give the lowest Flutter limit; the turbine was barely stable and showed evidence of Flutter. Thus, it could be concluded that turbines approaching 10MW and beyond will most likely need to be designed taking Flutter carefully into account, which will mean scrutinising its intended optimal operating states and blade structural design. Aeroelastic design using the whole wind turbine will most likely be required to prevent any other means being necessary to keep large turbines stable; for example, the use of a smart rotor using actuated trailing edge flaps.

The remainder of the report is dedicated to testing the merit of using actuated trailing edge flaps as a means to mitigate Classical Flutter instability in wind turbines, which may have applications in solving the problems just exhibited for a 10MW wind turbine.

5 Smart Rotor Design for Flutter Suppression

In the preceding sections, the implementation of a dynamic model to capture the effects of Flutter was described and an attempt to determine the Flutter margins of the UpWind turbine (rigid hub and isolated blade analysis) and an up-scaled version to 10MW was made. The outcome of the analysis suggested a current 5MW wind turbine is suitably far from the Flutter limits in its operational conditions, but future larger turbines approaching 10MW and beyond could be at risk.

It is now interesting to explore whether the Flutter of a blade can be controlled using a trailing edge flap (TEF), or otherwise called a 'smart' rotor such that it is possible to stabilise a blade temporarily in the Flutter zone or even stabilising for full operation within the zone. It is now useful to introduce the working principle of a 'smart' rotor as used in the context of this study.

Essentially, a deflection of the trailing edge of the aerofoil alters the lift force experienced by that aerofoil. For example, with reference to Figure 5.2, a positive trailing edge flap deflection - δ (downward position) will cause an increase in the observed lift. For a negative deflection, the opposite can be said. It might be prudent to then ask how these aerodynamic properties can be used to stabilise Flutter. This is explained with the aid of Collar's Aeroelastic Triangle in Figure 5.1 [13].

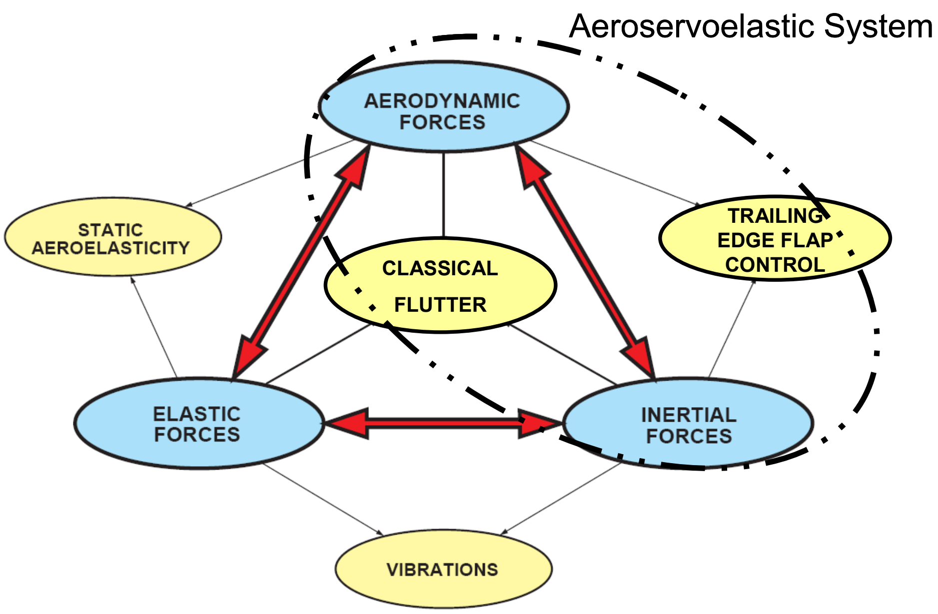

Figure 5.1 Collars Aeroelastic Triangle Showing the Aeroservoelastic System Concept

Figure 5.1 provides a definition of aeroelasticity, showing the coupling of the aerodynamic loads relative to structural elastic and inertial response. On each point of the triangle is shown the governing loadings which determine the type of response of the structure. For example, vibrations are a result of inertia in a structure of given mass distribution affected by its elastic forces trying to bring it into stable equilibrium. However, if external aerodynamic forces are added to the mix as shown, a dynamic coupling triangle is formed to define the mechanics of aeroelastic instabilities, of which the Classical Flutter phenomenon in this study belongs to. Likewise, there is a clear link from inertia to aerodynamic forces, which suggests that interfering with the aerodynamics (i.e. controlling lift forces) means we can change the inertial behaviour existing in the structure. This underpins the reason for using TEF geometry to gain control over these processes and tune the system to a desired state. Inclusion of a control surface (TEFs) in the above Aeroelastic model defines the Aeroservoelastic Control System. It can be envisioned from this principle, that a controllable TEF could reduce the dependency of Classical Flutter from being based on external loading conditions and fixed aerofoil design (unchangeable mass and stiffness distribution). This means the instability could potentially be avoided.

To this end, this final section aims to show through using simple control analysis techniques (e.g. Proportional, Integral or Derivative PID controllers), it is possible to mitigate against Flutter-and therefore potentially other known instabilities using a trailing edge flap. The intention is not to design a fully operational and optimised controller over the full gamete of wind turbine operating conditions, but rather to illustrate it might be achievable and worth more investigation in a more detailed analysis using both full wind turbine aeroelastic analysis and controller design.

In section 5.1, the inclusion of trailing edge flap aerodynamics into the modified Theodorsen aerodynamic model is outlined. Section 5.2 gives the methodology used to design the control system for a Flutter condition with details and results of the experiment given in section 5.3 Conclusions are then drawn on the merit of a ‘smart rotor’ for Flutter control as well as discussion on the limitations of the current analysis in terms of the modelling methods employed.

5.1 Trailing Edge Flap Geometry & Aerodynamic Coefficients

A general discussion of the aerodynamic model is given in Section 3.1.3, but with the details of the trailing edge flap integration and design reserved until now. The WIMSIM model is designed for unsteady aerodynamics including a trailing edge flap using Theodorsen’s theory modified by Wagner and Kussner functions for computational efficiency. It is represented in state-space format in WIMSIM with the complete governing relations and actuated flap performance validation given in Appendix A.I. Presented here are simplified relationships for illustrating how the angle of attack relates to a trailing edge flap deflection for determination of the lift coefficient, and hence blade forces. Parameters defining the trailing edge flap geometry and deflections relative to the aerofoil blade are also given.

Figure 5.2 shows the aerofoil and trailing edge flap combination. It should be noted that the changes in lift from a trailing edge flap deflection are assumed to occur at the aerodynamic centre, and no other rotational moments caused from the geometry change are considered. The trailing edge in this study is assumed to have negligible effects on the blade dynamics, i.e. the inertia and deformation of the TEF is neglected.

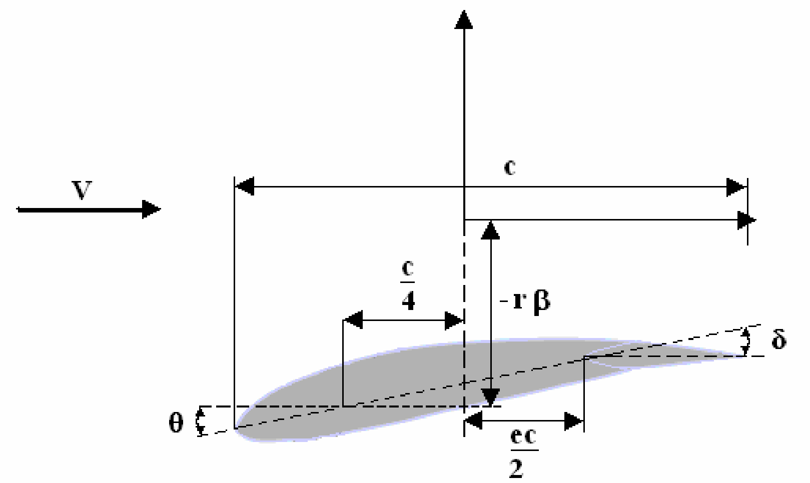

Figure 5.2 Aerofoil Cross Section Showing Additional Trailing Edge Flap Deflection and Related Geometry for Aerodynamic Model

The important parameters used in the aerodynamic equations are the non-dimensional trailing edge flap hinge location – *e,* and the trailing edge flap deflection – *δ [rad]*. The hinge location can therefore be chosen according to the ratio of desired trailing edge flap chord to aerofoil chord, i.e.

5.1

$$e = 1 - 2(\frac{c_{te}}{c})$$

where,

c_{te} is the chord length of the trailing edge flap

c is the aerofoil chord length

With the hinge location defined, the following coefficients according to Theodorsen for input into the aerodynamic equations are:

5.2

$$F_1 = e\cos^{-1} e - \frac{1}{3}\left(2 + e^2\right)\sqrt{1 - e^2}$$

$$F_4 = e\sqrt{1 - e^2} - \cos^{-1} e$$

5.3

$$F_{10} = \sqrt{1 - e^2} + \cos^{-1} e$$

$$F_{11} = \left(1 - 2e\right)\cos^{-1} e + \left(2 - e\right)\sqrt{1 - e^2}$$

The role of Eq. 5.2 and 5.3 can be viewed in the following simplified expressions for determining the lift (c_l) from a TEF deflection.

The total lift on the aerofoil is the sum of its circulatory ($c_{l,c}$) and non-circulatory ($c_{l,nc}$) constituents:

$$c_l = c_{l,nc} + c_{l,c}$$

The non-circulatory component of lift is a function of the quasi-steady angle of attack (α_{qs}) and TEF velocity and acceleration, including its geometric coefficients as defined above:

$$c_{l,nc} = F(\alpha_{qs}) + G(\dot{\delta}, \ddot{\delta}, F_1, F_4)$$

where the quasi-steady angle of attack for the aerofoil is based on inflow conditions, blade accelerations, motion, etc, as given by:

$$F(\alpha_{qs}) = f(\varphi, \theta_t, \theta_p, \dot{\beta}, etc)$$

The circulatory component of lift is given by the Wagner and Kussner as functions in quasi-steady angle of attack for the blade, and quasi-steady angle of attack due to a TEF deflection (δ_{qs}):

$$c_{l,c} = H(\alpha_{qs}) + J(\delta_{qs})$$

which relates the quasi-steady angle of attack due to TEF deflection as a function of TEF position, velocity and geometry defined by Theodorsen's coefficients.

$$J(\delta_{qs}) = j(F_{10}, F_{11}, \delta, \dot{\delta})$$

The full relationships for determining the quasi-steady angle of attack and thus, lift coefficient for a TEF deflection are given in Appendix A.1.

The final parameter of the trailing edge flap to specify is the span of blade it covers. For the current study, the flap is assumed to begin at the tip of the blade running inboard to a desired location suitable for providing a sufficient moment arm. Trailing edge flap chord and span optimisation is given some attention in section 5.3 when the controller and TEF geometry assembly is tested for it ability to suppress Flutter.

5.2 Trailing Edge Flap Controller Design (Smart Rotor)

Up to this point, the WIMSIM model has been identified as being able to capture the effects of Classical Flutter and details of the aerodynamic effects for an aerofoil with a trailing edge flap (TEF) have been given. It is now desirable to implement a control scheme for actuation of the TEF such that when the rotor experiences Flutter, the control scheme will act to keep the wind turbine stable. The goal is to design a simple feedback controller, such as using Proportional, Integral or Derivative action on the error of the desired system state to show the feasibility of using TEFs to control Flutter, and perhaps even other instabilities. The items addressed for the design of the Flutter suppression mechanism in this study are:

- Implementation of a flap actuator with given frequency and damping characteristics with output of position, velocity and acceleration
- System identification techniques to create a linearised version of the total aeroelastic model for a given operational mode
- Controller design using root locus and frequency response analysis
- Choice of feedback for the controller

The controller is not designed over the full wind turbine operating conditions, but rather a single condition is chosen where Flutter is evident to test the outcome of the smart rotor. For convenience to carry out the simulations, it was decided to reduce the blade properties to induce Flutter more readily, using both a test case for increasing rotor speed to the Flutter point, and using a step input in rotor speed close to the instability limit.

5.2.1 State Feedback Variable

The feedback variable for input into the controller is chosen to be the blade tip flap (out-of-plane) acceleration. This was decided for because of proven methods currently available to measure blade acceleration on a real wind turbine. Since it is desirable to keep the testing of a TEF as realistic as possible, the flap acceleration is a logical choice for monitoring the state of the system. If it is proving difficult to obtain a satisfactory controller with such feedback, another option worth exploring could be to use the torsion degree of freedom, as this would also carry information of the Flutter instability with it.

5.2.2 Trailing Edge Flap Actuator Design

A standard dynamic actuator concept is employed wherein an applied voltage for example, is used to drive the actuator to the desired position with predefined frequency and damping characteristics to achieve a desired flap response suitable for the application. The voltage is regulated according to the feedback variable governing the state of the system and voltage is adjusted to provide the required response of the trailing edge flap (TEF) to try and equilibrate the system. A second order system is chosen to represent the TEF dynamics with feedback of position and velocity. The TEF dynamics can be represented by:

5.4

$$\ddot{\delta} + (2\xi\omega)\dot{\delta} + \omega^2\delta = \omega^2 V$$

where,

$\delta, \dot{\delta}, \ddot{\delta}$ is the flap angle and related angular velocity and acceleration [rad, rad/s, rad/s^2]

ω is the simulated frequency of the TEF [rad/s]

ξ is the simulated damping in the actuator

V is the applied voltage to the actuator [V]

Eq. 5.4 can be represented in block diagram form to illustrate how the feedback of TEF position and velocity is used to achieve the desired TEF position.

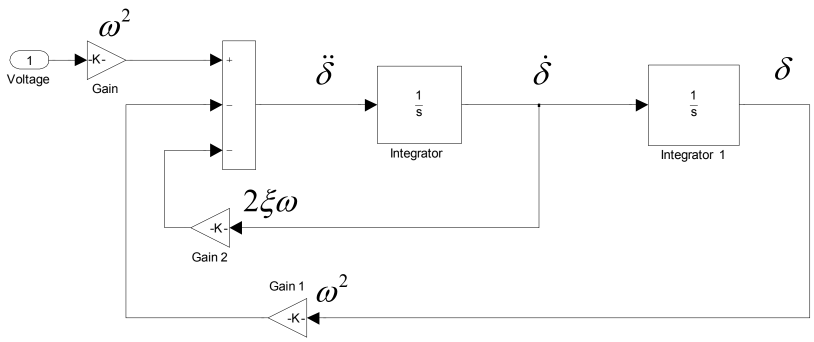

Figure 5.3 Block Diagram of Trailing Edge Flap Actuator with Feedback

Figure 5.3 shows each feedback loop and voltage input entering the summing junction block, which to bring the system into equilibrium, will try to reduce the output of the summing junction (error) to zero through continual acceleration of the flap until the desired system state is achieved through monitoring of the system feedback. The frequency and damping characteristics are chosen to achieve a desired response of the TEF, such as the amount of overshoot and time taken to arrive at the desired position from the disturbed system.

A general configuration for the actuator is adopted in this study as the focus is not to design a fully optimised controller with finely tuned dynamics. A suitable flap frequency is required so the dynamics are fast enough to influence the system, while damping will ensure not too much overshoot occurs. Some trial and error of parameters was used for the actuator without too much concern for optimising the response, leading to the characteristic parameters shown and response as in Figure 5.4.

TEF Frequency	Damping
20Hz	0.1

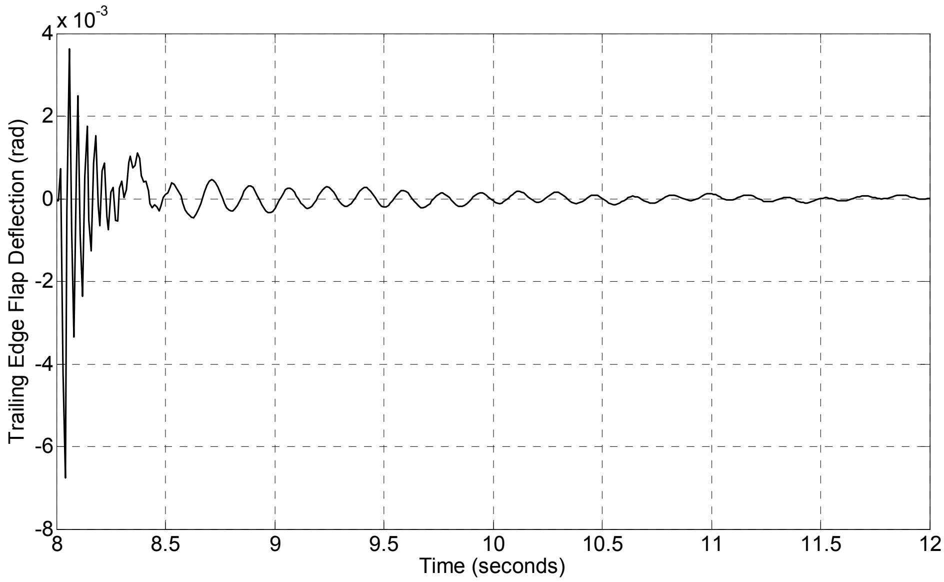

Figure 5.4 Trailing Edge Flap Response to a Step Input

For a step input, the response of the TEF is shown to be highly oscillatory and responds quite quickly to return the system to a new equilibrium position, at which time the acceleration of the flap returns to zero. This configuration for the actuator is placed within the WIMSIM simulation environment so system identification techniques can be applied to obtain a linearised model of the total system dynamics and subsequently used to design the control algorithm for the Flutter suppression experiment.

5.2.3 System Identification

Classic control techniques for an actuated TEF to control Flutter are employed which follows these primary tasks:

- Select a feedback variable of the system which will describe the state of the system for the controller
- Obtain a linearised model of plant dynamics (e.g. single input – single output transfer function) close to the state of that which will be controlled
- Analyse the model stability and use root locus / frequency response techniques to design a Proportional, Derivative or Integral action controller to effectively change the overall system behaviour (adding poles to the system)

The system identification procedure to design the controller for Flutter in this study is a common methodology employed in a range of control applications to obtain linearised models of plant dynamics. Control design for a system is most easily performed when the dynamics of the system are made linear so that a transparent relationship is obtained for the response (output) of the system for any given input. The system dynamics can be made linear if we choose particular operating states about which to linearise, therefore to design a controller over an entire operating range of a wind turbine for example, would require many linearisations. The objective here however is not to undertake such a task but to test the feasibility of controlling Flutter, so minimal operating points are considered.

A schematic of the system identification procedure is given in Figure 5.5 [28] along with a brief description of the involved steps undertaken in the current analysis. The author refers you to the theory of [28] for a step by step account of carrying out the system identification procedure used in this analysis.

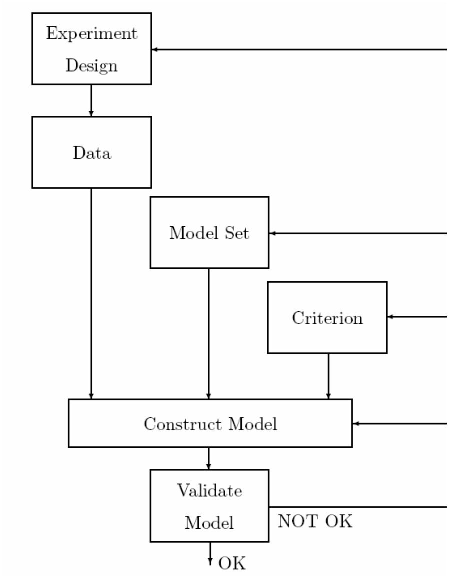

Figure 5.5 Model Identification Procedure [28]

Flutter Control Experimental Design and Data Measurement

This step refers to the model set-up for collection of input and output signals of the dynamics of the system. This allows a linearisation of dynamics to be made by selecting an input to sufficiently disturb the system such that it is exciting the required dynamics so that the output signal has an imprint of the required information to relate input to output signals. For the system at hand, this means the experiment is set-up with the feedback state of blade tip acceleration to be measured for the output signal. Since the goal is to create a TEF controller, random voltage input into the TEF actuator is applied to excite and create the imprint of the system dynamics. In this way, a linearised model can be obtained to give the response of the system for a given TEF deflection. A schematic of the experimental set-up is given in Figure 5.6.

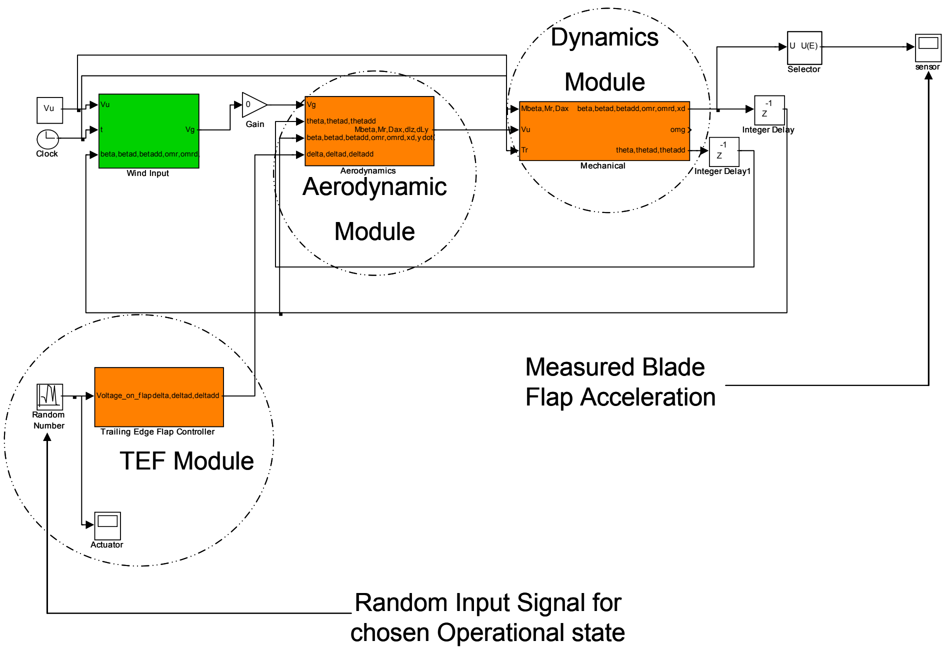

Figure 5.6 Experimental Set-up for Identification of System Dynamics

A random TEF input is directed through the aerodynamic module and the blade response is measured as an open loop arrangement as shown. System Identification software available in Matlab is used to perform the analysis, which includes the tools to perform the following sub-steps as in Figure 5.5.

Model Set

Model set refers to an identified model which adequately models the measured data of the experiment (i.e. best predictor model – matching the output for a given input). The identification software allows a range of models to be used to find a suitable predictor of the measured data, and it is usual to try a range of models to find one which meets the criterion for the control design purpose. The model most suited to the present analysis is the Box-Jenkins model, which seemed to give the closest fit to the measured data. The Box-Jenkins model set is determined using 4 polynomials, two of which form a fractional coefficient of the input term, and another two forming the fractional coefficient of the added disturbance to the system. A linear model is built from these polynomials according to the following [28]:

5.5

$$y(t) = G(q)u(t) + H(q)e(t)$$

where for the Box Jenkins model the transfer functions are represented by the polynomials in *B, F, C* and *D* as in Eq. 5.6. The disturbance on the system is given by $e(t)$.

5.6

$$G(q) = \frac{B(q^{-1})}{F(q^{-1})}$$
$$H(q) = \frac{C(q^{-1})}{D(q^{-1})}$$

An example of a Box Jenkins parametric model identified for use in designing the controller is given in Figure 5.7. It's an overlay of the measured data to that predicted by the simulated model. A small portion of the time range is selected for ease of comparing the fit. The best fit was obtained using a 5th order polynomial function.

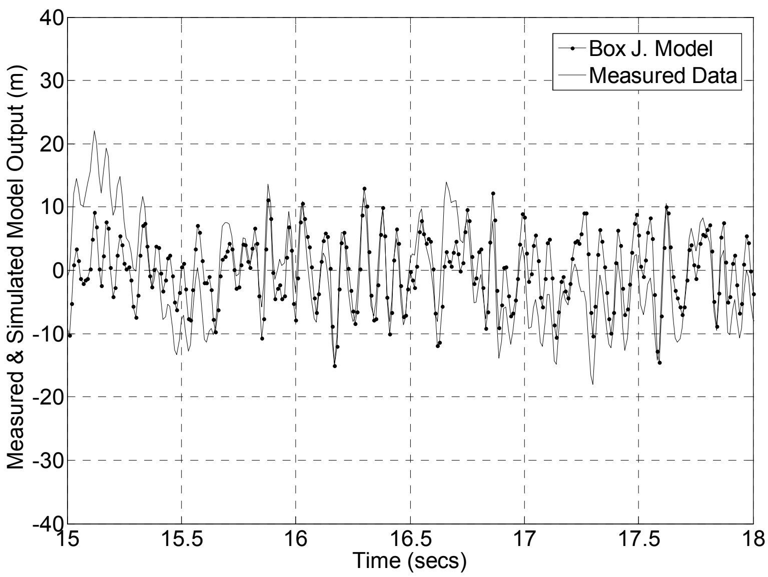

Figure 5.7 Box Jenkins Linearised Model Predicting Measured Blade Tip Accelerations

For this case, reasonable agreement is found but some error is evident as is generally the case. The error is deedme acceptable according to the following validation step.

Criterion and Validation

Since the main intention here was to use Box-Jenkins model from the onset for ease of defining a single input-single output system, validation of the model is the final step to judge whether the system is adequately identified. Validation in this case is the determination of the prediction error (residual error) from the model and measured data (i.e. subtraction of predicted response from measured data). A validation tool exists in the identification software for easy determination if the model is suitable. The residual error function for the simulated case above is given in Figure 5.8. It shows the error is within the defined bounds indicated, therefore validating the linear model as a good predictor to the simulated dynamics of the system. With such a model defined, it is now possible to represent the input for TEF deflection as a system transfer function with blade tip acceleration for output. This provides the basis of designing the controller.

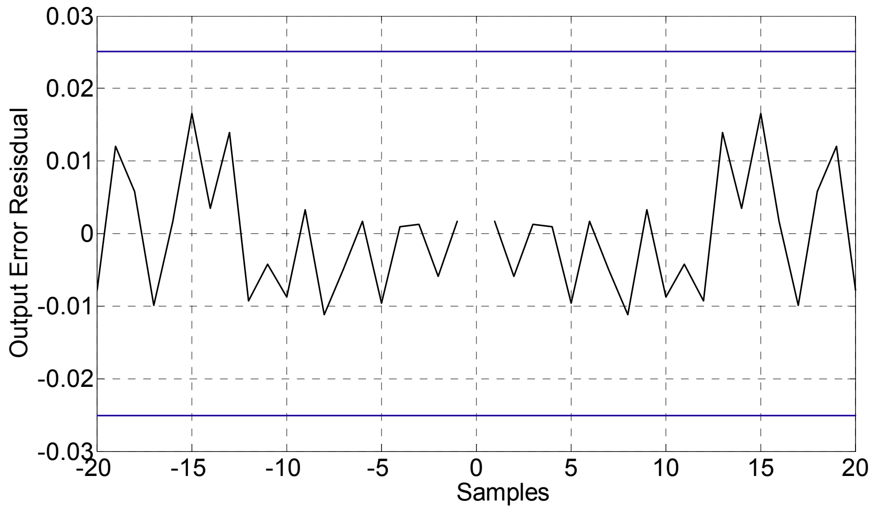

Figure 5.8 Residual Error on Box-Jenkins Linearised Model for Flutter Suppression Experiment

5.2.4 Controller Design for Classical Flutter Suppression

Up until now, we have a linearised model of the whole system defining the wind turbine, including a TEF, at a specific operating point close to Flutter. It is important to be close to the Flutter point because for a controller to be designed to work requires building it from the known system so when inserted into the non-linear model, it does in fact change the system dynamics as intended. For each operating state, a different controller would be required.

A control system toolbox in Matlab can be used to design a controller using either root locus or frequency response techniques. It makes use of the transfer function as obtained in the system identification process and the frequency response of the system can be analysed.

The idea is to modify the transfer function characteristics (poles, zeros, etc) to design a desired change into the original system dynamics for the given operating condition (i.e. design a controller). This modified transfer function, or rather, controller, can be inserted into the non-linear model and supply the desired state to the TEF actuator according to the feedback variable of blade tip flapping acceleration. This concept is shown in Figure 5.9.

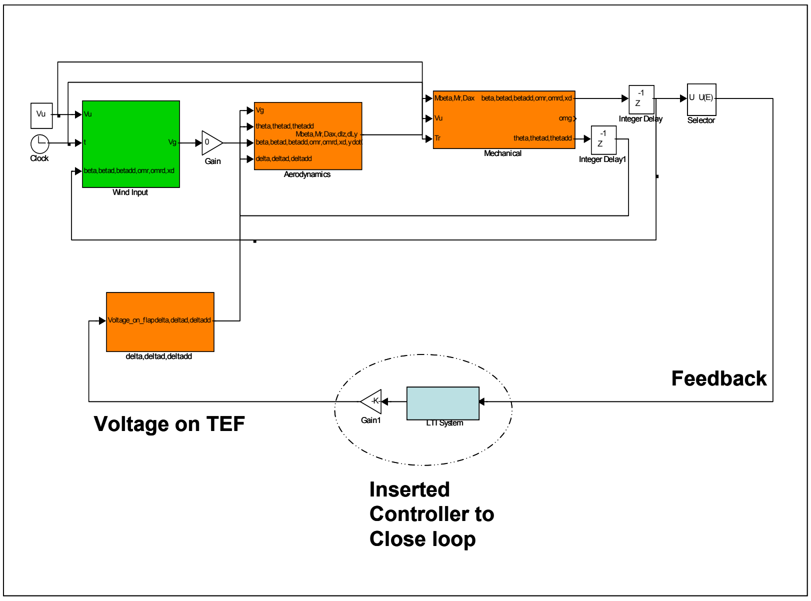

Figure 5.9 Implementation of Controller into Non-Linear Model

It was attempted to keep the controller as simple as possible and a single PID Proportional Integral Differential controller was experimented with to combat Flutter. The root locus plot of the original identified system is shown in Figure 5.10.

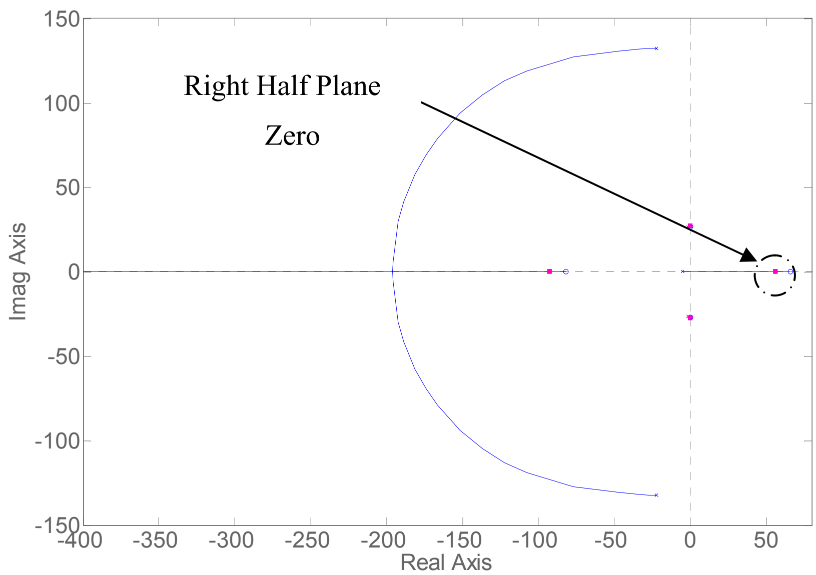

Figure 5.10 Root Locus Plot of the Original System dynamics

The original root locus plot shows the system to be open-loop unstable with both a pole and a zero in the right half plane. The pole could be moved through addition of gain but the same cannot be said for the zeros presence. In control system theory, it is known systems with right-half plane zeros are intrinsically difficult to control. The right side zero phenomenon has been seen in aircraft (aerodynamic) applications before and in this case is attributed to the location of the centre of mass from behind the elastic axis, which for changes in lift, acts as a moment arm causing additional variations in the angle of attack and more unstable response. The centre of gravity in front of the elastic axis in such an application causes the system to be inherently stable. It is therefore possible this same phenomenon is present in this analysis since the centre of gravity offset to the elastic axis is captured specifically in the dynamic model and also is behind the elastic axis. It is suggested this should be a topic to pursue in a subsequent analysis.

It may be possible to obtain a system transfer function with no right half-side zeros if a multiple input-output linearised model is obtained. This could allow for more information about the system and finer tuning of parameters to avoid the case above. This was not done for this study, with the original root locus plot being used for compensator design.

The designed compensator from the identified system transfer function is given in Figure 5.11.

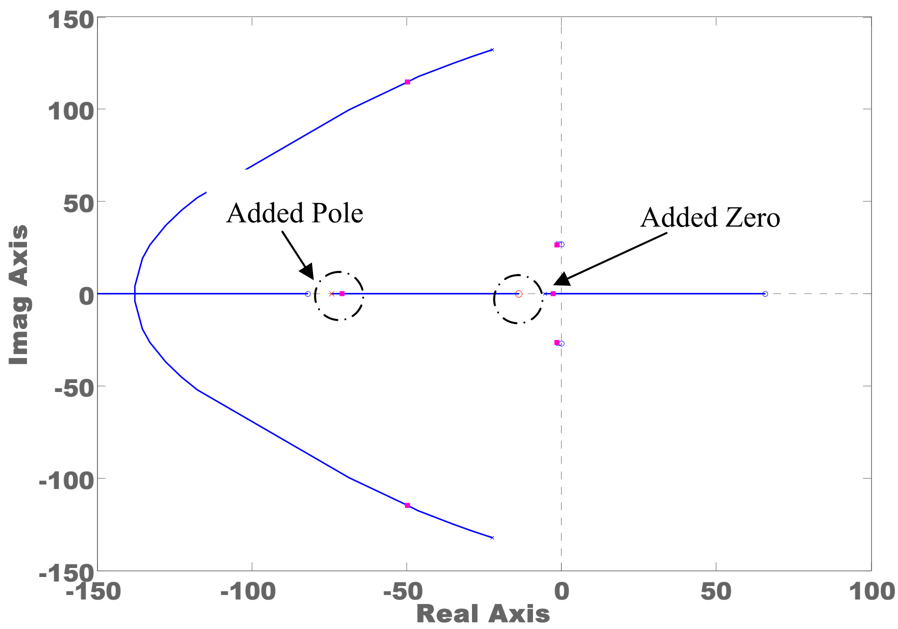

Figure 5.11 PID Compensator Root Locus Plot Showing Added Pole and Zero for a Desired Response

The pole and zero were added to try and create a stable system and with a desired response. The locations were chosen using trial and error as to try and draw the root locus gain lines into the left-hand plane. This compensator can be exported into the non-linear model and tested in the condition it was designed for. In section 5.3, the Flutter case set up to test the above compensator is described and results showing the validity of using TEFs to control Flutter are analysed.

5.3 Flutter Suppression Analysis

5.3.1 Experimental Set-up

As stated at the beginning of the chapter, for ease of performing the control of the Flutter analysis, the UpWind blade properties have been modified to induce the mechanism of Flutter at low rotor speeds (low blade tip velocity). This means the blade torsional stiffness was reduced and the centre of gravity was placed further aft of the elastic axis. A wind turbine operating region was chosen for a zero pitch angle at a wind speed of 8ms^{-1} to be sure the simulation is as realistic as possible (i.e. to eliminate control issues of the wind turbine as it approaches rated wind speed). A real controller would be required to operate over the full operational range of the wind turbine, but here only one case of turbine operation is examined, as it is assumed if one case can be controlled, it is likely to be the same for the others (not without challenges I'm sure). The new properties of the blade, along with the dimensions of the TEF are given in Table 5.1.

It is appreciated both the controller dynamics and TEF dimensions (chord and span) would be very important in obtaining an overall optimised configuration to control Flutter, however, the present study is limited to using raw values suitable for the purpose of merely showing if Flutter can be stabilised with a TEF. It is left for future studies to focus on optimisation of controlling the instability should the topic be pursued.

The aspects that were considered in choosing the TEF dimensions to keep the results realistic were to try and use as little span as possible starting from the tip of the blade going inboard; and a ratio of TEF chord to aerofoil chord between 0.1 and 0.25. It was considered important to use as little span as possible because the TEF is assumed to remain rigid in flapwise bending relative to the aerofoil (i.e. it does not deflect according to the mode shape of the aerofoil). Therefore, if the TEF covers the tip region of the blade only, this part is roughly more linear than the inboard region (see Figure 3.9 to Figure 3.11) and should preserve the integrity of the geometric relations defining the aerodynamics between aerofoil and TEF deflection.

It is desired to keep a small TEF chord to aerofoil chord ratio such that the structural integrity of the blade near the tip is maintained and to minimise the size of the TEF such that practically sized actuating power is required, thereby reducing bending moments about the hinge points.

Table 5.1 Wind Turbine, Blade and TEF Parameters Defining Flutter Experiment

Wind Speed	8 ms^{-1}
Rotor Speed	8.5 RPM
Torsion Frequency	4 Hz
COG Offset (% extra original value)	30%
TEF Frequency	20 Hz
TEF Chord Length (% of aerofoil chord)	20 %
TEF Span Length (% of aerofoil span)	30%

Two methods have been employed to test the controllability on the Flutter limit. The first is to take advantage of the reduced blade properties by using a step input on the rotor speed to induce Flutter. The response was examined closely to determine if it was in fact Flutter occurring. Based on the analysis of Flutter behaviour in preceding sections, it was deemed the blade was sent into a classical Flutter mode through a step increase from 8.5 RPM to 9.6 RPM.

The second method is to validate the Flutter mode of the previous method, whereby once again the rotor is allowed to gradually speed up to the Flutter point with the controller in place. It would be expected the Flutter speed to be quite low, since the relatively small step input in rotor speed in the previous case was enough to cause the instability. This case will also test how the controller performs for continually changing system dynamics and give an indication how far the Flutter limit is extended with TEF control.

5.3.2 Trailing Edge Flap Performance

Figure 5.12, Figure 5.13 and Figure 5.14 show the performance of the TEF on suppressing Classical Flutter for the two cases mentioned above. Shown for each case is the simulation without the controller in place to preview the occurrence of the instability, followed by a simulation with the controller installed.

No Controller	Installed Controller
Torsion Response - Step Input of Rotor Speed	Torsion Response – Stabilised after disturbance
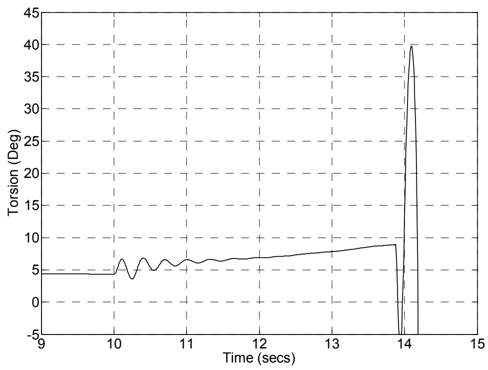	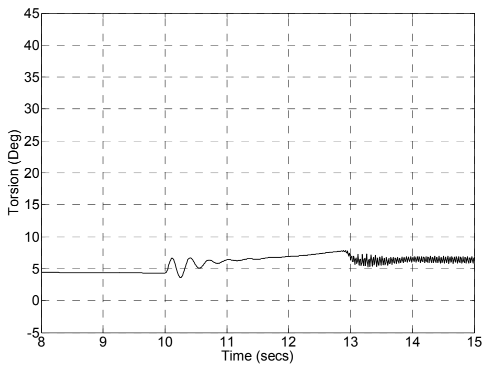
Flap Response - Step Input of Rotor Speed	Flap Response - Stabilised after disturbance
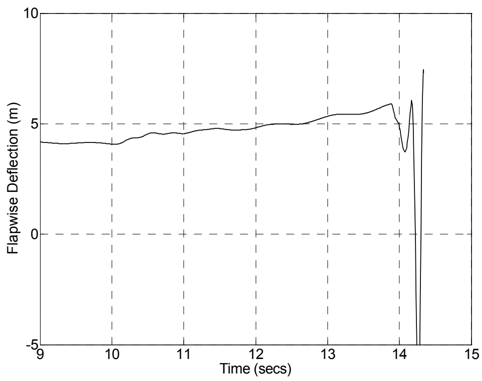	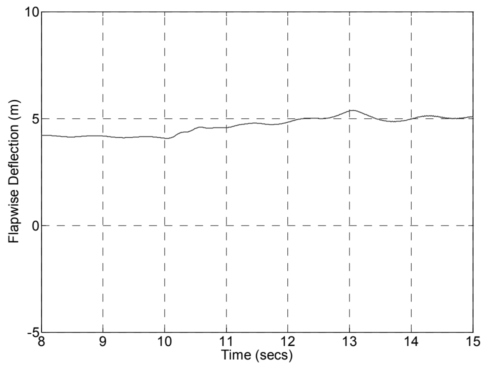
Step Input on the Rotor Speed	Trailing Edge Flap Response to Flutter
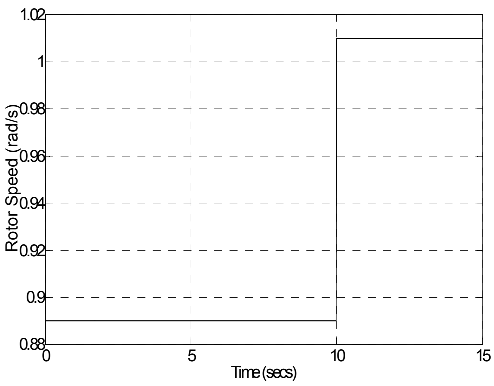	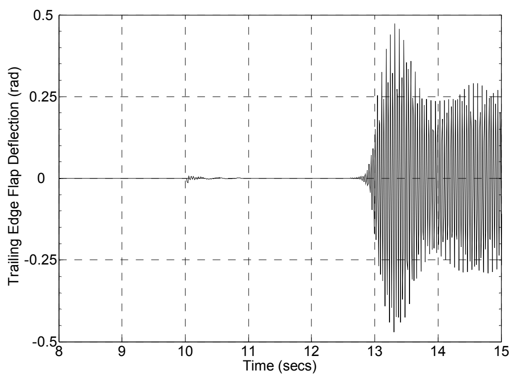

Figure 5.12 Induced Flutter for Step Input on Rotor Speed (Step Input at 10 secs) and TEF Controller Response (Bottom)

After a step input (at 10 seconds simulation time) on the rotor speed, the response of torsion and flapwise deflections start to drift, increasing in magnitude until rapid Flutter occurs within 5 seconds after experiencing the disturbance. For the simulation with added controller, after the disturbance, again the drift occurs to the same point where Flutter is reached, but now the TEF starts to act and stabilises the response to reach a new equilibrium of elastic torsion of about 6 degrees (up from ~ 4.5 degrees) and flap deflection of approximately 5m (up from ~ 4m).

Figure 5.13 shows the results again for the case of an installed controller for the flapping and TEF response to a step input in rotor speed but with extended time history to show the stabilised response.

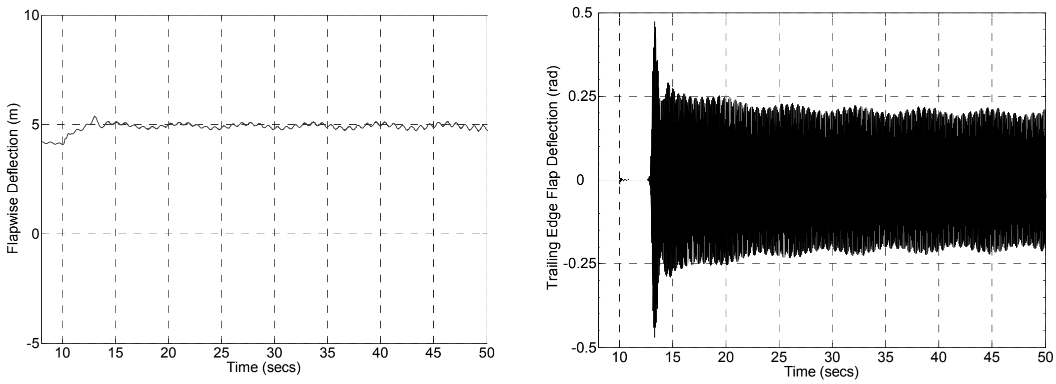

Figure 5.13 Expanded Time History for Flap (left) & TEF (right) Response to a Step Input on Rotor Speed

The TEF has a maximum deflection of approximately 23 degrees, reaching an equilibrium oscillatory amplitude of about 10 degrees. This experiment shows a positive result for stabilising the response of the turbine which has entered a Flutter zone using TEFs.

The same controller is now applied for the case of increasing rotor speed to and beyond the Flutter point. The results are given in Figure 5.14 overleaf.

The Flutter speed of the modified blade with no controller is approximately reached at $66ms^{-1}$, at which sudden amplitude growth in torsion and flap occurs causing the simulation to fail. With the controller in place, it is shown the Flutter limit is increased as it is being suppressed, but in this case, the system is slowing growing in amplitude, with the TEF unable to reach equilibrium. This could be caused by a few reasons; one being that the system is always slowly accelerating in rotor speed, meaning the systems dynamics are shifting away from that which the controller was designed for. Another reason may be due to an edgewise instability which seemed to be more pronounced as the rotor speed increased far beyond the normal operation speed. It should be remembered that this test case uses altered blade properties, so the dynamics of the blade may not behave as expected, especially at higher than intended rotor speeds, so large edgewise deflections might be expected.

The larger edgewise deflections show through to the coupled torsion and flap response by the increasing amplitude shown in the right side of Figure 5.14. Therefore it could be possible that without the edgewise instability, the controller may keep the system from slowly increasing in amplitude. To verify this problem, a simulation was carried out so that the rotor speed became constant at some point within the Flutter zone, rather than continuing to increase. The effect was that the system showed more stability, but still a very slowly building edgewise instability resulted. The conclusion therefore is that while Flutter is suppressed, other dynamics are interfering with the control of the wind turbine dynamics stabilising.

In any event, the result still shows an extension of the Flutter boundary well beyond that without the controller and gives enough evidence to suggest a more complex, thoroughly designed controller with an optimised controller and TEF flap assembly is a suitable means to mitigate against Classical Flutter instability problems on wind turbines.

<table>
<tr><th>No Controller</th><th>Installed Controller</th></tr>
<tr><td>Torsion Deflection up to Flutter Speed</td><td>Torsion Deflection Beyond Flutter Speed</td></tr>
<tr><td>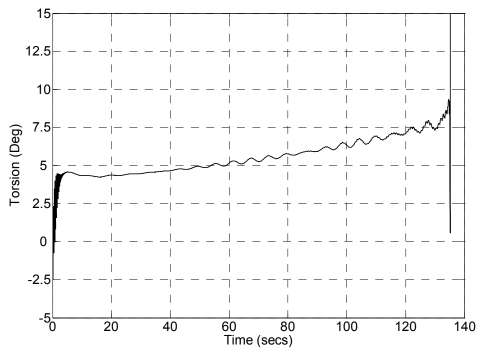
</td><td>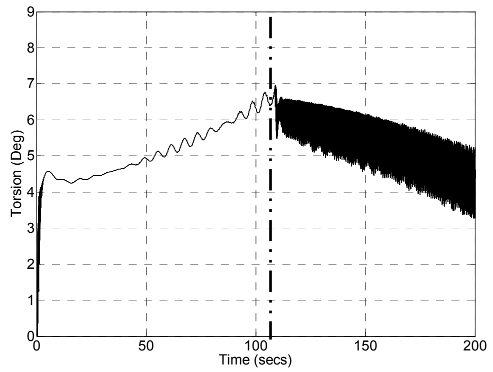
</td></tr>
<tr><td>Flapwise Deflection up to Flutter Speed</td><td>Flapwise Deflection Beyond Flutter Speed</td></tr>
<tr><td>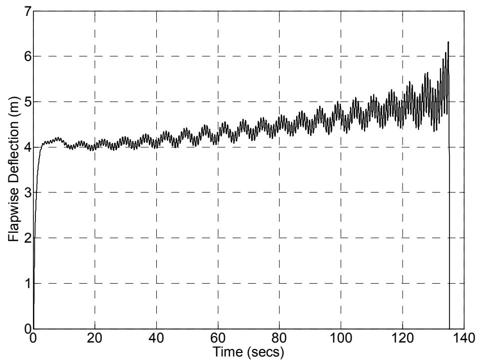
</td><td>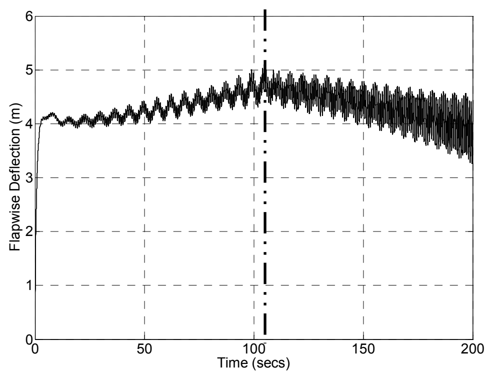
</td></tr>
<tr><td>Increasing Rotor Speed - Original Flutter Speed (horizontal dashed line)</td><td>Trailing Edge Flap Response to Flutter</td></tr>
<tr><td>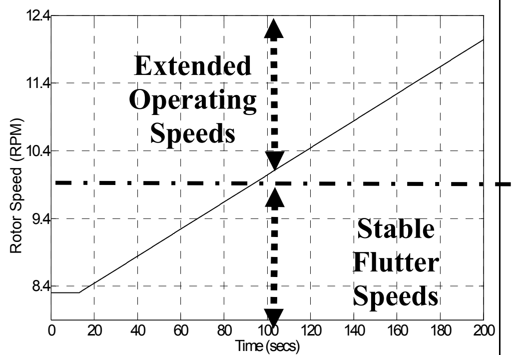
</td><td>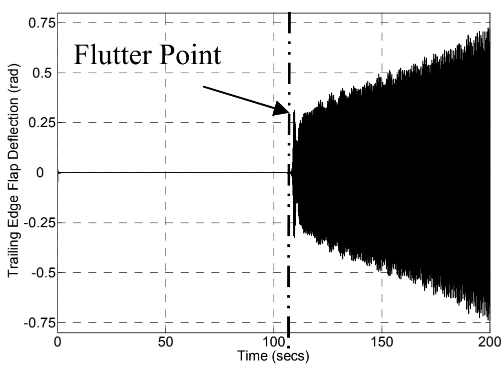
</td></tr>
</table>

Figure 5.14 Induced Flutter and Control for Ramp Up of Rotor Speed

5.4 Limitations of the TEF Analysis

The analysis just undertaken should be considered as 'raw' only and much more work needs to be done to show how a TEF could be used over the whole wind turbine operational envelope as a stability shaping device. The time available for this study only allowed a very simplified single-input-single-output (SISO) controller to be designed and this in itself presented some limitations in the amount of control the system could achieve as indicated by the results in Figure 5.14. It is possible this SISO system identification led to a system containing right-half plane zeros (from root locus plots), making it difficult to design a stable controller for the system. A multiple-input-multiple-output (MIMO) control identification procedure should enable better control to be obtained through monitoring more system variables and using them in feedback. Although the results show an extension of the Flutter operating limits, the controller is far from optimised, both in actuator design and TEF geometry. For an optimised TEF control surface covering optimum blade span and using the right chord ratio requires the structural response (deformation) of the TEF to be included with the blade.

It is therefore strongly recommended for any subsequent analysis to work with MIMO systems at a minimum with detailed control system phenomena applied to the actuator to make the analysis more practical and realistic. This means careful attention should be paid to maximum TEF deflection and frequency bandwidths.

The author can recommend the material presented in Verhaegen and Verdult [31] for an introduction into MIMO system analysis as could be applied in an extension to the present study.

Further recommendations on improving the TEF analysis is given in section 6.

6 Conclusions & Recommendations

Conclusions

In the preceding sections of this analysis, the following items have been addressed in terms of fulfilling the goals and objectives initially set out to investigate the feasibility of using trailing edge flaps to mitigate against the Classical Flutter instability:

- A simplified aeroelastic model comprising of a modal analsysis and BEM theory module has been developed for determination of the forces and response of the rotor. The equations of motion are represented through the generalised coordinate method and virtual work principle for a discretised beam. The aerofoil with added trailing edge flap (TEF) geometry incorporates Theodorsen's theory for determining the lift coefficient for arbitrary aerofoil and TEF deflections.
- A rigid tower, one-bladed version of the 5MW UpWind turbine (122m diameter), with all blade sectional properties and operating characteristics as prescribed, has been investigated for the boundaries (limiting operational tips speeds) of its instability limits for Classical Flutter.
- A fictitious 10MW (172m diameter) wind turbine design was scaled from the 5MW design to compare the effects of wind turbine up-scaling on the Flutter limits. Basic scaling rules were used with the assumption of larger blades becoming more slender to avoid them being high in mass. Similar operating tip speed ratios were assumed for normal mode of operation.
- A solution to the Classical Flutter problem was then demonstrated through the development of a TEF actuator controller and for a given flap geometry assembly. A simple controller with PID capability (single input-output) was tested using the practically measured-in real life-blade tip accelerations to monitor the state of the system. For the purposes of the experiment, the upwind blade was modified in stiffness and centre of gravity location so that the Flutter velocity could be reached more quickly.

In regards to the 5MW UpWind turbine, the following was found in regards to the Flutter limit investigation:

- At low wind speeds the Flutter limit was reached at rotor speeds around 21RPM (tip speeds ~ 120ms^{-1}). At the other end of the wind speed spectrum, Flutter was exhibited at around 17RPM (tip speeds ~ 107ms^{-1}). This lower limit is still well above the maximum rotor speed of 12.5RPM (tip speeds ~ 80ms^{-1}) for which the 5MW wind turbine operation is intended. It is therefore unlikely such a turbine could be put into the state of a Flutter mode in normal operation.
- A spectral analysis of the wind turbine state close to a Flutter mode revealed it was likely the 2nd flapwise blade mode responsible for interacting with torsion to cause Flutter. This has been the case for other studies with similar blade properties and length. For the UpWind turbine at the operation condition tested, the Flutter mode took place between 3Hz and 4Hz.
- Wind Shear and Tower Shadow effects seemed to lower the Flutter limits. This was thought to occur due to the excitation they provide as the Flutter instability limit is being approached.
- Finally, as also observed in other studies, the location of the centre of gravity relative to the shear centre has impacts on the observed Flutter limit. Placing the centre of gravity forward of the shear centre (from a position of 10% of the chord behind it) increased the Flutter limit from around 113ms^{-1} to 125ms^{-1}, an increase of 10%.

The up-scaled wind turbine of 10MW showed stiffness values quite reduced compared to the 5MW blade. The torsion frequency of the blade reduced from 5.6Hz to 4Hz, while the 2nd flapwise frequency reduced from 2.3Hz to 1.25Hz. This shows a relative closing in the gap between the two frequencies and therefore possibly a lower Flutter limit speed. When the limits were investigated, the following was found:

- For low wind speeds, a much reduced tip speed Flutter velocity of 72ms^{-1} was discovered (120ms^{-1} for 5MW case for same condition).
- For higher wind speeds, the wind turbine exhibited Flutter modes and was difficult to get to a stable condition. Even at a greatly reduced tip speeds, Flutter was still possible for wind speeds around the operating limits of 25ms^{-1}.

The conclusion drawn from the comparison is that wind turbines approaching 10MW and beyond will need careful design using full aeroelastic analyses if Flutter is to be avoided without using alternative means, such as the smart rotor concept.

Finally, it was shown that implementing trailing edge flaps does have the potential to stabilise against the Classical Flutter effect. For a given trailing edge flap span and chord width, it was possible to show the modified wind turbine entering into a Flutter mode and being stabilised by trailing edge flap deflection frequencies of 20Hz and angles around 13 degrees. For one scenario in particular, it was shown the wind turbine was still stabilised for an increase in rotor speed of 3RPM beyond its original Flutter limit.

Recommendations

The results presented for the performance of TEFs as a stability shaping device have been positive in the theoretical sense, and in the author's opinion, warrants more investigation into their feasibility for future wind turbine designs. The current study has used quite a simplified analysis and leaves room for more rigorous testing of TEFs. The areas needing further work can be split into two categories; that dealing with the aeroelastic model and that which deals with an optimised controller-TEF flap assembly. Some points to consider in any subsequent analysis are given below:

Aeroelastic Model

- The aeroelastic model should be expanded to include the whole turbine structure, such as drive train and tower dynamics. This includes modelling 3 blades, rotor coning and tilt. Hansen [8] has shown the dynamics of the whole turbine structure influence the Flutter limits.
- The BEM model needs to be upgraded such that induction is determined using the annular method. Currently the induction factor is assumed constant over the rotor disc.
- Unsteady Drag and Moment coefficients could be included in Theodorsen's model, since for this study they were estimated for steady values from the blades look-up tables. It might even be prudent to consider a complex CFD model so that full geometry of aerofoil and trailing edge flap can be modelled as opposed to the flat plat representation.
- A pitch controller could also be installed to simulate the effects this could have with Flutter, as this could excite the Flutter mode if close enough to it.
- Mechanical damping should be added to the structure, particularly to give more stable simulation results around rated wind speed where there is a high speed-torque slope.
- A dynamic stall module could be installed such that it is possible to model more instabilities, e.g. stall Flutter, and test stability using trailing edge flaps.
- More testing on Flutter effects with all three of turbulence, tower shadow and wind shear included.

Trailing Edge Flap Geometry & Controller

- Trailing edge flap dynamics needs to be included with blade dynamics, i.e. need to model TEF deformation relative to aerofoil due to inertia and elastic forces. This will give a more realistic description of the aerodynamics on the blade and allow optimised design of flap surface. A more detailed analysis needs to be made on where the resulting forces and moments are produced with a TEF, as these may impact on controllability.
- More focus on the realistic simulation of a type of actuator with specific mechanical properties to give realistic output for magnitudes of flap angles and frequency for practical Flutter suppression.
- More analysis on the optimum span and chord width of TEF for maximum load control and minimum actuator power.
- Incorporate more complex controller techniques, such as multiple-input-output controllers. This might make for better control over the Flutter instability which was a limiting factor in this analysis.

It would be considered worth while in the future to focus on the trailing edge flap aerodynamics and actuator dynamics. It needs to become apparent that there are practical devices available that can reliably produce the frequencies and flap angles required to change the response and suppress Flutter.

References

[1]. Bielawa, R.L. (1992), *Rotary Wing Structural Dynamics and Aeroelasticity*, AIAA Education Series.

[2]. Borglund, D. & Kuttenkeuler, J. (2002), Active Wing Flutter Suppression Using a Trailing Edge Flap, Journal of Fluids and Structures, Vol. 16(3), 271-294.

[3]. Burton T, Sharpe, D, Jenkins, N, & Bossanyi, E. (2001), *Wind Energy Handbook,* John Wiley & Sons, England.

[4]. Clough, R.W. (1975), *Dynamics of Structures*, McGraw-Hill.

[5]. Chaviaropoulos, P.K. (1999), Flap-Lag Aeroelastic Stability of Wind turbine Blade Sections, Wind Energy, Vol. 2, 99-112.

[6]. Gaunaa, M, (n.d), 'Investigation of the Effect of Deformable Trailing Edge Geometry Control systems on Flutter Velocity", Riso National Laboratory.

[7]. Glauert, H., (1963), Airplane Propellers, Aerodynamic Theory, W. F. Durand, ed., Dover, New York.

[8]. Hansen, M.H.(2002), Vibrations of a Three-Bladed Wind Turbine Rotor due to Classical Flutter. AIAA, A02-14513 (48), 256-66.

[9]. Hansen, M.H. (2007), Aeroelastic Instability Problems for Wind Turbines, von Karmen Institute for Fluid Dynamics, Lecture Series 2007-05.

[10]. Hansen, M.O.L., Sorensen, J.N., Voutsinas, S., Sorensen, N. & Madsen, H.Aa (2006), Elsevier, Progress in Aerospace Sciences 42, 285-330.

[11]. Hansen, M.O.L (n.d), "*Simulation of dynamic systems"*, Course Notes, Denmark.

[12]. Hansen, O.L. M. & Sorensen, J.N. (n.d), "*Unsteady BEM Model"*, Course Notes, Denmark.

[13]. Honlinger, H.G., Krammer, J. & Stettner, M. (1998), MDO Technology Needs in Aeroelastic Structural Design, American Institute of Aeronautics and Astronautices, AIAA-984731.

[14]. Hulshof, S.J. (2007), "*Aeroelasticity",* Course Notes, TUDelft.

[15]. Hansen, M.H (2003). *Aerodynamics of Wind Turbines*, James & James Ltd.

[16]. Leishman, J.G. (2002), Challenges in Modelling the Unsteady Aerodynamics of Wind Turbines, Wind Energy, Vol 5, 85-132.

[17]. Leishman, J.G. (1994). Unsteady Lift of a Flapped Airfoil by Indicial Concepts. AIAA, Vol. 31, No. 2, 288-296.

[18]. Manwell, J.F., McGowan J.G. & Rogers, A.L. (2002), *Wind Energy Explained,* John Wiley & Sons.

[19]. Marrant, B. (2007), WIMSIM – Wind Turbine Integrated Module Simulation for Simulink, Aerospace Engineering, TUDelft Internal document.

[20]. Gere, J.M. & Timoshenko, S.P. (1999), *Mechanics of Materials*, Fourth edition, Stanley thornes (publishers) Ltd.

[21]. Van Holten, Th. (2006), Energy Flow Considerations, An Educational Tool to Clarify Aeroelastic Phenomena, Conference Paper, TUDelft.

[22]. Van Holten, Pavel, M.D. & Smits, G.N., The Influence of Scale Effects on the Aeroelastic Stability of Large Wind Turbines, Faculty of Aerospace Engineering, Delft University of Technology, Delft.

[23]. Pavel, M.D. (1999), *An investigation of the Rotor-Tower Instability of the KEWT Wind Turbine*, TUDelft, Novem project no 224.740-9854.

[24]. Pavel, M.D. & Schoones, M.M.J. (1999), *Literature survey on Aeromechanical Instabilities for helicopters and wind turbines*, TUDelft, Novem project no. 224.740-9854.

[25]. Rasmussen, F. Hansen, M.H, Thomsen, K, Larsen, T.J, Bertagnolio, F., Johansen, J., Madsen, H.A., Bak, C. & Hansen, A.M. (2003), Present Status of Aeroelasticity of Wind Turbines, Wind Energy, Vol 6, 213-228.

[26]. Stepniewski, W.Z. (1981), *Rotary Wing Aerodynamics*, Dover Publications.

[27]. Tangler, J.L, (2000), The Evolution of Rotor and Blade Design, Presented at the American Wind Energy Association, NREL, Colorado.

[28]. Van den Hof, P.M.J (2004), *System Identification*, Delft Centre for Systems and Control, Delft.

[29]. Van Langen, P.J. (2007), Aeroleastic Analysis of the UpWind reference wind turbine (Draft), ECN, ECN-E-07-000

[30]. Veldkamp, D., *Oral discussion on Generalised Forces for Pure Torsion of a Blade*, TUDelft.

[31]. Verhaegan, M. & Verdult, V. (2007), Filtering and System Identification: An Introduction, Cambridge Univ Pr.

[32]. Quarton D.C. (1998), The Evolution of Wind Turbine Design Analysis – A Twenty Year Progress Review, Wind Energy, Vol. 1, 5-24.

Appendix

A.I WIMSIM Aerodynamic Model and Validation

In this chapter, the Aerodynamic module of Theodorsen adapted with the Wagner and Kussner functions as used in the WIMSIM aeroelastic model is given in detail. The equations for Theodorsen representing a flat plate aerofoil with state space representation are taken from the paper of Leishman [16]. The BEM module was created internally within TUDelft and an internal document describing the following structure was constructed by Marrant [17]. The aerodynamics module makes use of the classic blade element momentum method together with the extended Theodorsen model for general motions to describe the unsteady aerodynamics with a trailing edge flap, and including a dynamic inflow model.

A.I.I Blade Element Momentum Method (BEM)

The aerodynamic forces can be calculated using classic BEM theory. This requires equating the axial aerodynamic force on the rotor as determined with momentum theory and blade element theory in order to find the steady axial induction factor which determines the strength of the wake. For these calculations the rotation in the wake has been neglected and it was assumed that the axial induction factor is constant over the rotor disc, this means that a mean value of the wake is taken. With the use of momentum theory the axial induction factor can be found for the normal windmill state:

I.1

$$C_{Dax} = 4a\left|1-a\right|$$

and an empirical relation is used for the turbulent wake state:

I.2

$$C_{Dax} = \frac{2.7077}{1.991-a} \quad 0.5 \le a \le 1.62$$

where:

$C_{D\,ax}$: is the axial aerodynamic force coefficient [-],

a: is the axial induction factor [-].

A blade element with the definitions of velocities, angles, forces and moments can be seen in Figure I.1. From this the blade element theory can be described.

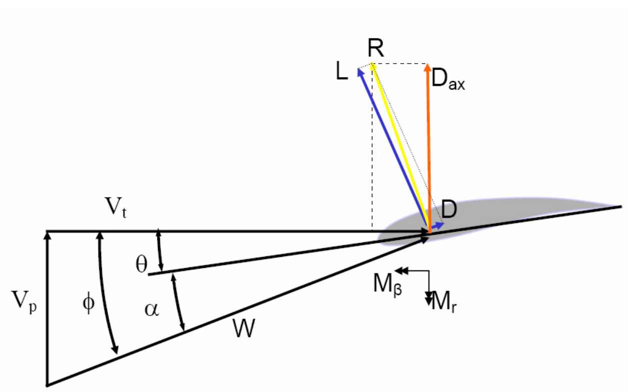

Figure I.1 Blade section with definitions of velocities, angles, forces and moments

The perpendicular velocity component is equal to:

I.3

$$V_p = V(1-a)$$

where:

V mean wind speed in [m/s],

a: steady axial induction factor [-]

The tangential velocity component is equal to:

I.4

$$V_t = \Omega r$$

where:

Ω : angular velocity of the rotor [rad/s],

r: radius of the blade element [m]

The relative wind speed at each blade element is determined with:

I.5

$$W = \sqrt{V_p^2 + V_t^2}$$

The inflow angle of each blade element is equal to:

I.6

$$\varphi = a\tan\left(\frac{V_p}{V_t}\right)$$

The total lift and the drag of each blade can be determined by integrating the incremental lift and drag of over the entire blade radius:

I.7

$$L = \int_0^R c_l \frac{1}{2}\rho W^2 c\, dr$$

$$D = \int_0^R c_d \frac{1}{2}\rho W^2 c\, dr$$

where:

c_l : lift coefficient [-],

ρ: air density [kg/m^3],

c: chord length [m],

dr: length of a blade element [m].

The lift coefficients are determined with the use of Theodorsen and the Küssner and Wagner function with Duhamel superposition as described in the section on unsteady aerodynamics. The drag coefficients are determined from look-up tables where c_d is given as a function of the quasi-steady airfoil angle of attack α. These drag coefficients originate from steady airfoil data for the blade section at 75% radius.

In Figure I.1 it can be seen that the axial aerodynamic force induced by the rotor is determined by summing the lift and drag components of all blades in the axial direction:

I.8

$$D_{ax} = \sum_{n=1}^{N_b} \left(\int_0^R dL \cos(\varphi) + \int_0^R dD \sin(\varphi) \right)$$

The non-dimensional axial aerodynamic force coefficient is then determined with:

I.9

$$C_{Dax} = \frac{D_{ax}}{1/2 \rho V^2 \pi R^2}$$

The aerodynamic flapping moment is determined by summing the moments due to the lift and drag components of each blade element in the axial direction as can be seen in Figure I.1:

I.10

$$M_\beta = \int_0^R r \cos(\varphi) dL + \int_0^R r \sin(\varphi) dD$$

The aerodynamic rotor torque is determined by the summation of the moments due to the lift and drag components of each blade element in the direction of the rotor plane:

I.11

$$M_r = k_p \int_0^R r \sin(\varphi) dL - \int_0^R r \cos(\varphi) dD$$

where k_p is the power loss factor, a correction factor for the simplifications made within BEM theory, which is equal to 0.9.

The steady aerodynamic axial force, blade flapping moment and torque are within a range of 1% difference with respect to the original calculated values with the Matlab version of WIMSIM.

A.I.II Unsteady Aerofoil Aerodynamics

Unsteady airfoil aerodynamics has been described in the work by Theodorsen and made suitable for general inputs in the time domain by Wagner and Küssner [16].

The unsteady lift coefficient consists of two parts, one describing the non-circulatory part of the flow and the other describing the circulatory part of the flow.

I.12

$$c_l = c_{l,nc} + c_{l,c}$$

The non-circulatory lift coefficient determined by Theodorsen is given by:

I.13

$$c_{l,nc} = -\frac{\pi c}{2W^2} \left(r \ddot{\beta} + W \dot{\theta} + \frac{\Omega}{W} \dot{\Omega} r^2 \alpha_{qs} + \frac{c \ddot{\theta}}{4} \right) - \frac{c}{2W^2} \left(F_4 W \dot{\delta} + \frac{c F_1 \ddot{\delta}}{2} \right)$$

with the coefficients F_1 and F_4 according to Theodorsen:

I.14

$$F_1 = e \cos^{-1} e - \frac{1}{3}\left(2 + e^2\right)\sqrt{1 - e^2}$$

$$F_4 = e\sqrt{1 - e^2} - \cos^{-1} e$$

where:

α_{qs}: quasi-steady angle of attack due to a pitch and plunge motion [rad],

δ: trailing-edge flap deflection [rad],

θ: blade pitch angle (rotation around the ¼ chord point) [deg],

e: non-dimensional trailing-edge flap hinge location in semi-chords [-],

W: relative wind speed [m/s],

dot=d/dt: first time derivative [1/s].

The blade with the trailing-edge flap and the definitions according to Theodorsen can be seen in Figure I.2.

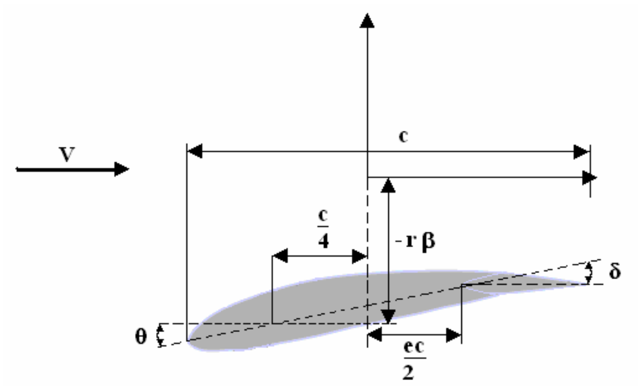

Figure I.2 Blade section with trailing-edge flap and dimensions and angles for Theodorsen's theory

For arbitrary airfoil and trailing-edge flap motion and for the case where the airfoil is operating in an arbitrary gust field, the circulatory part of the lift coefficient can be obtained by means of Duhamel's superposition integral with the Wagner indicial step response ϕ and the Küssner gust entry function Ψ:

I.15

$$c_{l,c} = (c_{l,c})_{\alpha} + (c_{l,c})_{\delta} + (c_{l,c})_{w_g}$$

$$2\pi\left(\alpha_{qs}(0)\phi(s) + \frac{1}{V}\int_0^s \frac{d(V\alpha_{qs})}{d\sigma}\phi(s-\sigma)d\sigma + \delta_{qs}(0)\phi(s) + \int_0^s \frac{d\delta_{qs}}{d\sigma}\phi(s-\sigma)d\sigma + \frac{w_g(0)}{W}\Psi(s)\right.$$
$$\left. + \int_0^s \frac{dw_g}{d\sigma}\Psi(s-\sigma)d\sigma\right)$$

where:

s: non-dimensional aerodynamic time [-],

w_g: downwash velocity [m/s],

δ_{qs}: quasi-steady angle of attack due to a trailing-edge flap deflection [rad],

ϕ: Wagner function,

Ψ: Küssner function.

In these, the quasi-steady angle of attack α_{qs} and the quasi-steady angle of attack due to trailing-edge flap deflection δ_{qs} are given with respect to the initial steady state values. The non-dimensional parameter s is the aerodynamic time based on semi-chord lengths of the airfoil traveled:

I.16

$$s = \frac{W}{(c/2)}$$

The quasi-steady airfoil angle of attack is equal to:

I.17

$$\alpha_{qs} = \varphi + \Delta\varphi - \left(\theta + \theta_i + \frac{\dot{\theta}\, c}{2W} + \frac{\dot{\beta}\, r + \dot{x}}{W} \right)$$

where:

β: blade flapping angle [rad],

φ: inflow angle [rad],

θ_i: local twist angle of the blade [deg],

x: tower displacement [m].

The increment in inflow angle $\Delta\varphi$ is:

$$\Delta\varphi = a\tan\left(\frac{V}{\Omega r} \right) - a\tan\left(\frac{V}{\Omega_0 r} \right)$$

where:

Ω_0: steady rotor speed

Ω: instantaneous rotor speed

The quasi-steady angle of attack due to a trailing-edge flap deflection can be written as:

I.18

$$\delta_{qs} = \frac{F_{10}\,\delta}{\pi} + \frac{c\,F_{11}\,\dot{\delta}}{4\pi W}$$

with the coefficients F_{10} and F_{11} according to Theodorsen.

I.19

$$F_{10} = \sqrt{1-e^2} + \cos^{-1} e$$
$$F_{11} = (1-2e)\cos^{-1} e + (2-e)\sqrt{1-e^2}$$

The quasi-steady angle of attack due to a trailing-edge flap deflection is only taken into account for the blade sections at the tip where the trailing-edge flap is located. For the simulations the inboard location of the flap must be specified in the wind turbine file. The outboard location is assumed to be the tip. A trailing-edge flap located near the tip will be the most efficient because of the larger moment arm.

The Wagner function $\phi(s)$ describing the unsteady aerodynamic behavior of the airfoil, due to a step change in the angle of attack or a step change in trailing-edge flap deflection, can be approximated by the indicial step response function with an error of less than 0.1%:

I.20

$$\phi(s) = 1.0 - A_1 e^{-b_1 s} - A_2 e^{-b_2 s}$$

where $A_1=0.2048$, $A_2=0.2952$, $b_1=0.0557$ and $b_2=0.333$.

The Küssner function $\Psi(s)$ describing the unsteady aerodynamic behavior of the airfoil in an arbitrary gust field can be approximated by the indicial function with an error of less than 0.1%:

I.21

$$\Psi(s) = 1 - A_3 e^{-b_3 s} - A_4 e^{-b_4 s}$$

where $A_3=0.5792$, $A_4=0.4208$, $b_3=0.1393$ and $b_4=1.802$.

The state space equivalent of the Duhamel integral can be written as:

I.22

$$\begin{Bmatrix} \dot{z}_1 \\ \dot{z}_2 \\ \dot{z}_3 \\ \dot{z}_4 \end{Bmatrix} = \begin{bmatrix} 0 & 1 & 0 & 0 \\ -b_1 b_2 \left(\frac{2W}{c}\right)^2 & -(b_1+b_2)\left(\frac{2W}{c}\right) & 0 & 0 \\ 0 & 0 & 0 & 1 \\ 0 & 0 & -b_3 b_4 \left(\frac{2W}{c}\right)^2 & -(b_3+b_4)\left(\frac{2W}{c}\right) \end{bmatrix} \begin{Bmatrix} z_1 \\ z_2 \\ z_3 \\ z_4 \end{Bmatrix} + \begin{bmatrix} 0 & 0 \\ 1 & 0 \\ 0 & 0 \\ 0 & 1 \end{bmatrix} \begin{Bmatrix} \alpha_{qs} + \delta_{qs} \\ \frac{w_g}{W} \end{Bmatrix}$$

$$c_{l,c} = c_{l,\alpha} \begin{bmatrix} \frac{b_1 b_2}{2}\left(\frac{2W}{c}\right)^2 & (A_1 b_1 + A_2 b_2)\left(\frac{2W}{c}\right) & b_3 b_4 \left(\frac{2W}{c}\right)^2 & (A_3 b_3 + A_4 b_4)\left(\frac{2W}{c}\right) \end{bmatrix} \begin{Bmatrix} z_1 \\ z_2 \\ z_3 \\ z_4 \end{Bmatrix} + \frac{c_{l,\alpha}}{2}\left\{\alpha_{qs} + \delta_{qs}\right\}$$

or

$$\begin{Bmatrix} \dot{z}_1 \\ \dot{z}_2 \\ \dot{z}_3 \\ \dot{z}_4 \end{Bmatrix} = [A]_i \begin{Bmatrix} z_1 \\ z_2 \\ z_3 \\ z_4 \end{Bmatrix} + [B]_i \begin{Bmatrix} \alpha_{qs} + \delta_{qs} \\ \frac{w_g}{W} \end{Bmatrix}$$

$$c_{l,c} = c_{l,\alpha}[C]_i \begin{Bmatrix} z_1 \\ z_2 \\ z_3 \\ z_4 \end{Bmatrix} + \frac{c_{l,\alpha}}{2}\left\{\alpha_{qs} + \delta_{qs}\right\}$$

For all the blade elements together the state space system looks as follows:

$$\{\dot{z}\} = \begin{bmatrix} A_1 & 0 & \dots & 0 \\ 0 & A_2 & \dots & 0 \\ \vdots & \vdots & \ddots & \vdots \\ 0 & 0 & \cdots & A_{N_b N_s} \end{bmatrix} \{z\} + \begin{bmatrix} B_1 & 0 & \cdots & 0 \\ 0 & B_2 & \cdots & 0 \\ \vdots & \vdots & \ddots & \vdots \\ 0 & 0 & \cdots & B_{N_s N_b} \end{bmatrix} \{y\}$$

$$\{c_{l,c}\} = c_{l,\alpha}\begin{bmatrix} C_1 & 0 & \cdots & 0 \\ 0 & C_2 & \cdots & 0 \\ \vdots & \vdots & \ddots & \vdots \\ 0 & 0 & \cdots & C_{N_sN_b} \end{bmatrix}\{z\} + \begin{bmatrix} \begin{bmatrix} 0 & \frac{c_{l,\alpha}}{2} \end{bmatrix} & 0 & \cdots & 0 \\ 0 & \begin{bmatrix} 0 & \frac{c_{l,\alpha}}{2} \end{bmatrix} & \cdots & 0 \\ \vdots & \vdots & \ddots & \vdots \\ 0 & 0 & \cdots & \begin{bmatrix} 0 & \frac{c_{l,\alpha}}{2} \end{bmatrix} \end{bmatrix}\{y\}$$

where the matrices A_i, B_i , C_i for each blade element i are defined in the previous equations and the input vector $\{y\}$ is defined as:

I.23

$$\{y\} = \left(\left(\alpha_{qs} - \alpha_{qs,0} + \delta_{qs} - \delta_{qs,0}\right)_1 \quad \left(\frac{w_g}{W}\right)_2 \quad \cdots \quad \left(\alpha_{qs} - \alpha_{qs,0} + \delta_{qs} - \delta_{qs,0}\right)_{N_sN_b} \quad \left(\frac{w_g}{W}\right)_{N_sN_b} \right)^T$$

A.I.III Validation of Unsteady Aerodynamic Module

The state space module implemented in WIMSIM was tested under some specific conditions to validate the solution using the aforementioned theory.

Figure I.3 a) and Figure I.3 b) show a step response in pitch on the aerodynamic flapping moment in uniform wind flow.

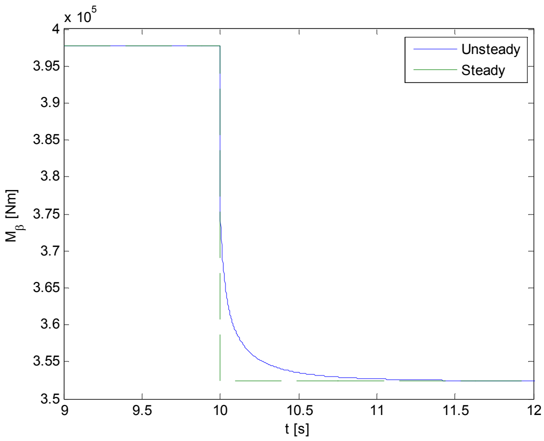

a)

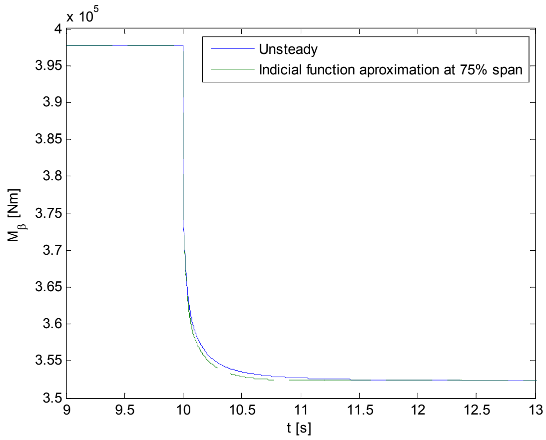

b)

Figure I.3 Step response in pitch on the aerodynamic flapping moment of a blade, a) Comparison between steady and unsteady aerodynamic model, b) Comparison of unsteady aerodynamic model with scaled indicial Wagner function at 75% span

In Figure I.3 a) a comparison is made between the aerodynamic flapping moment obtained with steady and unsteady aerodynamics, it can be seen that the unsteady response converges to the steady step response. In Figure I.3 b) the unsteady step response is compared with the scaled indicial Wagner function for the 75% span location. It can be seen that the correlation between the two is very good which indicates the validity of the computations. It can be clearly seen that a positive pitch input gives a decrease in the aerodynamic flapping moment because of the smaller angle of attack. For this specific situation it takes approximately 1.1 seconds or approximately 150 degrees before the aerodynamic moment reaches its new steady state.

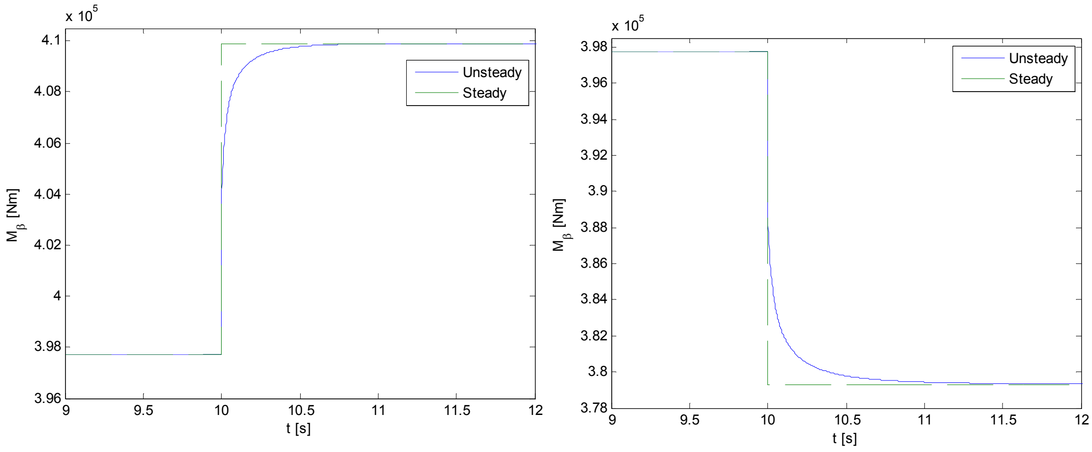

a) **b)**

Figure I.4 a) Step response in trailing-edge flap deflection on the blade aerodynamic flapping moment, b) step response in blade flapping on the aerodynamic flapping moment

In Figure I.4 a) a step response in trailing-edge flap deflection is shown whereas in Figure I.4 b) a step response in blade flapping is shown. In both cases the unsteady aerodynamic flapping moment converges to the steady flapping moment. As shown in Figure I.4 a) a positive trailing-edge flap deflection results in an increase in aerodynamic flapping moment. As shown in Figure I.4 b) a positive blade flapping rate gives a decrease in aerodynamic moment since this blade flapping results in aerodynamic damping of the flapping motion.

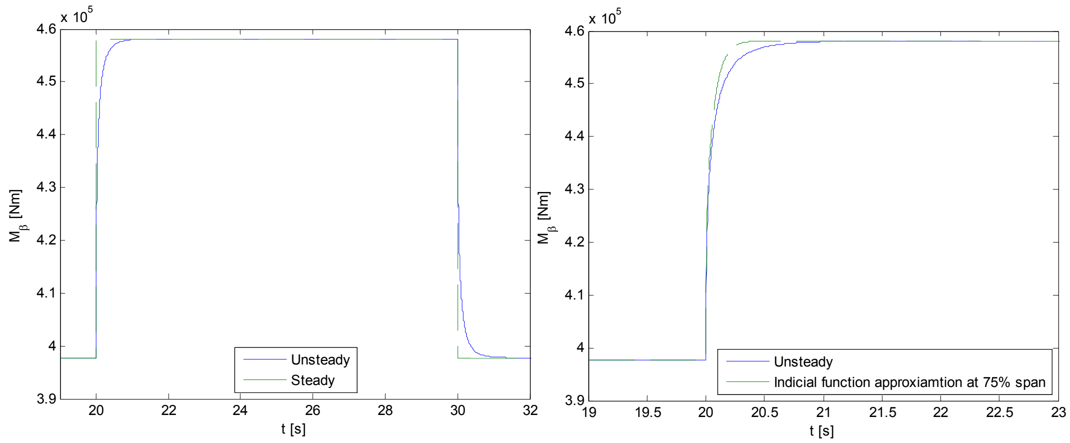

a) **b)**

Figure I.5 Aerodynamic blade flapping response on a gust in the form of a single pulse, a) Comparison of steady and unsteady aerodynamic model, b) Comparison of unsteady model and scaled Küssner function

The influence of a gust input in the form of a single pulse can be seen in Figure I.5 a) for both the steady and the unsteady aerodynamic model. It can be seen that the unsteady response converges to the steady response within approximately 1 second. Figure I.5 b) shows the comparison of the scaled indicial Küssner function at the 75% span location. Here the comparison is not as good as for the Wagner function.

A.I.IV Dynamic Inflow

The dynamic behavior of the wake is described with a first order differential equation with respect to the time. Also here the distinction is made between the normal windmill state:

I.24

$$\dot{a} = \frac{V}{4R}\left(-a + 0.5 - 0.5\sqrt{1 - C_{Dax}}\right) \text{ for } C_{Dax} \leq 1.0$$

and the turbulent wake state:

I.25

$$\dot{a} = \frac{V}{4R}\left(-a + 1.991 - \frac{2.7077}{C_{Dax}}\right) \text{ for } C_{Dax} \geq 1.0$$

where R is the radius of the blade.

The dynamic inflow effect can be seen in Figure I.6 in the comparison of a step response in pitch for the aerodynamic flapping moment for the situation with dynamic inflow and the situation where the wake adapts itself instantaneously to the step input in blade pitch. The dynamic inflow can be seen as the undershoot of the aerodynamic flapping moment with respect to the other situation followed by the increase of the aerodynamic flapping moment until it converges to the aerodynamic flapping moment obtained with an instantaneously adapting wake. The dynamic inflow effect refers to the fact that the wake needs time to accommodate to a new equilibrium situation. This figure also shows the unsteady aerodynamic effect due to blade pitching (Wagner) which is clearly much less severe than the dynamic inflow effect. For both cases the inflow changes necessitating the use of Küssner.

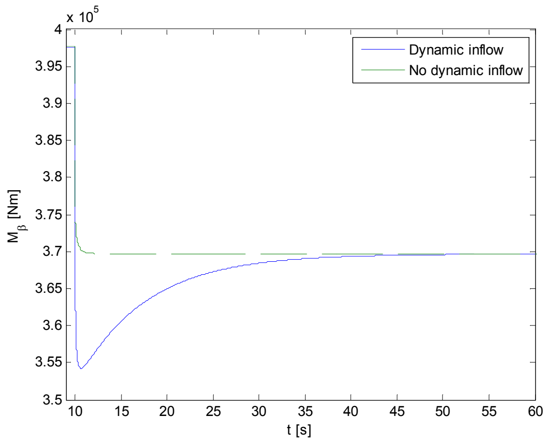

Figure I.6 Comparison of a first order dynamic inflow model with an instantaneously changing wake model for a step response in blade pitch

A.II Upwind Turbine Operating & Blade Specifications

A.II.I Upwind Operating Characteristics

Wind Speed (ms-1)	RPM	Pitch (Deg)
5	7.0	0
6	8.0	0
7	8.5	0
8	10.0	0
9	11.5	0
10	12.5	3
11	12.7	3
12	12.7	6
13	12.7	6.5
14	12.7	8
15	12.7	10.5
16	12.7	11.5
17	12.7	14
18	12.7	14.9
19	12.7	16
20	12.7	17
21	12.7	18.5
22	12.7	19
23	12.7	19.8
24	12.7	22.1
25	12.7	23.3

A.II.II Upwind Blade Structural Data

The following tables provide the blade structural and eigenmode data and used in the current investigation. The blade node points at which deflections, velocities, etc are determined in the simulations are given in the 1st column of each table.

Other relevant data specified in the table can also be view in the following diagram, which illustrates the assumed position of the springs and various variable offsets. The z' and y' axis indicates the principle axis of the blade. The elastic axis EA is the origin of this axis and is not a fixed distance from the aerofoil leading edge, i.e. changes with span.

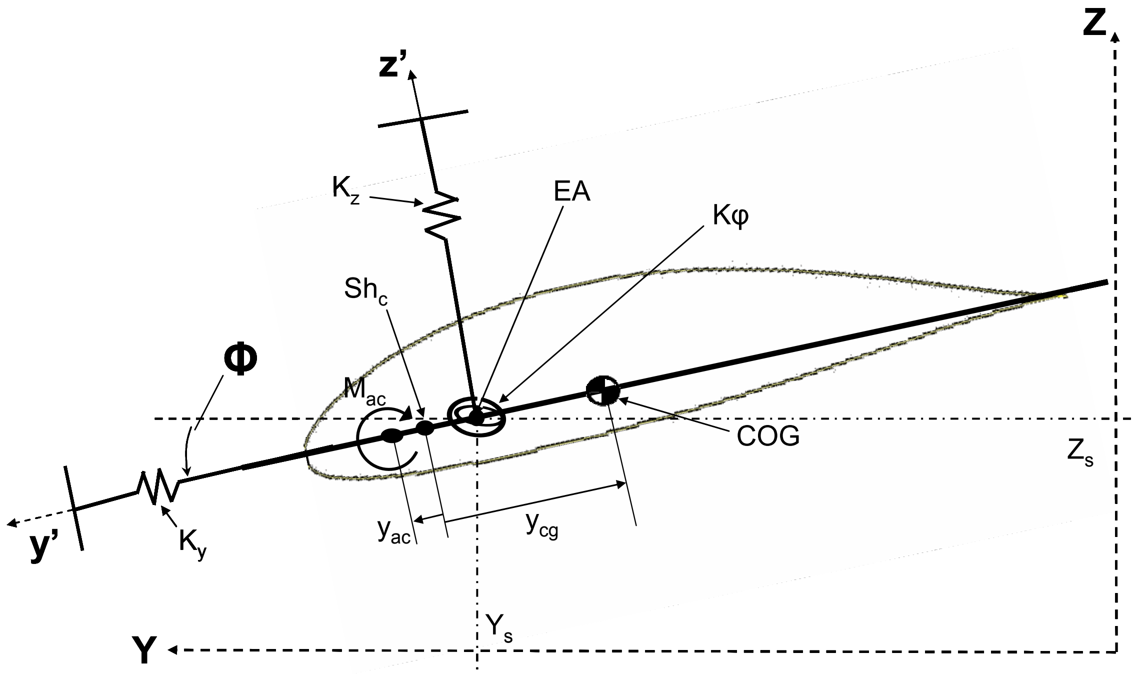

Figure II.1 Cross Section of Aerofoil Showing Structural Model Properties and Coordinate Systems

A.II.III Blade Properties for Selected Nodes

Node (m)	Mass Distribution (kg/m)	Chord (m)	Twist (Deg)	Flap Stiffness (EI) (Nm^2)	Edgewise Stiffness (EI) (Nm^2)	Torsion Stiffness (GJ) (Nm^2)	Polar Moment of Inertia (I) (kg.m^2/m)	COG (y_{cg})[1] (m)	Shc[2] (m)	EA[3] (m)
0.00	715.00	3.54	13.31	1.81E+10	1.81E+10	5.56E+09	1449.05	-0.20	-0.70	-0.20
3.20	780.00	3.54	13.31	1.81E+10	1.81E+10	4.99E+09	1497.08	-0.19	-0.70	-0.21
6.20	474.00	3.67	13.31	1.53E+10	1.98E+10	2.32E+09	827.62	-0.21	-0.66	-0.24
9.20	422.00	4.38	13.31	6.31E+09	9.15E+09	1.16E+09	685.32	-0.37	-0.41	-0.31
12.20	439.00	4.59	13.18	4.94E+09	7.01E+09	6.72E+08	657.62	-0.67	-0.13	-0.54
15.20	372.00	4.62	11.56	3.39E+09	7.08E+09	3.36E+08	524.52	-0.62	-0.22	-0.38
18.20	365.00	4.59	10.79	2.39E+09	4.95E+09	2.92E+08	485.33	-0.61	-0.21	-0.39
22.20	348.00	4.39	9.67	2.05E+09	4.50E+09	2.29E+08	401.33	-0.57	-0.18	-0.39
26.20	330.00	4.05	7.93	1.59E+09	4.00E+09	1.44E+08	338.57	-0.51	-0.15	-0.38
30.20	277.00	3.79	6.71	1.10E+09	3.45E+09	8.12E+07	212.29	-0.44	-0.16	-0.33
34.20	267.00	3.69	6.12	6.81E+08	2.73E+09	6.91E+07	193.97	-0.43	-0.17	-0.32
38.20	232.00	3.45	4.97	4.09E+08	2.33E+09	4.59E+07	144.50	-0.41	-0.16	-0.30
42.20	189.00	3.19	3.83	2.39E+08	1.58E+09	2.74E+07	104.64	-0.36	-0.22	-0.25
46.20	163.00	2.97	2.89	1.26E+08	1.18E+09	1.85E+07	90.93	-0.42	-0.21	-0.29
50.20	113.00	2.60	1.73	9.09E+07	7.98E+08	9.07E+06	48.03	-0.33	-0.20	-0.22
54.20	104.00	2.49	1.34	6.10E+07	5.18E+08	8.06E+06	41.78	-0.33	-0.20	-0.22

[1] Denotes the centre of gravity offset from the elastic shear centre (Shc) measured along the chord length

[2] Denotes the shear centre offset relative to the aerodynamic centre (quarter chord point) measured along the chord length

[3] Denotes the position of the elastic axis offset relative to the shear centre (Shc)

57.20	76.80	2.24	0.57	3.94E+07	3.95E+08	5.75E+06	21.39	0.23	0.20	
58.70	69.80	2.16	0.40	2.65E+07	2.81E+08	5.33E+06	18.13	0.23	0.19	
60.20	58.90	2.07	0.32	1.60E+07	1.38E+08	3.66E+06	10.42	0.15	0.18	
61.20	51.70	1.96	0.22	7.55E+06	8.51E+07	2.64E+06	7.26	0.13	0.15	
61.50	48.30	1.69	0.14	2.45E+05	5.01E+06	2.17E+06	5.91	0.12	0.13	

A.III Determination of Blade Eigenmodes

The following procedure gives the algorithm used to compute the blade eigenmode shape and corresponding slopes and curvatures, which are used to estimate the amount of work done in blade bending for the estimates of blade deflection at each node. The following algorithm is as given by [ref 10].

A.III.I 1st, 2nd Flapwise & 1st Edgewise Eigenmodes

The procedure makes use of arbitrary static forces (P_Y & P_Z) applied in the wind coordinate system to determine shear forces and bending moments in each respective blade station. These moments are converted to the blade principle axis to give the eigenmodes in this coordinate system, for as is shown in A.IV, a transformation from the principle axis back to the blade axis is made which accounts for the built-in twist and elastic twist of the blade, while acting in the presence of flapwise and edgewise deflections. The bending moments can be related to curvature of the blade, which is numerically integrated to arrive at the eigenmode shape according to the blade properties. This can be used in an iterative procedure to determine the first few eigenmodes of the blade. The following outlines the procedure.

For each blade node station starting from the tip, determine the shear forces in the Y, and Z direction, with the shear forces being equal to zero at the tip:

III.1

$$T_Y^{i-1} = T_Y^{i} + \frac{1}{2}(P_Y^{i-1} + P_Y^{i})(x^i - x^{i-1})$$

$$T_Z^{i-1} = T_Z^{i} + \frac{1}{2}(P_Z^{i-1} + P_Z^{i})(x^i - x^{i-1})$$

Where x is the distance on the node in question.

The moments at each node can then be found from (M_Y meaning the moment in flapwise-direction and notation likewise for other formulas below):

III.2

$$M_Y^{i-1} = M_Y^{i} + T_Y^{i}(x^i - x^{i-1}) + (\frac{1}{6}p_Y^{i-1} + \frac{1}{3}p_Y^{i})^2$$

$$M_Z^{i-1} = M_Z^{i} + T_Z^{i}(x^i - x^{i-1}) + (\frac{1}{6}p_Z^{i-1} + \frac{1}{3}p_Z^{i})^2$$

These moments are transformed to the principle axis using the built in twist of the blade:

III.3

$$M_{y'} = M_Y \cos\beta - M_Z \sin\beta$$

$$M_{z'} = M_Y \sin\beta + M_Z \cos\beta$$

With the moments identified in the principle axis, the curvature for each direction is obtained from:

III.4

$$\kappa_{y'} = \frac{M_{y'}}{EI_{edgewise}}$$

$$\kappa_{z'} = \frac{M_{z'}}{EI_{flapwise}}$$

The curvature can now be numerically integrated to give the slope (gradient) of the eigenmode and finally the deflection modeshape, the values of which are given in A.III.II.

The slope is calculated from, with slope at the blade root equal to zero:

III.5

$$\theta_{y'}^{i+1} = \theta_{y'}^{i}(\kappa_{y'}^{i+1} + \kappa_{y'}^{i})(x^{i+1} - x^{i})$$

$$\theta_{z'}^{i+1} = \theta_{z'}^{i}(\kappa_{z'}^{i+1} + \kappa_{z'}^{i})(x^{i+1} - x^{i})$$

The deflection is found according to the slope and curvature by:

III.6

$$u_{y'}^{i+1} = u_{y'}^{i} + \theta_{z'}^{i}(x^{i+1} - x^{i}) + (\frac{1}{6}\kappa_{z'}^{i+1} + \frac{1}{3}\kappa_{z'}^{i})^{2}$$

$$u_{z'}^{i+1} = u_{z'}^{i} + \theta_{y'}^{i}(x^{i+1} - x^{i}) + (\frac{1}{6}\kappa_{y'}^{i+1} + \frac{1}{3}\kappa_{y'}^{i})^{2}$$

With the arbitrary loading applied and given mass of the blade at each node, the natural frequency is estimated from:

III.7

$$\omega = \sqrt{\frac{p_{z'}^{tip}}{u_{z'}^{tip} m^{tip}}}$$

This natural frequency can then be used to calculate a new loading value and all the previous equations are reapplied iteratively to find the frequency until convergence is reached.

The new loading is found from:

III.8

$$p_{y'}^{i} = \omega^{2} m^{i} u_{y'}^{i}$$

$$p_{z'}^{i} = \omega^{2} m^{i} u_{z'}^{i}$$

Using this method, the solution converges to the 1st blade flapwise eigenmode. The second flapwise and 1st edgewise modes are determined through subtracting the constants (given in section 3.1.4.1 of the report) at each iteration to converge on the desired mode. The values obtained from this procedure for the Upwind turbine blade are given overleaf.

The Constant to subtract for finding the 2nd flapwise is as follows from [ref 10]:

III.9

$$k_{2f} = \frac{\int_0^R u_{z'}^{1e} m_i u_{z'} dx' + \int_0^R u_{y'}^{1e} m_i u_{y'} dx'}{\int_0^R u_{z'}^{1e} m_i u_{z'}^{1e} dx' + \int_0^R u_{y'}^{1e} m_i u_{y'}^{1e} dx'}$$

Method for determination of 1st Torison Eigenmode:

The method here follows similar logic to the above iterative process but only requires the 1st torsion mode for this study. Section 3.1.4.1 of the main report gives the procedure and is not repeated here.

A.III.II Blade Eigenmode Data (Deflection, Slope & Curvature)

	Normalised Eigenmode Deflections				Eigenmode Slopes				Eigenmode Curvatures			
Node (m)	1st Flapwise	2nd Flapwise	1st Edgedwise	1st Torsion	1st Flapwise	2nd Flapwise	1st Edgedwise	1st Torsion	1st Flapwise	2nd Flapwise	1st Edgedwise (x 10^{-3})	1st Torsion
0.00	0.0000	0.0000	0.0000	0.0000	0.0000	0.0000	0.0000	0.0000	0.0000	0.0000	0.0000	0.0000
3.20	0.0002	-0.0006	0.0006	0.0000	0.0002	-0.0007	0.0005	0.0000	0.0001	-0.0003	0.2833	0.0000
6.20	0.0009	-0.0026	0.0026	0.0001	0.0005	-0.0020	0.0013	0.0000	0.0001	-0.0004	0.2388	0.0000
9.20	0.0027	-0.0075	0.0078	0.0002	0.0010	-0.0041	0.0025	0.0001	0.0002	-0.0008	0.4756	0.0000
12.20	0.0062	-0.0159	0.0168	0.0005	0.0018	-0.0071	0.0042	0.0001	0.0003	-0.0009	0.5697	0.0000
15.20	0.0123	-0.0290	0.0311	0.0013	0.0028	-0.0107	0.0059	0.0003	0.0004	-0.0011	0.5198	0.0001
18.20	0.0216	-0.0465	0.0511	0.0028	0.0041	-0.0151	0.0078	0.0005	0.0005	-0.0014	0.6726	0.0001
22.20	0.0399	-0.0838	0.0864	0.0069	0.0062	-0.0212	0.0107	0.0009	0.0005	-0.0013	0.6622	0.0001
26.20	0.0665	-0.1242	0.1334	0.0144	0.0084	-0.0268	0.0134	0.0013	0.0006	-0.0012	0.6287	0.0001
30.20	0.1023	-0.1678	0.1915	0.0261	0.0109	-0.0318	0.0160	0.0021	0.0007	-0.0011	0.5965	0.0003
34.20	0.1488	-0.2113	0.2603	0.0442	0.0141	-0.0355	0.0185	0.0032	0.0009	-0.0010	0.5941	0.0003
38.20	0.2089	-0.2488	0.3392	0.0730	0.0182	-0.0368	0.0209	0.0047	0.0012	-0.0005	0.5261	0.0004
42.20	0.2866	-0.2681	0.4277	0.1162	0.0234	-0.0332	0.0231	0.0071	0.0015	0.0004	0.5549	0.0007
46.20	0.3866	-0.2474	0.5253	0.1794	0.0301	-0.0208	0.0253	0.0107	0.0019	0.0021	0.4932	0.0011
50.20	0.5129	-0.1572	0.6316	0.2750	0.0371	-0.0002	0.0273	0.0174	0.0016	0.0033	0.4372	0.0022

54.20	0.6660	0.0317	0.7455	0.4210	0.0428	0.0239	0.0289	0.0245	0.0012	0.0039	0.3396	0.0025
57.20	0.7960	0.3299	0.8352	0.5950	0.0457	0.0401	0.0297	0.0289	0.0007	0.0032	0.1607	0.0035
58.70	0.8648	0.5992	0.8810	0.7131	0.0465	0.0453	0.0298	0.0344	0.0003	0.0017	0.0634	0.0038
60.20	0.9346	0.7515	0.9271	0.8532	0.0468	0.0480	0.0299	0.0390	0.0002	0.0010	0.0449	0.0055
61.20	0.9815	0.9025	0.9579	0.9631	0.0470	0.0489	0.0299	0.0410	0.0002	0.0003	0.0095	0.0076
61.50	1.0000	1.0000	1.0000	1.0000	0.0470	0.0491	0.0299	0.0410	0.0000	0.0004	0.0052	0.0076

A.IV Bending - Torsion Transformation Equations

The following set of equations has been taken from [ref 1].

The equations are used to account for the coupling of the flapwise and edgewise deflections acting in the presence of elastic torsion and built in twist of the blade. The twisting of the blade tilts the principle axis out of the rotor plane, thereby causing this coupling to occur (refer to diagram in A.II). The deformations are conveniently described in the principle axis of the blade, which gives a spatially changing elastic axis (relative to the rotating blade coordinate system) according to the flapwise and edgewise deflections and where the built in twist and elastic twist can be accounted for.

Because this model uses an uncoupled modal approach, a way to include this coupling is through a trigonometric transformation on the curvatures of the elastic axis (y', z') to the rotating blade axis (Y, Z), i.e.:

IV.1

$$\frac{d^2Z}{dX^2} = \frac{d^2z'}{dx'^2} C\operatorname{os}\Phi - \frac{d^2y'}{dx'^2} S\operatorname{in}\Phi$$

$$\frac{d^2Y}{dX^2} = \frac{d^2z'}{dx'^2} Sin\Phi - \frac{d^2y'}{dx'^2} Cos\Phi$$

Where Φ is the total twist of the blade out of the rotor plane which is changing in time?

Bielawa describes a series of partial integrations which can be applied to approximate this transformation to the blade system with an uncoupled modal approach. The equations are described below.

The deflection in the rotating blade coordinate system (X, Y, Z) is approximated for flapwise (Z_f) and edgewise (Y_e) directions using the uncoupled modal deflections by:

IV.2

$$Y_e = (y_e' + \Delta y' - \Delta Y')\cos\Phi - (z_f' - \Delta z' - \Delta Z')\sin\Phi$$
$$Z_f = (y_e' + \Delta y' - \Delta Y')\sin\Phi + (z_f' - \Delta z' - \Delta Z')\cos\Phi$$

Where,

y_e' is the uncoupled edgewise modal deflection as detailed in the main section of the report

z_f' is the uncoupled flapwise modal deflection

Other variables represented by the following integral functions:

IV.3

$$\Delta y' = \int_0^{x'} \frac{d\Phi}{dx'}.z_f.dx' + \int_0^{x_1'}\int_0^{x_2'} \frac{d\Phi}{dx'}.\frac{dz_f}{dx'}.dx_2'dx_1' = \Delta y'^{(1)} + \Delta y'^{(2)}$$

$$\Delta z' = \int_0^{x'} \frac{d\Phi}{dx'}.y_e.dx' + \int_0^{x_1'}\int_0^{x_2'} \frac{d\Phi}{dx'}.\frac{dy_e}{dx'}.dx_2'dx_1' = \Delta z'^{(1)} + \Delta z'^{(2)}$$

IV.4

$$\Delta Y' = \int_0^{x'} \frac{d\Phi}{dx'}.\Delta z' dx' + \int_0^{x_1'} \int_0^{x_2'} \frac{d\Phi}{dx'}.\Delta z'^{(2)}\, dx_2 dx_1$$

$$\Delta Z' = \int_0^{x'} \frac{d\Phi}{dx'}.\Delta y' dx' + \int_0^{x_1'} \int_0^{x_2'} \frac{d\Phi}{dx'}.\Delta y'^{(2)}\, dx_2 dx_1$$

The resulting deflections have therefore been corrected according to this coupling.

A.V Runge Kutta – Nystrom Integration Scheme

The equations of motion for the blade dynamics can be numerically evaluated using the Runge Kutta scheme. The idea is that knowing the accelerations, velocities and positions at time t1, this scheme can be used to estimate the velocities and positions at time t2. The acceleration can then be updated and a new time step performed.

The Runge Kutta integration scheme uses the following algorithm:

$$\overline{A} = \frac{\Delta t}{2}\ddot{\overline{x}}^{n}$$

$$\overline{b} = \frac{\Delta t}{2}(\dot{\overline{x}} + \frac{1}{2}\overline{A})$$

$$\overline{B} = \frac{\Delta t}{2}\overline{g}(t^{n+\frac{1}{2}}, \overline{x}^{n} + \overline{b}, \dot{\overline{x}}^{n} + \overline{A})$$

$$\overline{C} = \frac{\Delta t}{2}\overline{g}(t^{n+\frac{1}{2}}, \overline{x}^{n} + \overline{b}, \dot{\overline{x}}^{n} + \overline{B})$$

$$\overline{d} = \Delta t(\dot{\overline{x}}^{n} + \overline{C})$$

$$\overline{D} = \frac{\Delta t}{2}\overline{g}(t^{n+1}, \overline{x}^{n} + \overline{d}, \dot{\overline{x}}^{n} + 2\overline{C})$$

Where the overhead bar denotes a matrix in the case of multiple degrees of freedom.

The update for the next time step is then performed:

$$t^{n+1} = t^{n} + \Delta t$$

$$\overline{x}^{n+1} = \overline{x}^{n} + \Delta t(\dot{\overline{x}}^{n} + \frac{1}{3}(\overline{A} + \overline{B} + \overline{C}))$$

$$\dot{\overline{x}}^{n+1} = \dot{\overline{x}}^{n} + \frac{1}{3}(\overline{A} + 2\overline{B} + 2\overline{C} + \overline{D}))$$

$$\ddot{\overline{x}}^{n+1} = g(t^{n+1}, \overline{x}^{n+1}, \dot{\overline{x}}^{n+1})$$

A.VI 10MW Up-Scaling Methodology

In this section, the methodology and scaling principles used to estimate the design of a 10MW wind turbine is given.

A new 10MW wind turbines structural blade properties important for the current analysis were determined from scaling the following properties from the 5MW UpWind turbine:

- Blade Mass
- Flapwise, Torsion & Edgewise Stiffness for eigenfrequency determination
- Polar moment of inertia
- Inertial Torsional Moment
- Chord length
- Centre of gravity and aerodynamic centre offsets

A blade length of 86m (diameter 172m) was chosen to be representative of a 10MW wind turbine. The chord length was then scaled in proportion to the increase in radius from the UpWind turbine.

It is also assumed the blades become more slender as a result of keeping mass low, and this slenderness is taken to be the cause of keeping the blade thickness constant while chord length is increased.

Stiffness:

The stiffness of the blade is estimated according to the moment of inertia of the blade.

VI.1

$$k = E.I$$

$$I_f = \frac{ct^3}{12}$$

$$I_e = \frac{tc^3}{12}$$

For constant blade thickness, the new stiffness can be estimated from the original blade:

VI.2

$$k_f = \frac{c_n}{c_o} k_{f,o}$$

$$k_e = (\frac{c_n}{c_o})^3 k_{e,o}$$

where,

$k_{f,o}$ and $k_{e,o}$ are the original stiffness values; and

c_n and c_o are the new and old chord lengths respectively

The torsion stiffness is found from:

VI.3

$$k_t = G.J$$

With G being the material mechanical property of the material and J the polar moment of inertia. For constant blade thickness, the torsion stiffness was considered to scale according to the chord by the following:

VI.4

$$k_t = \left(\frac{c_n^{\ 3} + c_n}{c_o^{\ 3} + c_o}\right)k_{t,o}$$

This relation is derived from the polar moment of inertia being approximately equivalent to:

VI.5

$$J = I_f + I_e \, .$$

Blade Mass:

Similarly to stiffness, for an up-scaled blade with thickness remaining constant, the mass per unit length (m) is assumed to increase linearly with blade radius according to:

VI.6

$$m = \frac{c_n}{c_o} m_o$$

Where m_o is the original mass.

Chordwise Offsets:

The centre of gravity and aerodynamic centre were assumed to scale linearly with the original chord length.

Inertial Torsional Moment (pitching inertia):

This is the moment produced from the mass acting a distance from a prescribed axis. It is found from the mass radii of gyration of a blade section about the chordwise axis and an axis perpendicular to this through the elastic axis [ref 1]. The polar moment of inertia is defined from these as [ref 1]:

VI.7

$$J = \sqrt{y_{m1}^{\ 2} + y_{m2}^{\ 2}}$$

Where y_{m1} is the mass radii of gyration about a chordwise axis, and y_{m2} is perpendicular to this about the elastic axis (in thickness direction).

The mass radii of gyration was assumed to increase linearly with the chord length in chordwise direction only, since for the direction perpendicular to this (thickness direction), the geometry has been assumed constant (constant thickness). The torsional moment coefficient was found then determined according to the new blade mass and new polar moment of inertia as above:

$$I = mJ$$

For which the torsional moment is defined as:

$$M_T = I\ddot{\varphi}_e$$

Where $\ddot{\varphi}$ is the angular acceleration of a blade in torsion.

Rotor Speed:

The rotor speed was assumed to vary according to the increase in radius of the blade, i.e. the rotor speeds are less for increased radius.